

Turbulence and turbulent heat transfer at supercritical pressure

Peeters, Jurriaan

DOI

[10.4233/uuid:54f6098c-4c99-4129-8d8c-353a9411c0ae](https://doi.org/10.4233/uuid:54f6098c-4c99-4129-8d8c-353a9411c0ae)

Publication date

2016

Document Version

Final published version

Citation (APA)

Peeters, J. (2016). *Turbulence and turbulent heat transfer at supercritical pressure*. [Dissertation (TU Delft), Delft University of Technology]. <https://doi.org/10.4233/uuid:54f6098c-4c99-4129-8d8c-353a9411c0ae>

Important note

To cite this publication, please use the final published version (if applicable).
Please check the document version above.

Copyright

Other than for strictly personal use, it is not permitted to download, forward or distribute the text or part of it, without the consent of the author(s) and/or copyright holder(s), unless the work is under an open content license such as Creative Commons.

Takedown policy

Please contact us and provide details if you believe this document breaches copyrights.
We will remove access to the work immediately and investigate your claim.

TURBULENCE AND TURBULENT HEAT TRANSFER AT SUPERCRITICAL PRESSURE

Proefschrift

ter verkrijging van de graad van doctor
aan de Technische Universiteit Delft,
op gezag van de Rector Magnificus prof. ir. K.C.A.M. Luyben,
voorzitter van het College voor Promoties,
in het openbaar te verdedigen op woensdag 30 november 2016 om 12:30 uur

door

Jurriaan Willem Reinier PEETERS

Natuurkundig ingenieur,
Technische Universiteit Delft,
geboren te Nieuwegein, Nederland.

Dit proefschrift is goedgekeurd door de

promotoren: prof. dr. ir. B. J. Boersma & prof. dr. ir. T. H. J. J. van der Hagen
copromotor: dr. R. Pecnik

Samenstelling promotiecommissie:

| | |
|--|-------------------------------|
| Rector Magnificus, | voorzitter |
| Prof. dr. ir. B. J. Boersma, | Technische Universiteit Delft |
| Prof. dr. ir. T. H. J. J. van der Hagen, | Technische Universiteit Delft |
| Dr. R. Pecnik, | Technische Universiteit Delft |

Onafhankelijke leden:

| | |
|--|--|
| Prof. dr. ir. B. J. Geurts, | Universiteit Twente |
| Prof. S. He, BSc, MSc, PhD, CEng, FIMechE | The University of Sheffield |
| Prof. dr. ir. W. van de Water, | Technische Universiteit Delft & Technische Universiteit Eindhoven |
| Prof. dr. S. Hickel, | Technische Universiteit Delft |

Overige leden:

| | |
|------------------|-------------------------------|
| Dr. ir. M. Rohde | Technische Universiteit Delft |
|------------------|-------------------------------|



“Dit onderzoek is medegefinancierd door Technologiestichting STW, die onderdeel is van de Nederlandse Organisatie voor Wetenschappelijk Onderzoek (NWO) en deels gefinancierd wordt door het Ministerie van Economische Zaken.”

Keywords: Turbulence, Heat Transfer, Supercritical Pressure, Direct Numerical Simulations

Printed by: Gildeprint – www.gildeprint.nl

Front & Back: Cross-sectional visualisation of the enthalpy in a simultaneously heated and cooled fully developed turbulent flow at supercritical pressure in an annular geometry.

Copyright © 2016 by J. W. R. Peeters

ISBN 978-94-6233-482-3

An electronic version of this dissertation is available at

<http://repository.tudelft.nl/>

Had I the heavens' embroidered cloths,
Enwrought with golden and silver light,
The blue and the dim and the dark cloths
Of night and light and the half light,
I would spread the cloths under your feet:
But I, being poor, have only my dreams;
I have spread my dreams under your feet;
Tread softly because you tread on my dreams.

W. B. Yeats, 1865 - 1939

*voor mijn vader, moeder †
en mijn broers*

ABSTRACT

The world population is rapidly growing. As a result, the world energy demand is increasing as well. Currently, many power plants produce greenhouse gases, which contribute to an increase in global temperature. To meet the increase in energy demand, more efficient and greenhouse gas-free methods are necessary.

Applying enhanced thermodynamic cycles to, for example, concentrated solar power plants or nuclear power plants, will lead to energy efficient and low greenhouse gas emission technologies. The thermal efficiency of a thermodynamic cycle can be enhanced, by raising the pressure of either a part of the cycle or the whole cycle to supercritical pressure. At supercritical pressure, a fluid does not undergo a phase change during a heating process. It transitions from a fluid with liquid-like properties to a fluid with gas-like properties. However, heated or cooled fluids at supercritical pressure show large variations in thermophysical properties. The largest variations are found close the pseudo-critical temperature, the temperature for which the specific heat capacity has a maximum. These variations in thermophysical properties may lead to enhanced or deteriorated heat transfer when compared to similar conditions at sub-critical pressure. Currently, the mechanisms that lead to enhanced or deteriorated heat transfer are not fully understood, yet. This thesis aims to help elucidate these mechanisms.

To this end, a numerical code was developed with the aim to perform direct numerical simulations of turbulent heat transfer to a fluid at supercritical pressure. Direct numerical simulations were performed of a turbulent flow at super-critical pressure (CO_2 at 8 MPa) in an annulus with a hot inner wall and a cold outer wall. The annular geometry was chosen, as it is a common geometry found in heat transfer equipment. The pseudo-critical temperature lies close to the inner wall, which results in strong thermophysical property variations in that region.

First, the attenuation of turbulence was studied, as turbulence plays a major role in heat transfer. The turbulence attenuation was studied in two ways; by analysing mean statistics and by studying coherent structures such as near wall streaks and streamwise vorticity, which are part of the near wall cycle of turbulence. The turbulent shear stress

and the turbulent intensities significantly decrease near the hot inner wall, but increase near the cold outer wall, which can partially be attributed to the mean dynamic viscosity and density stratification. This leads to a decreased production of turbulent kinetic energy near the inner wall and vice versa near the outer wall.

By analysing an evolution equation for the coherent streak flank strength, which was derived by taking the curl of the momentum conservation equation in conservative form, the generation of streaks was investigated. It was found that thermophysical property fluctuations significantly affect streak evolution. Near the hot wall, thermal expansion and buoyancy hinder the formation of streaks, while the viscosity gradient that exists across the streaks interacts with mean shear to act either as a source or a sink in the evolution equation for the coherent streak flank strength.

The formation of streamwise vortices was also investigated using an evolution equation. Streamwise vortices are hindered by the torque that is the result of the kinetic-energy-and-density-gradients. Near the cold wall, the results are reversed, i.e. the coherent streak flank strength and the stream-wise vortices are enhanced due to the variable density and dynamic viscosity. The results show that not only the mean stratification, but also the large instantaneous thermophysical property variations that occur in heated or cooled fluids at supercritical pressure have a significant effect on turbulent structures that are responsible for the self-regeneration process in near wall turbulence. Thus, instantaneous density fluctuations are partially responsible for decreased (or increased) turbulent motions in heated (or cooled) fluids at supercritical pressure.

Subsequently, turbulent heat transfer both near the hot inner wall and near the cooled outer wall was studied. Mean high values of the specific heat capacity cause the mean temperature profile to flatten, while mean low values of the specific heat capacity have the opposite effect. Also, high mean values of the specific heat capacity dampen temperature fluctuations, while low values enhance temperature fluctuations. When comparing the probability density functions of the enthalpy fluctuations to that of the temperature variations, it was found that the turbulent variation of the specific heat capacity may enhance or dampen extreme temperature fluctuations.

The radial turbulent heat flux is affected by both the attenuation of the wall normal motions, but also by the enhancement of the enthalpy fluctuations near the heated surface. The enhancement of the enthalpy fluctuations can be attributed to a large average molecular Prandtl number. Molecular conduction is affected as the mean thermal diffusivity changes. A new average heat flux arises due to thermal diffusion fluctuations and enthalpy gradient fluctuations. This heat flux may be significant locally, but has a negligible effect on the Nusselt number.

Combining a relation between the Nusselt number and the radial heat fluxes together

with a quadrant analysis of the turbulent heat flux shows that different heat flux quadrants are affected differently by the thermophysical properties. These heat flux quadrants represent different turbulent heat flux events, i.e. hot fluid moving away from the wall (hot ejections), hot fluid moving toward the wall, cold fluid moving toward the wall (cold sweeps) and cold fluid moving away from the wall. Conditional averaging shows that different heat flux quadrants have significant different densities and molecular Prandtl numbers which means that certain flux quadrants are more effective at transporting heat than others. The density is an important factor in heat transfer as it determines how much heat a fluid particle can contain per volume. The Prandtl number is also an important factor, as the so-called time-scale ratio scales with the Prandtl number. This ratio can be thought of as a ratio of the heat decay time to the mechanical decay time. Higher time-scale ratios mean that hot fluid moving away from the hot wall decays less fast, or that it penetrates easier into the bulk of the flow. The analysis shows that not only the mean density and molecular Prandtl number variation, but also their fluctuations are important in understanding heat transfer to turbulent supercritical fluids.

The observation that hot ejections and cold sweeps have different Prandtl numbers was used to derive a new analogy between the Nusselt number and the friction factor. This new analogy was tested against various experiments reported in literature. The comparisons between results from the new analogy and experimental results suggest that such an analogy may be valid at low heat flux to mass flux ratios. This result may help to develop better heat transfer models for heat transfer to fluids at supercritical pressure in the future.

SAMENVATTING

De wereldbevolking is snel aan het groeien. Dientengevolge neemt de wereldwijde vraag naar energie ook toe. Veel krachtcentrales produceren heden ten dage broeikasgassen die bijdragen aan de opwarming van de aarde. Om te kunnen voldoen aan de wereldwijde vraag naar energie zijn efficiëntere methoden, die geen broeikasgassen uitstoten, nodig.

Het toepassen van verbeterde thermodynamische cycli op bijvoorbeeld geconcentreerde zonnekrachtcentrales of nucleaire krachtcentrales, zal leiden tot energie-efficiënte technologieën die weinig broeikasgassen uitstoten. De thermische efficiëntie van een thermodynamische cyclus kan verbeterd worden door de druk van óf een deel van de cyclus óf de gehele cyclus te verhogen naar superkritische druk. Bij een fluïdum dat onder superkritische druk staat vind gedurende een verwarmingsproces geen faseovergang plaats. Het fluïdum verandert van een fluïdum met vloeistof-achtige eigenschappen in een fluïdum met gas-achtige eigenschappen. Echter, verwarmde of gekoelde fluïda bij superkritische druk vertonen sterke variaties in de thermofysische eigenschappen. De grootste variaties zijn dicht bij de pseudo-kritische temperatuur te vinden; de temperatuur waarbij de specifieke warmtecapaciteit een maximum vertoont. Deze variaties in de thermofysische eigenschappen kunnen leiden tot verbeterde of verslechterde warmteoverdracht wanneer deze vergeleken wordt met soortgelijke condities bij sub-kritische druk. De mechanismen die tot verbeterde of verslechterde warmteoverdracht leiden zijn nog niet volledig begrepen. Dit proefschrift beoogt dergelijke mechanismen te verhelderen.

Daartoe is een numerieke code ontwikkeld met het doel om zogeheten directe numerieke simulaties van turbulente warmteoverdracht naar een stroming, die onder superkritische druk staat, uit te voeren. Dergelijke simulaties zijn uitgevoerd voor een turbulente stroming bij superkritische druk (CO_2 bij 8 MPa) in een annulus met een hete binnenwand en een koude buitenwand. Deze geometrie is uitgekozen om zijn veelvuldig voorkomen in warmteoverdrachtsmachinerie. De pseudo-kritische temperatuur ligt nabij de binnenwand, hetgeen sterke thermofysische-eigenschaps-variaties in dat gebied tot gevolg heeft.

De verzwakking van de turbulentie is als eerste onderzocht, omdat turbulentie een

grote rol speelt in warmteoverdracht. De turbulentieverzwakking is op twee manieren bestudeerd; door gemiddelde statistieken, als ook coherente structuren zoals ‘streaks’ en stroomsgewijze vorticeiteit, welke een onderdeel zijn van een structuur cyclus nabij de wand te onderzoeken. De turbulente schuifspanning en de turbulente intensiteiten nemen significant af nabij de hete binnenwand, maar nemen juist toe in de buurt van de koude buitenwand, hetgeen, op zijn minst ten dele, toegeschreven kan worden aan de dynamische- viscositeits- en- dichtheids- stratificatie. Dit leidt tot een afgenomen productie van turbulente kinetische energie nabij de binnenwand en juist het tegenovergestelde in de buurt van de buitenwand.

Door een evolutievergelijking voor de coherente ‘streak’ flanksterkte, die afgeleid kan worden door de rotatie-operator op de impulsbehoudswet in conservatieve vorm toe te passen, te analyseren, kon de totstandkoming van de ‘streaks’ onderzocht worden. Uit dit onderzoek kwam naar voren dat de fluctuaties van de thermofysische stoffeigenschappen de ‘streak’ evolutie sterk beïnvloeden. Nabij de hete binnenwand hinderen thermische expansie en de opwaartse kracht de totstandkoming van de ‘streaks’. De viscositeitsgradiënt die tussen ‘streaks’ bestaat heeft een interactie met de gemiddelde snelheidsgradiënt wat óf als een bron óf als een vernietigingsterm kan optreden in de evolutievergelijking van de coherente ‘streak’ flanksterkte.

De totstandkoming van stromingsgewijze kolken is ook bestudeerd met behulp van een evolutievergelijking. Stroomsgewijze kolken worden verhinderd door het koppel van de kinetische-energie-gradiënten en de dichtheidsgradiënten. Nabij de koude buitenwand zijn de resultaten omgedraaid; de coherente ‘streak’ flanksterkte en de stromingsgewijze kolken worden versterkt door de variabele dichtheid en de dynamische viscositeit. Deze resultaten laten zien dat niet alleen de gemiddelde stratificatie, maar ook grote instantane thermofysische stoffeigenschapsvariaties, die in verhitte of gekoelde turbulente fluïda bij superkritische druk kunnen voorkomen, een significant effect hebben op de turbulente structuren die verantwoordelijk zijn voor het zelf-regeneratie-proces van turbulentie nabij de wand. Instantane dichtheidsfluctuaties zijn dus verantwoordelijk voor verzwakte of juist versterkte turbulente bewegingen in verhitte of gekoelde fluïda bij superkritische druk.

Vervolgens is ook de turbulente warmteoverdracht zowel nabij de hete binnenwand als ook de koude buitenwand bestudeerd. Gemiddeld hoge waarden van de specifieke warmtecapaciteit maken het gemiddelde temperatuurprofiel platter, terwijl gemiddeld lage waarden van de specifieke warmtecapaciteit het tegenovergestelde effect hebben. Hoge gemiddelde waarden van de specifieke warmtecapaciteit verzwakken de temperatuur fluctuaties, terwijl lage specifieke warmtecapaciteitswaarden de temperatuurfluctuaties juist versterken. Door kansdichtheidsfuncties van de enthalpiefluctuaties en de tem-

peratuurfluctuaties te vergelijken is duidelijk geworden dat de turbulente variatie van de specifieke warmtecapaciteit extreme temperatuurfluctuaties kan versterken of juist verzwakken.

Zowel de verzwakking van de wandnormale beweging als de toename van de enthalpiefluctuaties beïnvloeden de radiële turbulente warmteflux nabij een verhitte wand. De versterking van de enthalpiefluctuaties kan toegeschreven worden aan de hoge gemiddelde waarden van het moleculaire Prandtl-getal. Moleculaire geleiding wordt beïnvloed door de gemiddelde thermische-diffusiviteitsverandering. Een nieuwe gemiddelde warmteflux komt tot stand door de thermische-diffusie-fluctuaties en de enthalpiegradiënt fluctuaties. Deze warmteflux kan lokaal significant zijn, maar heeft een verwaarloosbaar effect op het Nusselt getal.

Door een relatie tussen het Nusselt-getal en de radiële warmtefluxen te combineren met kwadrantanalyse van de turbulente warmteflux wordt inzichtelijk hoe verschillende kwadranten op verschillende manieren beïnvloed worden door de thermofysische eigenschappen. De warmteflux kwadranten stellen ieder een bepaald aspect van de warmteflux voor, zoals warme vloeistof die van de wand weggaat, warme vloeistof die naar de wand toegaat, koude vloeistof die naar de wand toegaat en koude vloeistof die van de wand weggaat. Conditionele gemiddelden laten zien dat verschillende warmteflux kwadranten duidelijk verschillende dichtheden en moleculaire Prandtl-getal-waarden hebben, wat zoveel betekent dat sommige kwadranten effectiever of juist minder effectief zijn in warmteoverdracht. De dichtheid beïnvloed de warmteflux direct. Het moleculaire Prandtl-getal is ook belangrijk, omdat de zoeten tijdschaalverhouding hiermee schaal. Deze tijdsschaalverhouding kan gezien worden als de verhouding van de karakteristieke warmteafname-tijd tot de mechanische afname tijd. Hogere tijdschaal verhoudingen betekenen dat de warmte die van een hete wand weggaat minder snel afneemt, of makkelijker tot in het midden van de stroming door kan dringen. De analyse laat zien dat niet alleen de gemiddelde variatie van de dichtheid en het moleculaire Prandtl-getal, maar juist ook de fluctuaties daarvan van belang zijn om warmteoverdracht naar turbulente fluïda te begrijpen.

De observatie dat warme vloeistof die van de wand weggaat en koude vloeistof die juist naar de wand toegaat verschillende moleculaire Prandtl-getallen hebben is gebruikt om een nieuwe analogie tussen het Nusselt-getal en de wrijvingsfactor af te leiden. Deze nieuwe analogie is gevalideerd aan de hand van verschillende experimenten uit de literatuur. De vergelijking tussen de resultaten van de nieuwe analogie en de experimenten suggereert dat een dergelijke analogie valide zijn kan bij lage verhoudingen tussen de warmteflux en de massafux . Dit resultaat kan helpen in het ontwikkelen van betere warmteoverdrachtsmodellen.

CONTENTS

| | |
|---|----|
| ABSTRACT | v |
| SAMENVATTING | ix |
| 1 INTRODUCTION | 1 |
| 1.1 The state of the world | 1 |
| 1.2 Enhanced thermodynamic cycles | 2 |
| 1.3 Supercritical fluids | 3 |
| 1.4 Thesis goals and outline | 6 |
| 2 NUMERICAL METHODS | 9 |
| 2.1 Governing equations | 9 |
| 2.2 Discretisation | 11 |
| 2.2.1 Spatial discretisation | 11 |
| 2.2.2 Temporal discretisation | 12 |
| 2.3 Thermophysical properties | 13 |
| 2.4 Sub-critical validations | 14 |
| 2.4.1 Annular geometry | 14 |
| 2.4.2 Variable density | 15 |
| 2.5 Super-critical tests | 15 |
| 2.5.1 Conservation of mass and energy | 16 |
| 2.6 Summary | 18 |
| 3 TURBULENCE ATTENUATION | 21 |
| 3.1 Introduction | 21 |
| 3.2 Cases | 23 |
| 3.3 Mean statistics | 25 |
| 3.3.1 Mean thermophysical property statistics | 25 |
| 3.3.2 Velocity profiles | 28 |
| 3.3.3 Turbulent shear stress | 28 |
| 3.3.4 Turbulence intensities | 32 |

| | | |
|-------|--|-----|
| 3.3.5 | Local Reynolds number effect | 33 |
| 3.3.6 | Production of turbulent kinetic energy | 34 |
| 3.4 | Structures | 35 |
| 3.4.1 | Generation of near wall streaks | 36 |
| 3.4.2 | Generation of stream-wise vortical motions | 45 |
| 3.4.3 | Molecular Prandtl number effect | 51 |
| 3.5 | Conclusions | 55 |
| 4 | HEAT TRANSFER ATTENUATION | 61 |
| 4.1 | Introduction | 61 |
| 4.2 | Numerical cases | 61 |
| 4.3 | Mean statistics | 63 |
| 4.3.1 | Mean thermophysical property and velocity statistics | 63 |
| 4.3.2 | Mean thermal statistics | 67 |
| 4.3.3 | Heat fluxes | 71 |
| 4.3.4 | Turbulent heat flux transport equation | 73 |
| 4.4 | Nusselt relation | 76 |
| 4.4.1 | Influences of the heat fluxes on the Nusselt number | 76 |
| 4.4.2 | Heat flux events and characteristics | 79 |
| 4.5 | Conclusions | 86 |
| 5 | TOWARDS A NEW MODEL | 91 |
| 5.1 | Introduction | 91 |
| 5.2 | The model | 91 |
| 5.2.1 | Concept | 91 |
| 5.2.2 | Derivation | 93 |
| 5.2.3 | Creating a relation | 96 |
| 5.3 | Results | 98 |
| 5.3.1 | A demonstration | 98 |
| 5.3.2 | Low heat flux | 99 |
| 5.3.3 | Comparisons | 100 |
| 5.4 | Discussion | 102 |
| 6 | CONCLUSIONS. | 105 |
| | ACKNOWLEDGEMENTS. | 109 |
| | LIST OF PUBLICATIONS | 111 |
| | CURRICULUM VITAE. | 113 |

| | |
|---|-----|
| APPENDIX | 115 |
| A.1 Derivations | 115 |
| A.1.1 Low Mach number approximation | 115 |
| A.1.2 Pressure in a simultaneously heated and cooled periodic annulus | 116 |
| A.1.3 Derivation of the momentum-vorticity equation | 117 |
| A.1.4 Fourier's law in terms of the enthalpy | 118 |
| A.1.5 Derivation of the Nusselt number relation | 119 |
| A.2 Tensors and dyadics | 121 |
| A.2.1 Curl of the divergence of a second order tensor | 121 |
| A.2.2 Curl of a gradient- vector- dyadic tensor | 121 |
| A.2.3 Curl of the transpose of a gradient- vector- dyadic tensor | 122 |
| A.2.4 Curl of a tensor multiplied by a scalar | 122 |
| A.2.5 Divergence of the curl of the identity tensor multiplied by a scalar | 123 |
| A.2.6 Dot product of a vector \mathbf{v} and the divergence of a second order tensor \mathbf{T} | 124 |
| A.2.7 Outer product between a vector and a second order tensor in cylindrical coordinates | 124 |
| A.3 Additional case details | 126 |
| A.3.1 Mesh generation | 126 |
| A.3.2 Enthalpy power spectra | 126 |

CHAPTER 1

INTRODUCTION

1.1 The state of the world

The world population has rapidly grown in the last century. In recent years alone, between the year 1990 and 2010, the population has increased by 30%, or 1.6 billion human beings according to the United Nations Department of Economic and Social Affairs [2015]. Due to this population growth, but also due to economic growth and industrialization, the world energy demand has increased in the same time by approximately 50% as is reported by the International Energy Agency [2015]. Projections indicate that the world population will increase to 9.7 billion in 2050 and that the electricity demand will increase by 70% in 2040. In order to maintain or even increase standards of living of the world population, it is important that the increase in electricity demand will be met with increased production of electricity.

Currently, burning fossil fuels, such as coal, (natural) gas and (fuel) oil, is the primary source of electricity worldwide. However, burning fossil fuels is also associated with the emission of greenhouse gases, such as CO_2 , into the atmosphere. The accumulation of such gases in the atmosphere results in an enhanced greenhouse effect as they will absorb thermal radiation emitted by the earth and re-emit a part of the absorbed radiation back toward the earth, which results in higher surface temperatures and lower- atmosphere-temperatures. A rise of $2.5\text{ }^\circ\text{C}$ in global mean temperature in the current century was predicted in the late last century by Hansen et al. [1981]. More recently, however, the International Panel on Climate Change [2014] presented projections showing an increase in global mean temperature ranging from $3.7\text{ }^\circ\text{C}$ to $4.8\text{ }^\circ\text{C}$ over the course of this century if greenhouse gas emissions are not mitigated. A rise in global mean temperature is unwanted as it can have dire consequences to global society, such as a rise in sea-levels, reduced crop yield, an increased rate of occurrence of heat waves or extreme weather and changes in flora and fauna. It is therefore vital that electricity production methods that emit less greenhouse gases are researched and subsequently implemented into society.

1.2 Enhanced thermodynamic cycles

The International Energy Agency [2015] reports that *"energy efficiency plays a critical role in limiting world energy demand growth to one-third by 2040."* Therefore, future energy systems should not only have low greenhouse gas emissions, but should also be highly energy efficient. Two examples of low greenhouse gas emission energy systems are concentrated solar power plants and nuclear power plants. Such energy systems rely on classical sub-critical steam cycles. Modern sub-critical steam cycles for concentrated power plants typically operate with a thermal efficiency of 37%-42%, according to Dunham and Iverson [2014]. Nuclear power plants that are currently in operation typically have a lower thermal efficiency of 33% to 35% (see for instance Piro et al. [2004]). These efficiencies are rather low when compared to modern fossil-fuelled power plants, which run at an efficiency in the range of 45%-50%, as such power plants typically operate at supercritical pressure. Supercritical pressure steam cycles allow for higher temperatures and pressure, which can increase the thermal efficiency to above 45%. The difference between a supercritical steam cycle and a sub-critical one is schematically represented in figure 1.1(a). The main difference between the two cycles is that in a supercritical cycle during the heating phase, indicated in the figure by 4-1, the working fluid does not enter the vapour/liquid coexistence region as is the case in a sub-critical steam cycle. In other words, no vapour is formed in the supercritical cycle.

Applying supercritical cycles to concentrated solar power plants or nuclear power plants results in highly efficient energy systems with low greenhouse gas emissions. In fact, new designs for concentrated solar power plants and nuclear power plants already exist. For instance, the High Performance Light Water Reactor, a new nuclear reactor concept, is designed to use a supercritical steam cycle and it is envisioned to have a thermal efficiency of 44 % as is stated by Schulenberg et al. [2011], which is substantially higher than nuclear power plants that are in operation today. Due to the supercritical conditions of the design, steam generators, steam separators and dryers are unnecessary, which is also advantageous when compared to older nuclear reactor designs. Dunham and Iverson [2014] mention that supercritical steam cycles are also considered for modern concentrated solar power plants.

Another thermodynamic cycle that has a high thermal efficiency (in the range of 50% according to Iverson et al. [2013]) is the supercritical carbon dioxide Brayton cycle. This cycle is similar to the sub-critical Brayton cycle, except for the fact that the working fluid is in the supercritical phase for the whole cycle rather than in the gaseous phase, as is shown in 1.1(b). In this cycle, the work that is done by the compressor is reduced due to the supercritical conditions, as was found by Angelino [1967]. This cycle is also considered for both concentrated solar power plants (see Iverson et al. [2013] or Garg

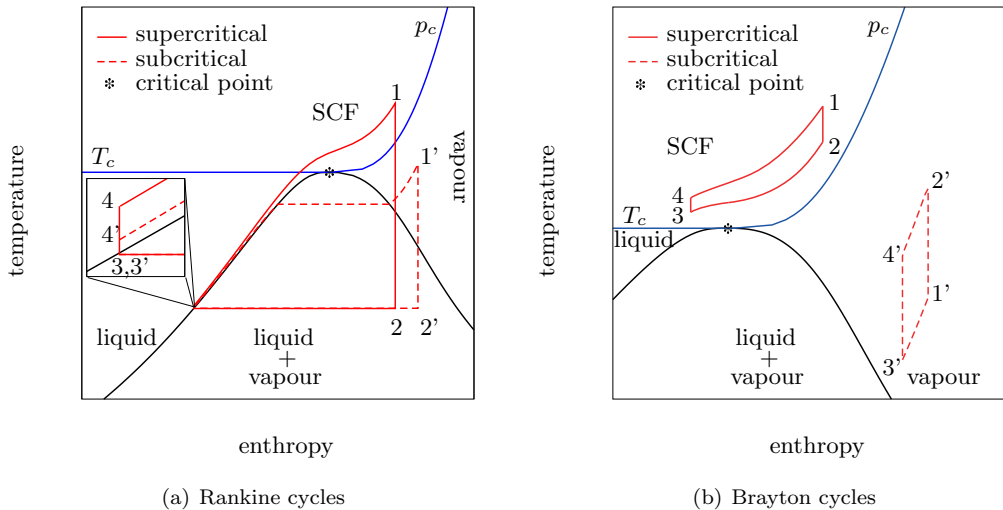


Figure 1.1: a) ideal Rankine cycles. The processes are as follows: 1–2: isentropic expansion, 2–3: cooling of the working fluid at constant pressure, 3–4: isentropic compression, 4–1: heating of the working fluid at constant pressure. Accents are reserved for the subcritical cycle. Points 3 and 3' coincide. b) ideal Brayton cycles. The processes are the same as in the Rankine cycle, except that they occur at different temperatures and entropies. The black line represents the saturation curve, while the blue lines represent the critical temperature isotherm and the critical isobar, denoted as T_c and p_c , respectively. SCF denotes the supercritical fluid phase.

et al. [2013]) and nuclear power plants (see Dostal et al. [2004]).

In short, more efficient energy systems can be developed if supercritical steam/ CO_2 cycles are used. However, the current knowledge of the behaviour of heat transfer to supercritical fluids is rather limited, which will be discussed below.

1.3 Supercritical fluids

At sub-critical pressure, vapour and liquid can coexist in equilibrium. This occurs for certain combinations of the pressure and the temperature. The collection of these combinations is known as the saturation curve. The maximum of this curve is the critical point, see figure 1.2. At this point, the distinction between vapour and liquid does not exist. Above the critical values of pressure and temperature, a fluid is supercritical, see for instance Zappoli et al. [2015].

Supercritical fluids have unique properties. For instance, supercritical fluids have a large isothermal compressibility, which is beneficial to the CO_2 Brayton cycle that was mentioned in the previous section. Moreover, when a fluid at supercritical pressure

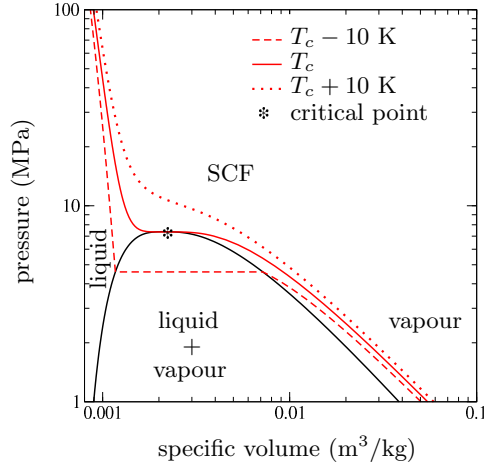


Figure 1.2: Pressure – specific volume diagram of CO_2 . The saturation curve is shown in black. SCF stands for supercritical fluid, while T_c denotes the critical temperature. The red lines are isotherms.

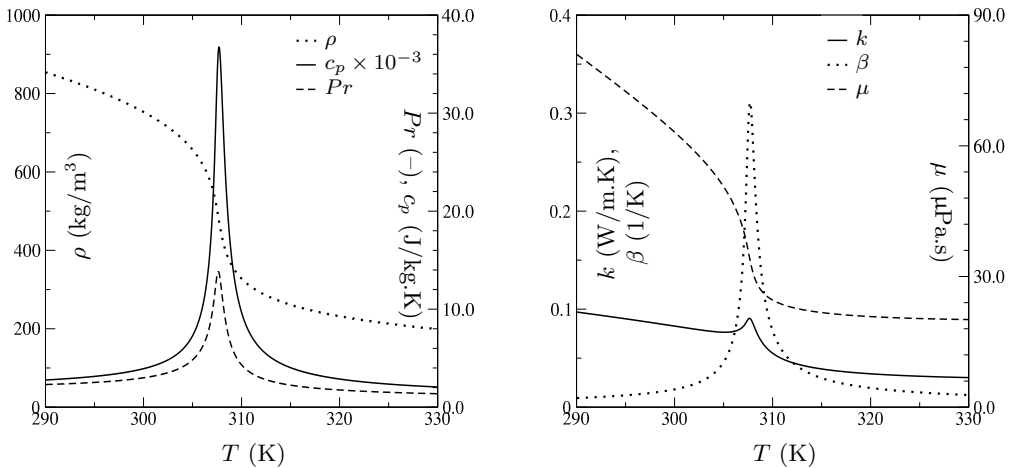


Figure 1.3: Properties of CO_2 at 8 MPa. Shown are the density ρ (kg/m^3), the specific heat capacity c_p ($\text{J}/\text{kg}\cdot\text{K}$), the molecular Prandtl number Pr (-), the thermal conductivity k ($\text{W}/\text{m}\cdot\text{K}$), the dynamic viscosity μ ($\mu\text{Pa}\cdot\text{s}$) and the thermal expansivity at constant pressure β ($1/\text{K}$). The thermo-physical properties have been obtained from the equation of state by Kunz et al. [2007] as well as equations from Fenghour et al. [1998] and Vesovic et al. [1990] and by using the NIST standard reference database by Lemmon et al. [2013].

is heated, it transitions from a fluid with liquid-like properties to a fluid with gas-like properties, without undergoing a phase change, which is beneficial to the supercritical steam cycle, as was mentioned in the previous section. The temperature about which this *continuous* transition occurs is called the pseudo-critical temperature T_{pc} , which is defined as the temperature for which the specific heat capacity has its maximum value. Close to the pseudo-critical temperature, the thermophysical properties vary sharply with temperature. This is, for instance, true for CO_2 as well as for water. The thermophysical properties of CO_2 at 8 MPa are shown in figure 1.3. As temperature increases, the density decreases as does the dynamic viscosity. The density and dynamic viscosity variation with temperature is strongest around $T_{pc} = 307.7\text{K}$. The specific heat capacity, Prandtl number and the thermal expansivity show a maximum at T_{pc} . Finally, the thermal conductivity decreases with temperature, but also shows a maximum at T_{pc} .

In most heat transfer applications, fluid flows are in a turbulent state and are heated (or cooled) by a hot (or cold) surface. The variation in thermophysical properties can have a significant effect on (turbulent) heat transfer to or from that surface. The effects of the thermophysical properties are two-fold. First of all, the variation in density and dynamic viscosity can affect the (turbulent) motion of the fluid and therefore also heat transfer. Secondly, heat transfer may be directly affected by variations in the density, the specific heat capacity, as well as the thermal conductivity. Heat transfer to supercritical fluids has been broadly categorised into three regimes:

- normal: the heat transfer is *comparable* to heat transfer in a similar situation, but with a fluid that has constant thermophysical properties
- enhanced: the heat transfer is *larger* than heat transfer in a similar situation, but with a fluid that has constant thermophysical properties
- deteriorated: the heat transfer is *smaller* than heat transfer in a similar situation, but with a fluid that has constant thermophysical properties

The enhanced heat transfer effect can be so strong, that it can cause a local drop in surface temperatures. On the other hand, the deteriorated heat transfer effect can be so strong, that it causes a local rise in surface temperature. These characteristics of heat transfer at supercritical pressure are not satisfactorily captured by both heat transfer correlations (see for instance Piore et al. [2004] and computational fluid dynamics with turbulence modelling (see Sharabi and Ambrosini [2009]), because these methods have either been developed for sub-critical pressure conditions, or perhaps because they have been developed without fully understanding the mechanisms behind heat transfer at supercritical pressures. According to a recent review on heat transfer at supercritical pressure by Yoo [2013] “*there has been no consensus on the general trends in supercritical*

heat transfer, particularly with regard to turbulent flow.” However, an enhanced understanding of heat transfer to fluids at supercritical pressure is of vital importance to a safe and optimised design of any heat transfer equipment meant to operate at supercritical pressure.

1.4 Thesis goals and outline

The aim of this thesis is to elucidate mechanisms that can lead to heat transfer enhancement or deterioration. The tools of choice for this investigation are computational fluid dynamics methods without using turbulence models, i.e., Direct Numerical Simulation techniques. Because the thermophysical properties may affect both the turbulent motion of the fluids and the heat transfer directly, this thesis aims to investigate both how turbulence is affected and how heat transfer is affected by variable thermophysical properties. As (concentric) annuli are geometries that are commonly found in heat transfer equipment, mostly annular turbulent flows are studied.

The outline of this thesis is as follows. **Chapter 2** documents the numerical methods that are used for the direct numerical simulations, such as the time-integration scheme, the spatial discretisation schemes as well as code-to-code validations, code-to-experiment validations and numerical tests.

In **chapter 3**, five different numerical simulations are described which are subsequently analysed in order to investigate turbulence attenuation in heated turbulent annular flows at supercritical pressure. Firstly, the mean attenuation of mean statistics by variations in the density and dynamic viscosity is investigated. Secondly, the attenuation of turbulent structures that are part of the near wall cycle in turbulent flows is studied.

In **chapter 4**, attention is given to the effect of the other variable thermophysical properties on turbulent heat transfer; the specific heat capacity, the thermal diffusivity, the Prandtl number, but also the density. Differences between enthalpy and temperature fluctuations in supercritical conditions are explained using probability density functions. Differences between turbulent heat transfer at sub-critical pressure (constant thermophysical properties) and turbulent heat transfer at supercritical pressure are explained by examining the budgets of heat flux transport equations as well as turbulent heat flux quadrants.

A new semi-analytical model for predicting heat transfer at supercritical pressure is presented in **chapter 5**. This model starts from the observation that the total heat flux consists of a conductive part as well as a turbulent part, but that the latter has the largest contribution to heat transfer.

The main conclusions of the work are summarised in **Chapter 6**. At the end of this thesis, various appendices can be found that present supplementary material.

Bibliography

- A. Angelino. Perspectives for the liquid phase compression gas turbine. *J. Eng. Power*, 89:229–236, 1967.
- V. Dostal, M.J. Driscoll, and P. Hejzlar. *A Supercritical Carbon Dioxide Cycle for Next Generation Nuclear Reactors*. PhD thesis, MIT, 2004.
- M.T. Dunham and B.D. Iverson. High-efficiency thermodynamic power cycles for concentrated solar power systems. *Renewable and Sustainable Energy Reviews*, 30:758–770, 2014.
- A. Fenghour, W. A. Wakeham, and V. Vesovic. The viscosity of carbon dioxide. *Journal of Physical and Chemical Reference Data*, 27:31–44, 1998.
- P. Garg, P. Kumar, and K. Srinivasan. Supercritical carbondioxide brayton cycle for concentrated solar power. *Journal of Supercritical fluids*, 76:54–60, 2013.
- J. Hansen, D. Johnson, A. Lacis, S. Lebedeff, P. Lee, D. Rind, and G. Russel. Climate impact of increasing atmospheric carbon dioxide. *Science*, 213(4511):957–966, 1981.
- International Energy Agency. World Energy Outlook. Technical report, 2015. <http://www.worldenergyoutlook.org>.
- International Panel on Climate Change. Climate Change Synthesis Report 2014. Summary for Policymakers. Technical report, 2014.
- B.D. Iverson, T.M. Conboy, J.J. Pasch, and A.M. Kruiuzenga. Supercritical co2 brayton cycles for solar-thermal energy. *Applied Energy*, 111:957–970, 2013.
- O. Kunz, W. Wagner R. Klimeck, and M. Jaeschke. The GERG-2004 wide-range equation of state for natural gases and other mixtures. Technical report, 2007. GERG Technical Monograph 15, Fortschritt-Berichte VDI, VDI-Verlag, Düsseldorf.
- E.W. Lemmon, M.L. Huber, and M.O. McLinden. NIST standard reference database 23: Reference fluid thermodynamic and transport properties-REFPROP. Version 9.1, National Institute of Standards and Technology, Standard Reference Data Program, Gaithersburg, 2013.
- I.L. Piore, H.F. Khartabil, and R.B. Duffey. Heat transfer to supercritical fluids flowing in channels—empirical correlations (survey). *Nuclear Engineering and Design*, 230: 69–91, 2004.

- T. Schulenberg, J. Starflinger, P. Marsault, D. Bittermann, C. Maráczy, E. Laurien, L.A. Lycklama à Nijeholt, H. Anglart, H. Andreani, M. Ruzickovai, and A. Toivonen. European supercritical water cooled reactor. *Nuclear Engineering and Design*, 241: 3505–3513, 2011.
- M. Sharabi and W. Ambrosini. Discussion of heat transfer phenomena in fluids at supercritical pressure with the aid of CFD models. *Annals of Nuclear Energy*, 36:60, 2009.
- United Nations Department of Economic and Social Affairs. World Population Prospects. The 2015 Revision. Key Findings and Advance Tables. Technical report, 2015. ESA/P/WP.241.
- V. Vesovic, W. Wakeham, G. Olchowiy, J. Sengers, J. Watson, and J. Millat. The transport properties of carbon dioxide. *Journal of Physical and Chemical Reference Data*, 19:763, 1990.
- J.Y. Yoo. The turbulent flows of supercritical fluids with heat transfer. *Annual Review of Fluid Mechanics*, 45(1):495–525, 2013.
- B. Zappoli, D. Beysens, and Y. Garrabos. *Heat transfers and related effects in supercritical fluids*. Springer, 2015.

CHAPTER 2

NUMERICAL METHODS

It is well accepted within the scientific community that the Navier-Stokes equations are a valid description of the motion of a fluid with constant thermophysical properties. Our aim, however, is to investigate the effect of variable thermophysical properties on turbulence and heat transfer. We will therefore start this chapter with a short remark on the validity of the Navier-Stokes equations with respect to the goals that were set in the introduction. Subsequently, numerical methods that are employed in order to solve the governing equations for heated turbulent fluids at super-critical pressure will be presented. These methods were used to rewrite a numerical program that was suitable to solve the incompressible Navier-Stokes equations, see Boersma [2011], to a program that is tailored to solve the low Mach number approximation of the Navier-Stokes equations. The numerical methods will be tested and validated at the end of the chapter.

2.1 Governing equations

The Navier-Stokes equations can only describe a heated turbulent fluid flow accurately if such a flow may be considered to be in local thermodynamic equilibrium. This assumption is valid for length scales Λ that are larger than the correlation length scale ξ ; a length scale that is associated with density fluctuations that arise due to variations in the number of molecules in a given volume. Under the assumption that $\Lambda > \xi$, the fluid state is described by the hydrodynamic conservation equations for a low Mach number fluid (Zappoli et al. [2015]). Experiments that were performed by Nishikawa and Tanaka [1995] in order to calculate ξ in supercritical CO_2 suggest that this assumption is reasonable.

It was mentioned in the introduction that this study will be limited to low Mach number applications. Therefore, the low Mach number approximation of the Navier Stokes equations is numerically solved to simulate heated and (or) cooled flows at supercritical pressure in cylindrical geometries. The low Mach number approximation has previously been used by Bae et al. [2005, 2008], Nematı et al. [2015] and Patel et al. [2015] to simu-

late such flows and a derivation of this approximation can be found in appendix A.1.1. In the low Mach number limit of the Navier Stokes equations, the effect of acoustic waves on the solution is neglected. The pressure is decomposed into a thermodynamic part $p_0(t)$ and a hydrodynamic part $p_{hy}(t)$. The thermodynamic pressure is considered to be constant. The fluctuations of the hydrodynamic pressure are assumed to be very small compared to the thermodynamic pressure so that all thermophysical property variations due to hydrodynamic pressure fluctuations can be neglected. Therefore, all thermophysical properties can be evaluated as a function of the enthalpy only. Well above the critical pressure, the speed of sound shows a minimum at the pseudo-critical temperature. For $s\text{CO}_2$ at 8 MPa, the minimum value of the speed of sound is 179 m/s. Thus when considering bulk velocities of 1 m/s, the Mach number is even less than 0.01, which validates the use of the low Mach number approximation.

Using dyadic notation and denoting a vector with a bold symbol, while denoting a second order tensor with a capital bold symbol, the governing equations for conservation of mass, momentum and enthalpy in non-dimensional form read:

$$\partial_t \rho + \nabla \cdot \rho \mathbf{u} = 0, \quad (2.1)$$

$$\partial_t(\rho \mathbf{u}) + \nabla \cdot (\rho \mathbf{u} \mathbf{u}) = -\nabla p_{hy} + Fr^{-1} \rho \hat{\mathbf{z}} + Re^{-1} \nabla \cdot 2\mu \mathbf{S} + \Phi, \quad (2.2)$$

where,

$$\mathbf{S} \equiv 1/2(\nabla \mathbf{u} + (\nabla \mathbf{u})^T) - 1/3(\nabla \cdot \mathbf{u})\mathbf{I}$$

and

$$\partial_t(\rho h) + \nabla \cdot \rho \mathbf{u} h = (RePr_h)^{-1} \nabla \cdot k \nabla T, \quad (2.3)$$

in which ρ is the density, $\mathbf{u} = (u, v, w)^T$ the velocity, Fr the Froude number, $\hat{\mathbf{z}}$ the stream-wise unit vector, Re the Reynolds number, μ the dynamic viscosity, \mathbf{S} the deviatoric stress tensor, $\Phi = (0, 0, \Phi)^T$ with Φ being the driving force, \mathbf{I} the identity tensor, h the enthalpy, Pr_h the reference Prandtl number based on a ratio of an enthalpy difference and a temperature difference, k the thermal conductivity and T the temperature. All variables in the above presented equations are scaled with bulk quantities, i.e. the spatial coordinates are scaled with the hydraulic diameter D_h^o , the velocity with the bulk stream-wise velocity w_b^o , and the time was scaled with D_h^o/w_b^o . The superscript o denotes a dimensional quantity. All thermophysical properties were scaled with their respective values at the pseudo-critical point, i.e. $\rho = \rho^o/\rho_{pc}^o$ and $\mu = \mu^o/\mu_{pc}^o$, where the subscript pc denotes a property at the pseudo-critical temperature. The hydrodynamic pressure is therefore scaled with $\rho_{pc}^o w_b^o{}^2$. Both the enthalpy and the temperature have been non-dimensionalised such that $0 \leq h \leq 1$ and $0 \leq T \leq 1$:

$$h = \frac{h^o - h_{cold}^o}{\Delta h^o}, \quad T = \frac{T^o - T_{cold}^o}{\Delta T^o}, \quad (2.4)$$

where T_{cold}^o represents the lowest possible temperature in the system and where h_{cold}^o equals $h^o(T_{cold}^o)$. $\Delta T = T_{hot}^o - T_{cold}^o$, where T_{hot}^o is the highest possible temperature. Similarly, $\Delta h^o = h^o(T_{hot}^o) - h^o(T_{cold}^o)$. By scaling the conservation equations in this manner, the Reynolds, Prandtl and Froude numbers are defined as:

$$Re \equiv \frac{\rho_{pc}^o w_b^o D_h^o}{\mu_{pc}^o}, \quad Pr_h \equiv \frac{\mu_{pc}^o \Delta h^o}{k_{pc}^o \Delta T^o}, \quad Fr \equiv \frac{w_b^{o2}}{g^o D_h^o}, \quad (2.5)$$

where g^o represents the magnitude of the gravitational vector. $g^o = 9.81 \text{ m/s}^2$, $\rho_{pc}^o = 4.75 \cdot 10^2 \text{ kg/m}^3$, $\mu_{pc}^o = 3.37 \cdot 10^{-5} \text{ Pa}\cdot\text{s}$ and $k_{pc}^o = 9.04 \cdot 10^{-2} \text{ W/mK}$, see Kunz et al. [2007] and equations from Fenghour et al. [1998] and Vesovic et al. [1990].

2.2 Discretisation

In the numerical model, the low Mach number approximation of the Navier-Stokes equation must be discretised in both time and space, before a solution for the momentum and the enthalpy can be obtained.

2.2.1 Spatial discretisation

As we envision to investigate an annular geometry, the flow domain is best described by cylindrical coordinates. Any derivatives with respect to the radial direction are discretised using a 6th order staggered compact finite difference scheme that was previously outlined by Boersma [2011]. Derivatives with respect to the circumferential direction and the stream-wise direction are calculated using a pseudo-spectral method. In order to enhance the stability of the numerical model, the diffusive terms of the momentum- and enthalpy equations are written in a non-conservative form. The diffusive terms are written as:

$$\nabla \cdot k \nabla T = k \nabla^2 T + \nabla k \cdot \nabla T \quad (2.6)$$

$$\nabla \cdot 2\mu \mathbf{S} = 2\mu \nabla \cdot \mathbf{S} + 2\nabla \mu \cdot \mathbf{S} \quad (2.7)$$

To avoid aliasing errors, a skew-symmetric formulation is used for the convective terms of the Navier-Stokes equations. For a convective term with three independent variables, numerous skew-symmetric formulations (both quadratic and cubic) are possible, see Kennedy and Gruber [2008]. In the current study, the quadratic formulation, reported by Feiereisen et al. [1981], was adopted:

$$\nabla \cdot (\rho u h) = \frac{1}{2} \nabla \cdot (\rho u h) + \frac{1}{2} \rho \mathbf{u} \cdot \nabla h + \frac{1}{2} h \nabla \cdot \rho \mathbf{u} \quad (2.8)$$

$$\nabla \cdot (\rho u u) = \frac{1}{2} \nabla \cdot (\rho u u) + \frac{1}{2} \rho \mathbf{u} \cdot \nabla \mathbf{u} + \frac{1}{2} \mathbf{u} (\nabla \cdot \rho \mathbf{u}) \quad (2.9)$$

This formulation was found to be computationally inexpensive, while yielding stable solutions.

2.2.2 Temporal discretisation

To obtain a solution for the momentum $\rho\mathbf{u} = (\rho u, \rho v, \rho w)^T$, which represent the radial, circumferential and stream-wise direction respectively, and for the values of ρh , equations (2.2) and (2.3) are numerically integrated using the following algorithm. First, the enthalpy transport equation is integrated using a second order Adams-Bashford (explicit) time integration scheme;

$$(\rho h)^{n+1} = (\rho h)^n + \Delta t \left[\frac{3}{2}(\mathcal{A}(h))^n - \frac{1}{2}(\mathcal{A}(h))^{n-1} \right], \quad (2.10)$$

where $\mathcal{A}(h)$ represents the diffusion and convective parts of equation (2.3). The density at time step $n + 1$, ρ^{n+1} , cannot be determined from $(\rho h)^{n+1}$ directly. An intermediate step is therefore required. An estimate ρ^* of ρ^{n+1} is calculated as is detailed by Najm et al. [1998]:

$$\rho^* = \rho^n + \Delta t \left[\frac{3}{2} \left(\frac{\partial \rho}{\partial t} \right)^n - \frac{1}{2} \left(\frac{\partial \rho}{\partial t} \right)^{n-1} \right] \quad (2.11)$$

The enthalpy at $n + 1$ is then estimated as $h^{n+1} = (\rho h)^{n+1} / \rho^*$. Subsequently, ρ^{n+1} is then calculated from h^{n+1} , which will be detailed later in this chapter. Advancing the momentum is done using an algorithm closely reminiscent of the method employed by McMurtry et al. [1986]. First, we will require that equation (2.1) holds for every solution at $n + 1$, or:

$$(\partial_t \rho)^{n+1} + \nabla \cdot (\rho \mathbf{u})^{n+1} = 0 \quad (2.12)$$

Because the enthalpy transport equation is advanced first, ρ^{n+1} is known, which means that a second order accurate estimate of $(\partial_t \rho)^{n+1}$ can be calculated:

$$(\partial_t \rho)^{n+1} = (\Delta t)^{-1} \left[\frac{3}{2} \rho^{n+1} - 2\rho^n + \frac{1}{2} \rho^{n-1} \right] \quad (2.13)$$

Second, the momentum equation will be advanced, while completely disregarding the pressure gradient, yielding an intermediate solution for the momentum $(\rho \mathbf{u})^*$;

$$(\rho \mathbf{u})^* = (\rho \mathbf{u})^n + \Delta t \left[\frac{3}{2}(\mathcal{A}(\mathbf{u}))^n - \frac{1}{2}(\mathcal{A}(\mathbf{u}))^{n-1} \right] \quad (2.14)$$

The 'remainder' of the momentum equation is given by:

$$(\rho \mathbf{u})^{n+1} = (\rho \mathbf{u})^* - \Delta t \nabla p^{n+1} \quad (2.15)$$

Taking the divergence of equation (2.15), yields Poisson's equation:

$$\nabla \cdot (\rho \mathbf{u})^{n+1} = \nabla \cdot (\rho \mathbf{u})^* - \Delta t \nabla^2 p^{n+1}. \quad (2.16)$$

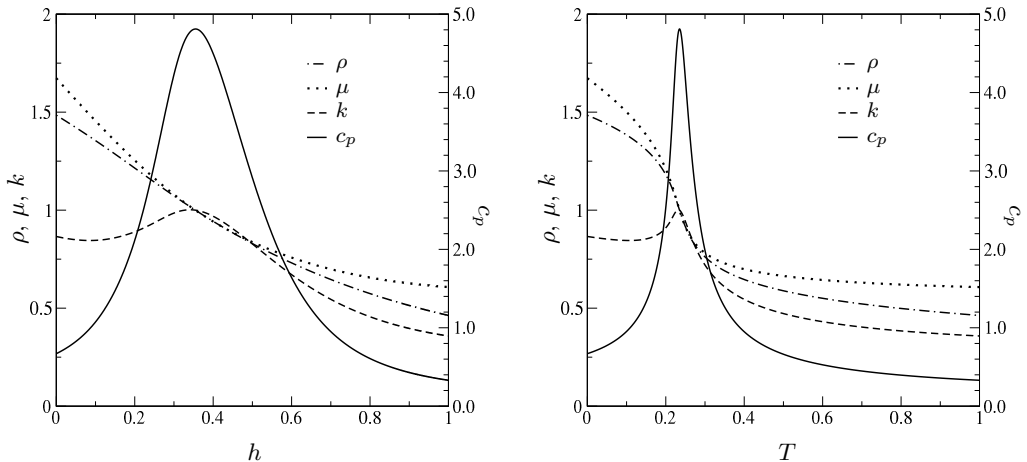


Figure 2.1: Non-dimensional properties of CO₂ at 8 MPa. Shown are the density ρ , the specific heat capacity c_p , the thermal conductivity k , and the dynamic viscosity μ as a function of the enthalpy h (left) and the temperature T (right).

Equation (2.16) is rewritten using that $-\nabla \cdot (\rho \mathbf{u})^{n+1}$ must be equal to equation (2.13);

$$\nabla^2 p^{n+1} = \frac{(\Delta t)^{-1} \left[\frac{3}{2} \rho^{n+1} - 2\rho^n + \frac{1}{2} \rho^{n-1} \right] + \nabla \cdot (\rho \mathbf{u})^*}{\Delta t} \quad (2.17)$$

Equation (2.17) is solved using second order implicit scheme to obtain p^{n+1} , after which $(\rho \mathbf{u})^{n+1}$ is obtained using equation 2.15.

2.3 Thermophysical properties

In the previous section, it was mentioned that the density is calculated as a function of the enthalpy. In fact, the density, dynamic viscosity, thermal conductivity and temperature are calculated at each time step (as soon as h^{n+1} is known) using a 3rd order spline interpolation along an isobar, as a function of the enthalpy h . Tabulated values of T, ρ, μ, k have been pre-computed using the Helmholtz equation of state by Kunz et al. [2007] and the equations by Fenghour et al. [1998] and Vesovic et al. [1990], which are included in the NIST standard reference database (Lemmon et al. [2013]). Calculating the thermophysical properties as a function of the enthalpy is advantageous compared to calculating them as a function of the temperature; the non-dimensional thermophysical properties show less steep variation around the pseudo-critical temperature with increasing non-dimensional enthalpy than they do with increasing temperature, as is shown in figure 2.1.

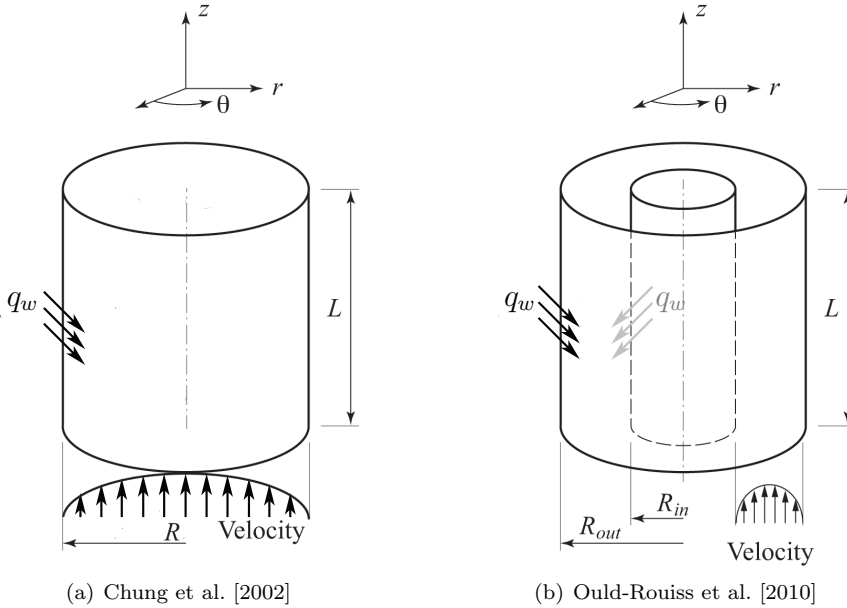


Figure 2.2: Configurations of Chung et al. [2002] and Ould-Rouiss et al. [2010]. Left: an annular geometry with a constant wall heat flux at the inner and the outer wall. Right: a pipe geometry with a constant heat flux at the wall.

2.4 Sub-critical validations

The numerical methods that were described in the previous section are validated against both heated turbulent flows in an annular geometry at different Prandtl numbers as well as a heated turbulent flow with variable density effects.

2.4.1 Annular geometry

The first validation case concerns a turbulent heated flow in an annular geometry. The configuration is shown in figure 2.2(a). Simulations were run at a Reynolds number of $Re=8900$ with Prandtl numbers of $Pr=0.71$ (on a $144 \times 288 \times 288$ mesh) and $Pr=7$ (on a $192 \times 576 \times 576$ mesh). Results of the turbulent intensities are compared in figures 2.3(a) and 2.3(b) with results reported by Chung et al. [2002] and Ould-Rouiss et al. [2010]. The comparison shows that there is good agreement between the current numerical methods and the results reported by Chung et al. [2002] and Ould-Rouiss et al. [2010].

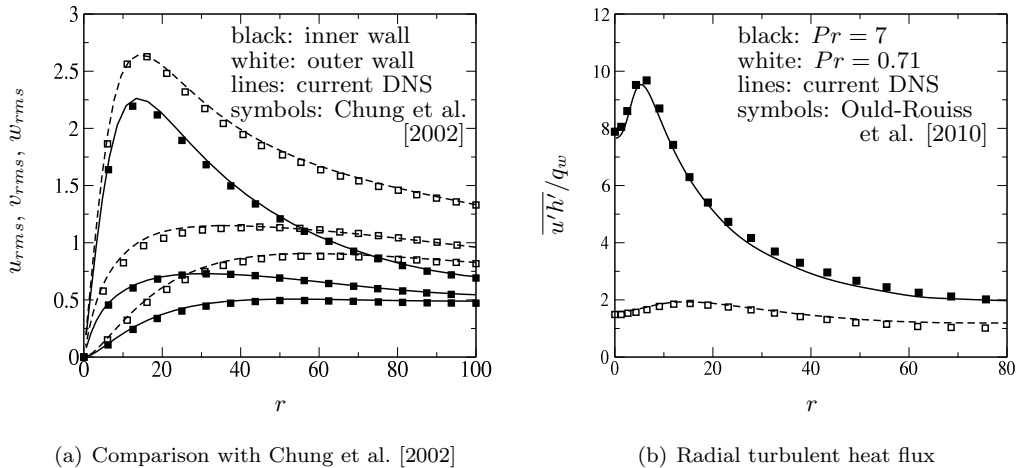


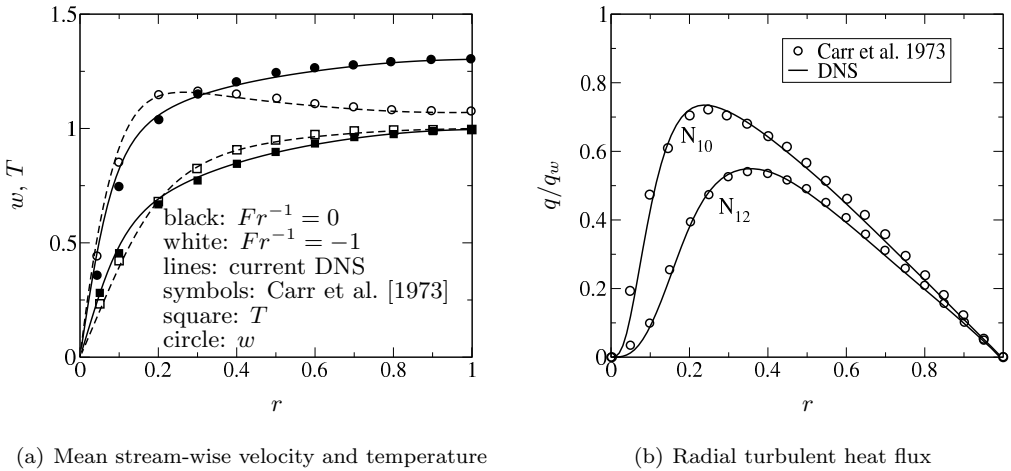
Figure 2.3: Comparison between the current DNS code, Chung et al. [2002] as well as Ould-Rouiss et al. [2010]. On the left, velocity intensities near the inner and outer wall of an annular geometry. On the right, temperature intensities near the inner wall for two different Prandtl numbers, Pr .

2.4.2 Variable density

The numerical methods that were discussed before were previously validated by Patel et al. [2015] against variable density channel flow results that were presented by Nicoud [2000]. Because the effect of buoyancy is also studied in this present study, the code was validated against two experiments by Carr et al. [1973]. In these experiments, annotated as N_{10} and N_{12} , upward flowing air (at a bulk Reynolds number of 5300) is heated in a pipe at atmospheric pressure, see figure 2.2(b). The same configuration was simulated using the numerical methods that were described earlier, using a mesh with $128 \times 256 \times 256$ grid points and a domain length of six hydraulic diameters. Mean velocity and temperature measurements are compared with the results from the Direct Numerical Simulation in figure 2.4(a) and the turbulent heat flux is compared in figure 2.4(b). The results validate the code, since there is good agreement between the DNS results and the measured experimental data.

2.5 Super-critical tests

In the previous section, it was shown that the numerical methods described in this chapter yield results that are in line with numerical simulations and experiments of heat transfer



(a) Mean stream-wise velocity and temperature

(b) Radial turbulent heat flux

Figure 2.4: Comparison between the current DNS-code and the experiment described by Carr et al. [1973]. The symbols denote experimental values, while the lines represent results of direct numerical simulations.

at sub-critical pressure, that were previously reported in literature. However, before discussing how variable thermophysical properties of a fluid at super-critical pressure attenuate turbulence (which will be done in the next chapter), it is useful to test the validity of the code also in a configuration at super-critical pressure. We will consider a configuration that will be investigated in the next chapter. The configuration is shown in figure 2.5(a). The annulus is similar to the one described before, except that the walls are kept at a constant temperature. Two cases are considered here. The first is a reference case with constant properties. The second is a case where the thermophysical properties correspond to that of CO_2 at 8 MPa, with $T_h = 323$ K, $T_c = 303$ K. The pseudo-critical temperature T_{pc} is reached in the bulk of the fluid. The grid size of the first case is $192 \times 480 \times 512$, while that of the second case is $256 \times 768 \times 768$. $Re = 8000$ in both cases. In the following, we will investigate the conservation of the mass, momentum and enthalpy of the system.

2.5.1 Conservation of mass and energy

In section 2.2, methods were introduced that should be considered non-conservative: in particular, equations (2.7) and (2.11). It is important, however, that these methods do not violate the conservation laws for mass, momentum and enthalpy. In general (while excluding body forces), the conservation equations for a scalar ϕ or a vector \mathbf{v} can be

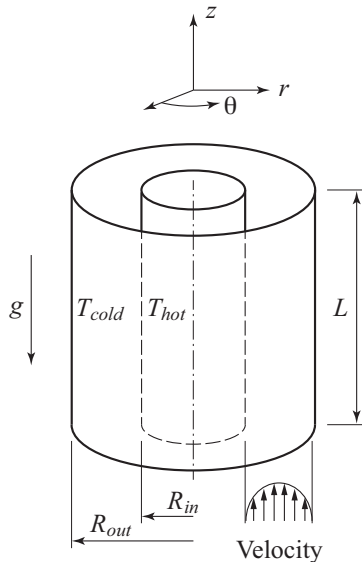


Figure 2.5: Annular configuration.

written in the following form :

$$\begin{aligned}\partial_t \phi + \nabla \cdot \mathbf{j} &= 0 \\ \partial_t \mathbf{v} + \nabla \cdot \mathbf{J} &= 0\end{aligned}\tag{2.18}$$

where,

$$\text{(mass)} \quad \phi = \rho : \quad \mathbf{j} = \rho \mathbf{u}\tag{2.19}$$

$$\text{(momentum)} \quad \mathbf{v} = \rho \mathbf{u} : \quad \mathbf{J} = \rho \mathbf{u} \mathbf{u} + p \mathbf{I} - 2\mu \mathbf{S}\tag{2.20}$$

$$\text{(enthalpy)} \quad \phi = \rho h : \quad \mathbf{j} = \rho \mathbf{u} h - k \nabla T\tag{2.21}$$

Equations (2.18) can be written in integral form as:

$$\begin{aligned}\frac{\partial}{\partial t} \iiint_V \phi dV + \oiint_a \mathbf{j} \cdot d\mathbf{a} &= 0 \\ \frac{\partial}{\partial t} \iiint_V \mathbf{v} dV + \oiint_a \mathbf{J} \cdot d\mathbf{a} &= 0\end{aligned}\tag{2.22}$$

Since convection is zero at the walls, and since the heat flux at the inner wall must balance that at the outer wall, equations (2.19) and (2.21) imply that in a (statically) fully developed flow $\iiint_V \rho dV$ and $\iiint_V \rho h dV$ must be constant. Furthermore, in such situations, the mean stream-wise pressure gradient should balance the mean shear stresses at the

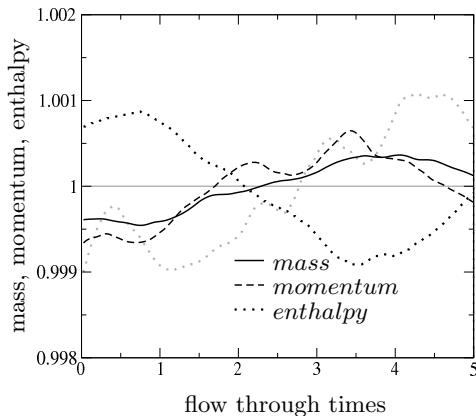


Figure 2.6: Variation of the total mass, momentum and enthalpy in the $s\text{CO}_2$ case and the reference case. Values are normalised using the respective averages. Results in grey indicate results from the constant properties case.

walls, so that $\iiint_V \rho u dV$ is constant as well. These implications were checked for the aforementioned simulation. The results are shown in figure (2.6(a)). It is clear that the total enthalpy variation of the case with simultaneously heated and cooled $s\text{CO}_2$ is very similar to that of the case with constant properties. The variation in the total enthalpy of the system is the result of a numerical mismatch between the the heat flux at the inner wall and that at the outer wall. The total mass variation shows an opposite trend to that of the total enthalpy. The total mass variation with time is therefore the result of the fact that the heat flux at the inner wall does not (instantaneously) balance that of the outer wall.

2.6 Summary

The numerical methods that are used to simulate heat transfer to a turbulent fluid at super-critical pressure have been presented; an 2nd order Adams-Bashford time integration scheme and a combination of compact finite difference and pseudo-spectral spatial discretisation methods are used. These methods have been validated against both numerical as well as experimental data of heated flows at sub-critical pressure with satisfactory results. Furthermore, preliminary tests were conducted to test the numerical methods with respect to a heated flow at super-critical pressure.

Bibliography

- Joong Hun Bae, Jung Yul Yoo, and Haecheon Choi. Direct numerical simulation of turbulent supercritical flows with heat transfer. *Physics of Fluids*, 17(10):105104, 2005.
- Joong Hun Bae, Jung Yul Yoo, and Donald M. McEligot. Direct numerical simulation of heated CO₂ flows at supercritical pressure in a vertical annulus at Re=8900. *Physics of Fluids*, 20(5):055108, 2008.
- B. J. Boersma. A 6th order staggered compact finite difference method for the incompressible Navier-Stokes and scalar transport equations. *Journal of Computational Physics*, 230(12):4940 – 4954, 2011.
- A. D. Carr, M. A. Connor, and H. O. Buhr. Velocity, temperature, and turbulence measurements in air for pipe flow with combined free and forced convection. *Journal of Heat Transfer*, 95 Ser C(4):445–452, 1973.
- S.Y. Chung, G.H. Rhee, and H.J. Sung. Direct numerical simulation of turbulent concentric annular pipe flow. Part 1: Flow field. *International Journal of Heat and Fluid flow*, 23:426–440, 2002.
- W.J. Feiereisen, W.C. Reynolds, and J.H. Ferziger. Numerical simulation of a compressible homogeneous, turbulent shear flow. Technical report, 1981. Report TF-13, Thermoscience Division, Department of Mechanical Engineering, Stanford University, Stanford.
- A. Fenghour, W. A. Wakeham, and V. Vesovic. The viscosity of carbon dioxide. *Journal of Physical and Chemical Reference Data*, 27:31–44, 1998.
- C. A. Kennedy and A. Gruber. Reduced aliasing formulations of the convective terms within the navier-stokes equations for a compressible fluid. *Journal of Computational Physics*, 227(3):1676–1700, 2008.
- O. Kunz, W. Wagner R. Klimeck, and M. Jaeschke. The GERG-2004 wide-range equation of state for natural gases and other mixtures. Technical report, 2007. GERG Technical Monograph 15, Fortschritt-Berichte VDI, VDI-Verlag, Düsseldorf.
- E.W. Lemmon, M.L. Huber, and M.O. McLinden. NIST standard reference database 23: Reference fluid thermodynamic and transport properties-REFPROP. Version 9.1, National Institute of Standards and Technology, Standard Reference Data Program, Gaithersburg, 2013.

- P.D. McMurtry, W.-H. Jou, J. Riley, and R.W. Metcalfe. Direct numerical simulations of a reacting mixing layer with chemical heat release. *AIAA Journal*, 24(6):962–970, 1986.
- H. N. Najm, P. S. Wyckoff, and O. M. Knio. A semi-implicit numerical scheme for reacting flow: I. stiff chemistry. *Journal of Computational Physics*, 143(2):381 – 402, 1998.
- H. Nemati, A. Patel, B.J. Boersma, and R. Pecnik. Mean statistics of a heated turbulent pipe flow at supercritical pressure. *International Journal of Heat and Mass Transfer*, 83:741 – 752, 2015.
- F. Nicoud. Conservative high-order finite-difference schemes for low-mach number flows. *Journal of Computational Physics*, 158:71–97, 2000.
- K. Nishikawa and I. Tanaka. Correlation lengths and density fluctuations in supercritical states of carbon dioxide. *Chemical Physics Letters*, 244:149–152, 1995.
- M. Ould-Rouiss, L. Redjem-Saad, G. Lauriat, and A. Mazouz. Effect of prandtl number on the turbulent thermal field in annular pipe flow. *International Communications in Heat and Mass Transfer*, 37:958–963, 2010.
- A. Patel, J.W.R. Peeters, B.J. Boersma, and R. Pecnik. Semi-local scaling and turbulence modulation in variable property turbulent channel flows. *Physics of Fluids*, 27(9): 095101, 2015.
- V. Vesovic, W. Wakeham, G. Olchowy, J. Sengers, J. Watson, and J. Millat. The transport properties of carbon dioxide. *Journal of Physical and Chemical Reference Data*, 19:763–808, 1990.
- B. Zappoli, D. Beysens, and Y. Garrabos. *Heat transfers and related effects in supercritical fluids*. Springer, 2015.

CHAPTER 3

TURBULENCE ATTENUATION

The contents of this chapter were published before under the title: "Turbulence attenuation in simultaneously heated and cooled annular flows at supercritical pressure" in the Journal of Fluid Mechanics, volume 799, pages 505–540, 2016.

3.1 Introduction

In order to understand how the thermophysical property variations of a fluid at supercritical pressure affect heat transfer, it is important to understand how the flow, and turbulence in particular, are affected by thermophysical property variations. This is not fully understood, yet. However, such knowledge will help in the design of better heat transfer models, such as Nusselt number relations and turbulence models.

To investigate the effect of thermophysical property variations on turbulent flow characteristics, Bae et al. [2005, 2008] simulated heat transfer to supercritical carbon dioxide (sCO₂) at 8 MPa in a pipe and annular geometry, respectively. Bae et al. [2005] reported significantly decreased vortical motions near the heated surface. This is an important observation as stream-wise vortices are an integral part of the self regenerating process of near wall turbulence (see for instance Waleffe [1997] and Hamilton et al. [1995]). Bae et al. [2008] found that velocity profiles and shear stress profiles are significantly affected by acceleration and the combined effect of buoyancy and a negative stream-wise pressure gradient; such findings are qualitatively in line with the experiments by Kurganov and Kaptil'ny [1992].

More recently, Zonta et al. [2012] and Lee et al. [2013] showed the effect of variable dynamic viscosity, representative of a fluid at sub-critical pressure, on a channel flow and a boundary layer flow. They found that the variation in viscosity causes the turbulence intensities to diminish. More specifically, Zonta et al. [2012] report that the streak characteristics are altered due to the variation in viscosity. Strong variations of dynamic

viscosity and thermal expansion coefficient were shown to have a large impact on momentum and heat transfer in stably-stratified channel flows (Zonta et al. [2012] and Zonta [2013]). High viscosity regions dampen the turbulent intensities, whereas low viscosity regions enhance the intensities. Unstably density stratification in a horizontal channel flow configuration was found to significantly increase momentum and heat transfer by Zonta and Soldati [2014]. These studies show that the non-linear thermophysical property relations for the thermophysical properties (non-Oberbeck-Boussinesq conditions) may have a profound effect on flow statistics and flow structures. It is also interesting to note here that Patel et al. [2015] found that the stability of streaks is significantly affected by mean density and viscosity stratification. These findings are important as streaks not only contribute greatly to the turbulent shear stress (Willmarth and Lu [1972]), but are also an integral part of the self-regenerating process of near wall turbulence.

In this chapter, we will investigate how the variable thermophysical properties of a heated (or cooled) fluid at supercritical pressure affect turbulent motions in a qualitative as well as a quantitative manner. Firstly, we are interested in what the influence of a mean density and dynamic viscosity variation is on the flow field. Secondly, we would like to investigate how instantaneous density- and dynamic viscosity fluctuations affect the turbulent motions, and more specifically, turbulent structures such as the near wall streaks and stream-wise vortices, which are important to the self-regeneration of turbulence in the near wall region. Lastly, we want to investigate the role of the variable Prandtl number with respect to the generation of turbulent structures, as it determines the magnitude of the thermal fluctuations and therefore the thermophysical property fluctuations. To this end, results from Direct Numerical Simulations (DNS) of simultaneously heated and cooled turbulent supercritical fluids flowing upwards in an annular geometry at a Reynolds number of 8000 will be shown. A schematic of the investigated geometry is shown in figure 3.1. The temperature crosses the pseudo-critical point within the flow field. The inner wall of the annular geometry is kept at a high temperature, while the outer wall is kept at a low temperature. In this manner, a statistically fully developed temperature and flow profile can be obtained. This allows us to focus on local variable thermophysical properties effects on turbulence, because effects such as a growing thermal boundary layer and mean stream-wise flow acceleration will not be present.

In the next section, five numerical cases that are suitable to investigate the effect of variable thermophysical properties on turbulence are described. Subsequently, the effect of the mean density and viscosity profiles of supercritical carbon dioxide (sCO_2) on mean flow statistics will be discussed first. Thereafter, the influence of the instantaneous density- and dynamic viscosity variations on turbulent structures will be investigated. Finally, a summary of the most important conclusions will be presented.

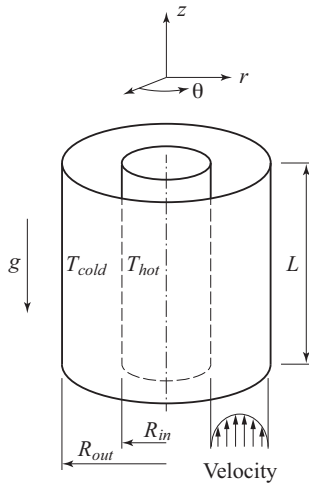


Figure 3.1: The annular geometry of the simulations. The inner and outer wall radii (R_{in} & R_{out}), the length L and the inner and outer wall temperatures (T_{hot} & T_{cold}) are shown.

3.2 Cases

In total, five cases have been simulated. The simulation parameters are summarised in table 3.1. In case I, all thermophysical properties are constant, which is representative of a turbulent flow at sub-critical pressure at low heating (or cooling) rates. In cases II and III, the thermophysical properties correspond to those of CO_2 at 8 MPa. Upward mixed convection (the combination of both forced- and free convection) effects are considered only in case III; all other cases are forced convection. Cases IV and V are cases with artificial thermophysical property behaviour, which are used to isolate either ρ - or μ specific characteristics or effects. In these cases, all properties are constant, except for the density (case IV) or the dynamic viscosity and thermal conductivity (case V). The molecular Prandtl number $Pr = \mu c_p / k$, is equal to 2.85 in the reference case (I) and the variable density (IV) and viscosity (V) cases, which is equal to the reference Prandtl number Pr_h in the sCO_2 cases. In case V, the thermal conductivity varies in the same way as the dynamic viscosity in order to keep the molecular Prandtl number constant. By doing so, the thermal length scales are of similar magnitude for cases I, IV and V. It can therefore be expected that the magnitude of thermophysical property variations is similar in cases IV and V. The molecular Prandtl number only varies in the sCO_2 cases. The inner wall of the annulus ($r = R_{in} = 0.5$) is kept at a constant temperature of 323 K, while the outer wall ($r = R_{out} = 1.0$) is kept at a lower temperature of 303 K. By simultaneously heating and cooling the fluid, a statistically fully developed turbulent

| Case | Properties | $Re_{\tau,in}$ | $Re_{\tau,out}$ | $Pr = \mu c_p/k$ |
|------|--------------------------|----------------|-----------------|------------------|
| I | constant | 276 | 264 | $Pr = 2.85$ |
| II | CO ₂ at 8 MPa | 275 | 220 | $Pr = 1.6 - 14$ |
| III | CO ₂ at 8 MPa | 310 | 221 | $Pr = 1.6 - 14$ |
| IV | variable ρ | 185 | 345 | $Pr = 2.85$ |
| V | variable μ | 375 | 180 | $Pr = 2.85$ |

| Case | flow condition | Fr^{-1} | $N_r \times N_\theta \times N_z$ |
|------|----------------|-----------|----------------------------------|
| I | forced | 0 | $192 \times 480 \times 512$ |
| II | forced | 0 | $256 \times 768 \times 768$ |
| III | mixed | -0.1 | $256 \times 768 \times 768$ |
| IV | forced | 0 | $192 \times 480 \times 512$ |
| V | forced | 0 | $192 \times 480 \times 512$ |

Table 3.1: Summary of direct numerical simulations considered at $Re_b = 8000$. The reference Prandtl number Pr_h equals 2.85 in all cases. $Re_{\tau,in} = (R_{out} - R_{in})/\delta_{\nu,in}$.

| Case | $(\Delta r)_{in}^+$ | $(r\Delta\theta)_{in}^+$ | $(\Delta z)_{in}^+$ | $(\Delta r)_{out}^+$ | $(r\Delta\theta)_{out}^+$ | $(\Delta z)_{out}^+$ |
|------|---------------------|--------------------------|---------------------|----------------------|---------------------------|----------------------|
| I | 0.55–2.24 | 3.60 | 8.60 | 0.53–2.10 | 7.22 | 8.19 |
| II | 0.42–1.65 | 2.25 | 5.71 | 0.30–1.32 | 3.60 | 4.50 |
| III | 0.50–1.97 | 2.51 | 6.40 | 0.33–1.33 | 3.62 | 4.62 |
| IV | 0.36–1.45 | 2.37 | 3.03 | 0.69–2.75 | 8.90 | 11.3 |
| V | 0.75–3.00 | 4.91 | 11.7 | 0.34–1.35 | 4.40 | 5.27 |

Table 3.2: Summary of the mesh size w.r.t. the viscous length scale $\delta_{\nu,in} = \mu_{w,in}/(\rho_{w,in}u_{\tau,in})$ near the inner wall and the outer wall $\delta_{\nu,out}$.

flow can be realised. The bulk Reynolds number is kept constant at 8000. The friction Reynolds numbers at the inner wall and the outer wall, $Re_{\tau,in}$ and $Re_{\tau,out}$ are listed in table 3.1. The stream-wise length L_z of the annular geometry equals $8D_h$. Note that in all cases, with the exception of case III, the value of $w_b^o D_h^o$ is fixed as $(\mu_{pc}^o/\rho_{pc}^o)Re_b$ m²/s. For case III, $Fr^{-1} = 0.1$, which results in $w_b^o = 8.2$ cm/s and $D_h^o = 6.9$ mm.

The grid-spacings, with respect to both the viscous length scale δ_ν and the Batchelor scale $\eta_B = \eta_K/\sqrt{Pr}$ (the smallest spatial scale of the temperature field), are summarised in table 3.2 and table 3.3. The grid-spacings are comparable to those of both Zonta et al. [2012] and Lee et al. [2013]. For reasons of readability, further details regarding the mesh, such as wall normal cell width and power spectra of the enthalpy fluctuations, are shown in appendix A.3.1.

| Case | $\Delta r/\eta_B$ | $r\Delta\theta/\eta_B$ | $\Delta z/\eta_B$ |
|------|-------------------|------------------------|-------------------|
| I | 0.57–1.20 | 1.12–7.00 | 4.00–8.71 |
| II | 0.24–1.75 | 1.20–7.10 | 1.69–9.70 |
| III | 0.22–1.75 | 0.60–6.60 | 1.48–8.40 |
| IV | 0.31–1.38 | 2.00–10.6 | 4.67–12.5 |
| V | 0.20–1.12 | 2.20–5.40 | 3.80–12.7 |

Table 3.3: Summary of the mesh size w.r.t. the Batchelor length scale $\eta_B = \eta_K/\sqrt{Pr}$, where η_K represents the Kolmogorov length scale. The listed values correspond to the whole computational domain.

3.3 Mean statistics

Our aim in this section is to investigate the effect of variable ρ and μ of a fluid at supercritical pressure on the turbulent flow field. When discussing the results, the emphasis will therefore be on the sCO₂ cases (cases II and III) in comparison with results of the reference case (case I). We will first discuss the property variations both qualitatively and quantitatively. Thereafter, we will investigate the effect of the mean property variation on the velocity statistics, such as first and second order moments, as well as the production of the turbulent kinetic energy.

3.3.1 Mean thermophysical property statistics

In all simulated cases, the inner wall was kept at a higher temperature than the outer wall, which means that there is a mean radial enthalpy gradient inside the flow. As such, the fluid is of low density and low dynamic viscosity near the inner wall and vice versa near the outer wall, in the sCO₂ cases (II and III). Figure 3.2(a) shows instantaneous values of the Prandtl number, the density and the dynamic viscosity in the forced convection sCO₂ case (II). Near the walls, low density/low dynamic viscosity fluid is mixed in with high density/high dynamic viscosity fluid due to the turbulent motions of the fluid. The Prandtl number is largest at the pseudo-critical temperature. Temperatures close to the pseudo-critical point can be found near the inner wall.

Because there is a mean radial enthalpy profile, there are also mean density and dynamic viscosity profiles. The mean density and dynamic viscosity profiles as well as the mean Prandtl number profiles of the forced convection sCO₂ case (II) are shown in figures 4.3(a) and 4.3(b). The mean variation of the thermophysical properties is most significant close to the inner wall ($y^+ < 20$), where the flow is heated, and near the outer wall, where the flow is cooled. The mean property variation further away from the wall ($y^+ > 50$) is very small, however. The mean variation of the properties in the mixed

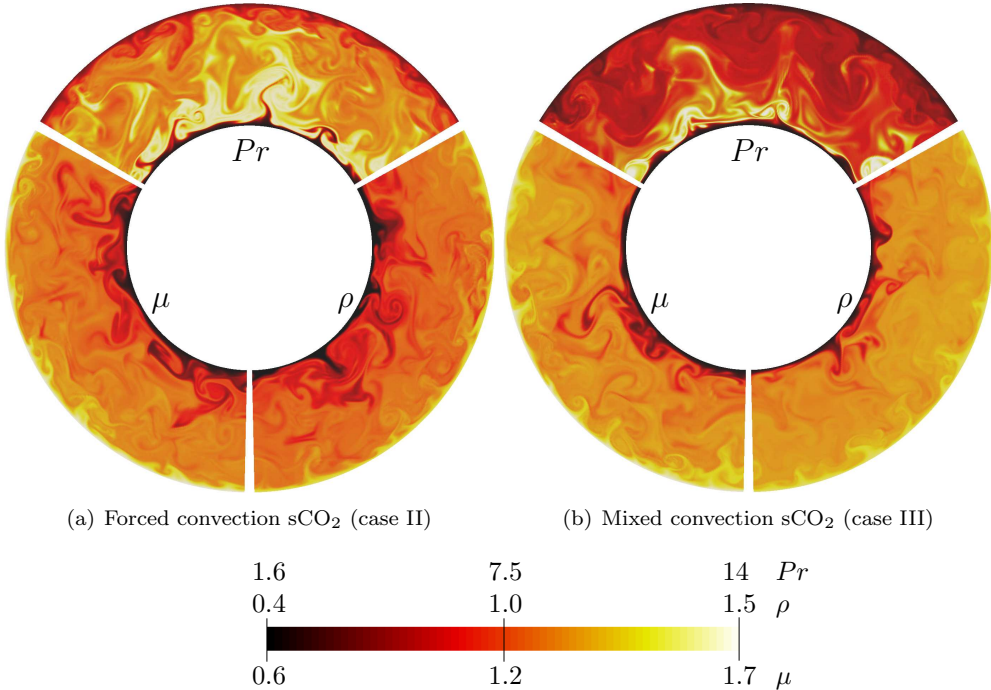


Figure 3.2: Instantaneous cross-sectional visualization of thermophysical properties for the supercritical fluid cases (II and III). The upper third shows the Prandtl number, the lower left part the dynamic viscosity and lower right the density.

convection sCO₂ case (III) is very similar to these results. Note that in the reference case (I), all thermophysical properties are equal to unity.

Figures 3.3(c) and 3.3(d) show the root mean square profiles of the property fluctuations. The strongest fluctuations occur close to the walls, especially for $y^+ < 20$. The fluctuations are much stronger near the hot inner wall of the annulus than near the outer wall of the annulus. This observation can be attributed to the fact that the pseudo-critical point lies close to the inner wall. The average Prandtl number is much higher in the forced convection sCO₂ case (II) than it is in the variable density (IV) and dynamic viscosity (V) cases for approximately $y^+ > 5$. Large values of the molecular Prandtl number cause large enthalpy fluctuations (see for instance Kawamura et al. [1998]) and therefore locally steep enthalpy gradients, which in turn lead to locally steep thermophysical property gradients. This partially explains why the thermophysical property fluctuation intensities are much larger in the forced convection sCO₂ case (II) than they are in the variable density (IV) and dynamic viscosity (V) cases. Another contributing factor is the fact that the turbulence intensities are different in the three aforementioned

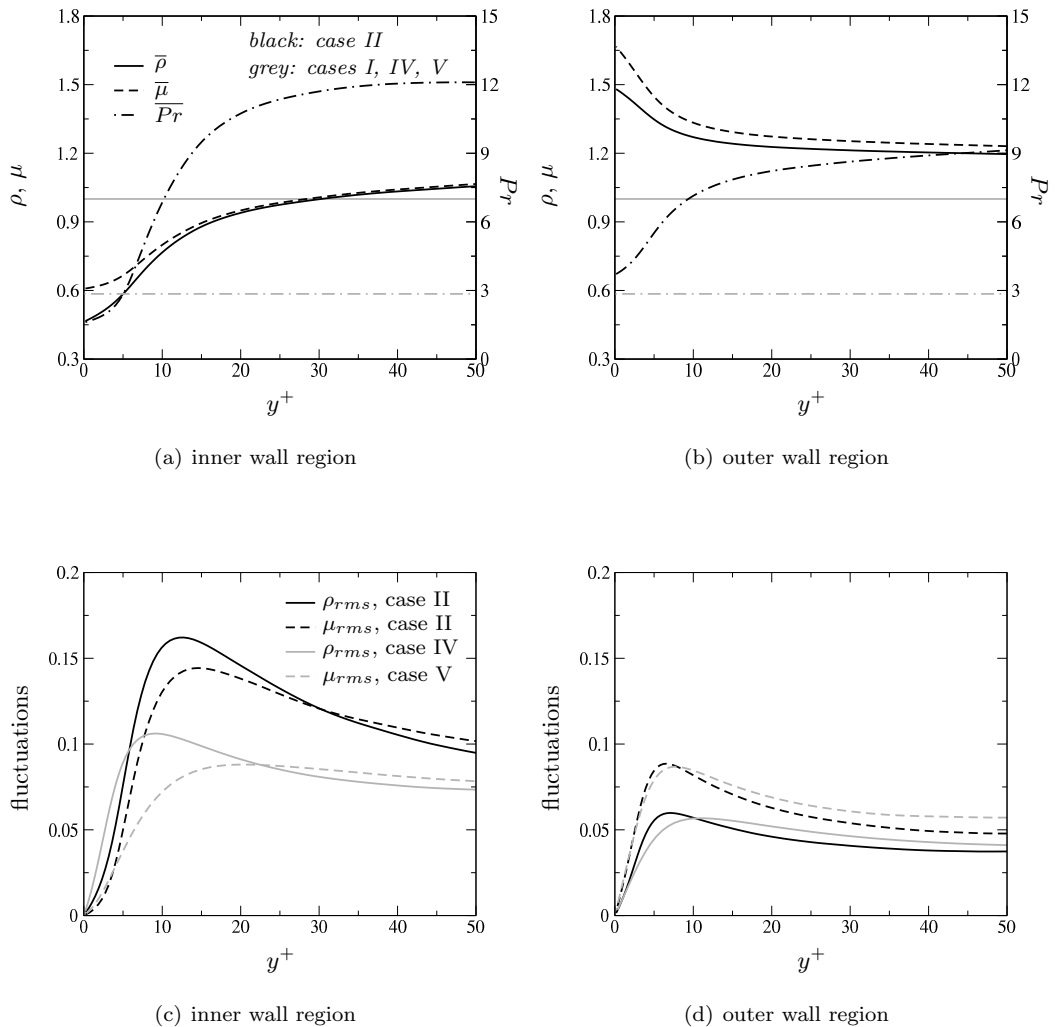


Figure 3.3: Radial profiles of mean properties and property fluctuations in the forced convection sCO₂ case (II). Black lines indicate forced convection sCO₂ results. Grey lines indicate results from the variable density (IV) and dynamic viscosity (V) cases. The constant grey line in the top figures represents the constant density in cases I and V or the constant viscosity in cases I and IV.

cases (II, IV and V), which will be shown later. The largest normalised thermophysical property fluctuation intensity is 22% for the density ($= \rho_{rms}/\bar{\rho}$) and 18% ($= \mu_{rms}/\bar{\mu}$) for the dynamic viscosity in the forced convection sCO₂ case (II). For the variable viscosity case (V) the largest value of $\mu_{rms}/\bar{\mu} = 14\%$, while for the variable density case (IV) the

largest value of $\rho_{rms}/\bar{\rho} = 10\%$. The thermophysical property variations of the mixed convection sCO₂ case (III) are very similar as that of the forced convection sCO₂ case (II) and are not shown here.

3.3.2 Velocity profiles

In the previous section we described the variation of the thermophysical properties ρ and μ in terms of the mean radial profiles and the *rms* values of the thermophysical property fluctuations. In this section as well as the subsequent sections, we will describe how the mean radial thermophysical property variations modulate the turbulent flow using classical mean flow quantities, such as mean velocity and turbulent stress profiles.

Figures 3.4(a) and 3.4(b) show the mean radial profiles of the stream-wise velocity $\bar{w}(r)$, where $\bar{(\)}$ denotes a time averaged mean quantity. In all variable property cases, the maximum of $\bar{w}(r)$ shifts towards the hot wall and increases in magnitude, when compared with the velocity profile of the reference case (I). This is a consequence of both the lower mean density and dynamic viscosity values near the hot wall (vice versa near the outer wall), since both the variable density (IV) and the variable dynamic viscosity (V) cases show this behaviour. The combination of a radial mean density profile and a non-zero Froude number (and thus a non-zero gravitational force) in the mixed convection case (III) causes the maximum of $\bar{w}(r)$ to move even closer to the hot inner wall. The mean strain rate $\partial_r \bar{w}(r)$ is increased in the immediate vicinity of the hot wall and decreased near the cold wall in all cases, except for the variable density case (IV). In the subsequent section, an in-depth analysis of the (turbulent) shear stress is presented, which is important in understanding the ‘shifted’ velocity profiles that were presented here.

3.3.3 Turbulent shear stress

To investigate the shifts in velocity profiles, the shear stress profiles can be analyzed. The total shear stress τ_{rz}^{tot} may be written as the sum of the viscous stresses, a fluctuating viscosity stress term and the turbulent stress:

$$\bar{\tau}_{rz}^{tot} = Re^{-1} \bar{\mu} \partial_r \bar{w} + Re^{-1} \overline{\mu' S'_{rw}} - \overline{\bar{\rho} u'' w''} \quad (3.1)$$

Note that in this equation, a $(\)'$ represents a fluctuation with respect to a Reynolds average and $(\)''$ stands for a fluctuating quantity with respect to a density weighted mean (or Favre average) $\tilde{(\)}$. From equation (3.1), it is clear that the viscous shear stress scales with $\bar{\mu}$, while the turbulent shear stress scales with $\bar{\rho}$. In all cases with variable dynamic viscosity (II, III and V), the fluctuating dynamic viscosity stress term was observed to be negligible, when compared to the other shear stresses, which is in line

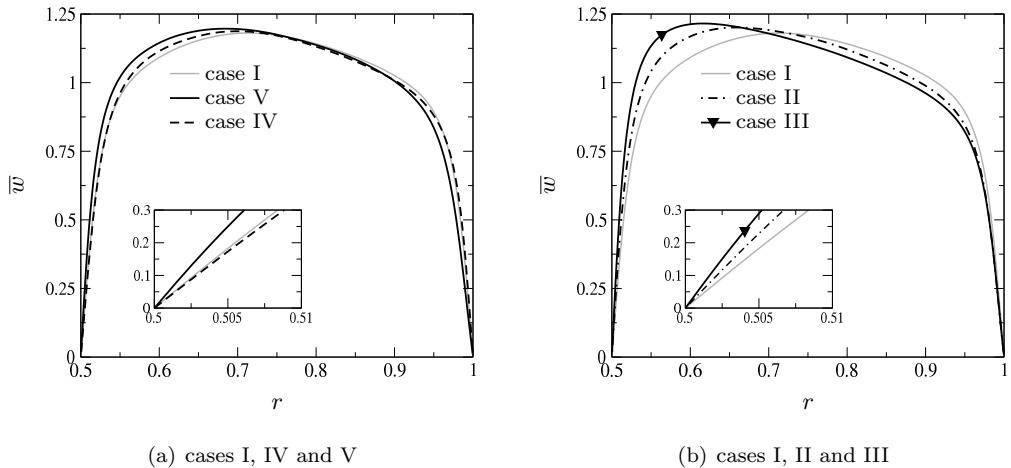


Figure 3.4: Mean velocity profiles of the variable density and viscosity cases (IV and V respectively, on the left) and the forced and mixed convection sCO₂ cases (II and III respectively, on the right). The grey lines represent results from the reference case (I).

with Lee et al. [2013] and Zonta et al. [2012] and it will therefore not be discussed. By integrating the time averaged stream-wise component of the momentum equation in the radial direction from R_{in} to r , an analytical expression for the total shear stress may be obtained, assuming that the mean flow is steady state and thus that the mean stream-wise pressure gradient is balanced by the shear stress at the inner and outer wall and the gravitational force acting on the flow (Petukhov and Polyakov [1988]):

$$\bar{\tau}_{rz}^{tot}(r) = R_{in}\tau_{in} + (r^2 - R_{in}^2)\partial_z\bar{p}/2 + Fr^{-1} \int_{R_{in}}^r \bar{\rho}(r)rdr \quad (3.2)$$

where τ_{in} is the shear stress at the inner wall. The mean stream-wise pressure gradient $\partial_z\bar{p}$ may be written as:

$$\partial_z\bar{p}/2 = \frac{R_{out}\tau_{out} - R_{in}\tau_{in}}{R_{out}^2 - R_{in}^2} + \frac{Fr^{-1}}{R_{out}^2 - R_{in}^2} \int_{R_{in}}^{R_{out}} \bar{\rho}(r)rdr \quad (3.3)$$

Equations (3.2) and (3.3) show that the total shear stress profile is dependent on the mean dynamic viscosity profile, because $\tau_{in} = \bar{\mu}\partial_r\bar{w}|_{r=R_{in}}$ and $\tau_{out} = \bar{\mu}\partial_r\bar{w}|_{r=R_{out}}$, as well as the effect of a mean radial density stratification in combination with the gravitational force.

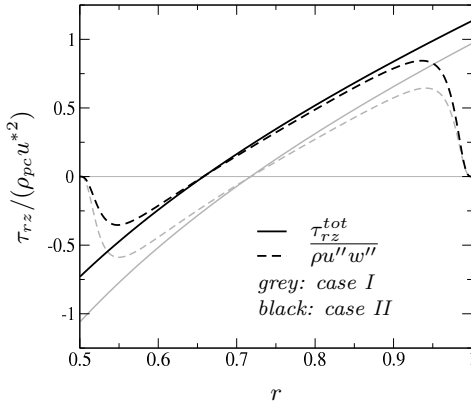
The buoyancy neutral stream-wise pressure gradient (which can be obtained by setting $Fr^{-1} = 0$ in equation (3.3)) can be used to define a velocity scale that is convenient for

analysing shear stress profiles in annular geometries (Boersma and Breugem [2011]):

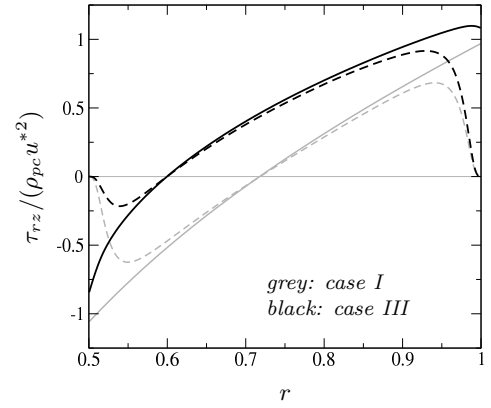
$$u_* = \left(\frac{1}{2\rho_{pc}D_h} \frac{R_{out}\tau_{out} - R_{in}\tau_{in}}{R_{out}^2 - R_{in}^2} \right)^{1/2} \quad (3.4)$$

This velocity scale can be thought of as a weighted average of the friction velocities at the inner wall and the outer wall of the annulus. Figures 3.5(a) to 3.5(d) show the total shear stress, as well as the turbulent shear stress of all four variable property cases.

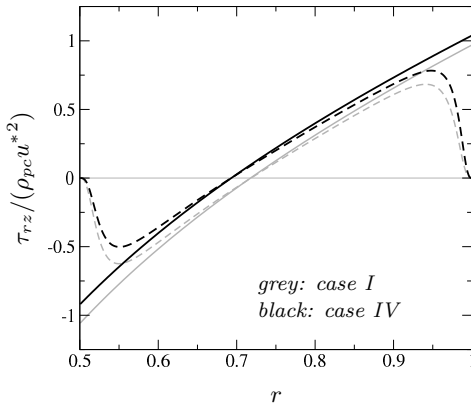
In all variable property cases, except for the mixed convection case (III), the total shear stress profiles are shifted, when compared with the shear stress in the reference case (I), which is in line with the mean stream-wise velocity results. In all cases, the magnitude of the wall shear stress is smaller at the inner wall, but is larger at the outer wall, when comparing these results with the reference case (I). In the variable viscosity case (V, see figure 3.5(d)), the wall shear stress magnitude is smaller due to the lower mean dynamic viscosity at the inner wall, even though the magnitude of the mean strain rate is larger (see inset in figure 3.4(a)), when compared with the reference case. The reverse is true for the outer wall. The variable density case (IV, see figure 3.5(c)) can be explained as follows. As the variable density has no direct effect on the viscous stresses, the changes in the total shear stress profile must be explained by analysing the turbulent shear stress; as the turbulent shear stress magnitude is smaller near the inner wall region (when compared to the reference case), less high momentum fluid is transported from the bulk towards the inner wall, resulting in a smaller mean strain rate magnitude (see the inset of figure 3.4(a)) and thus a smaller wall shear stress at the inner wall. The reverse of this argument holds for the outer wall, i.e. due to the fact that the turbulent shear stress is larger in the variable density case (IV) when compared to that of the reference case (I), more high speed momentum is transported towards the outer wall, which thereby increases the magnitude of the outer wall mean strain rate and thus the magnitude of the shear stress at the outer wall. The effects of the variable viscosity and density on the shear stress profiles combine in the forced convection case (II, see figure 3.5(a)), which simply results in a larger shift of the total shear stress profile, when compared with the variable density (IV) and dynamic viscosity (V) cases. It is interesting to note here that the effect of the variable viscosity on mean strain rate magnitude in this case are slightly stronger than that of the density effect (see inset in figure 3.4(b)). In the mixed convection sCO₂ case (III, see figure 3.5(b)), the interplay between the shear stress at the walls, the mean negative stream-wise pressure gradient and the gravitational force does not shift, but rather distort the total shear stress profile. In all cases, it is clearly visible that the turbulent shear stress changes in accordance with the total shear stress profile, as the magnitude of the turbulent shear stress is bounded by that of the total shear stress. These results show that the mean profiles of both the dynamic viscosity and the density change the magnitude and shape of the turbulent shear stress. As a



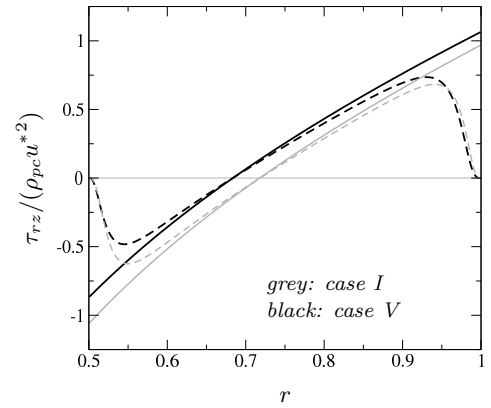
(a) case II vs. case I



(b) case III vs. case I



(c) case IV vs. case I



(d) case V vs. case I

Figure 3.5: Total and turbulent stress in the forced and mixed convection sCO₂ cases (cases II and III, upper row) and the variable density and variable viscosity cases (cases IV and V, lower row). Grey lines indicate results from the reference case (I). Continuous lines represent the total shear stress, while dashed lines denote the turbulent shear stress. The turbulent shear stress is normalised in the same manner as the total shear stress.

result, the velocity magnitude increases in a region with less shear stress and decreases in a region with higher shear stress.

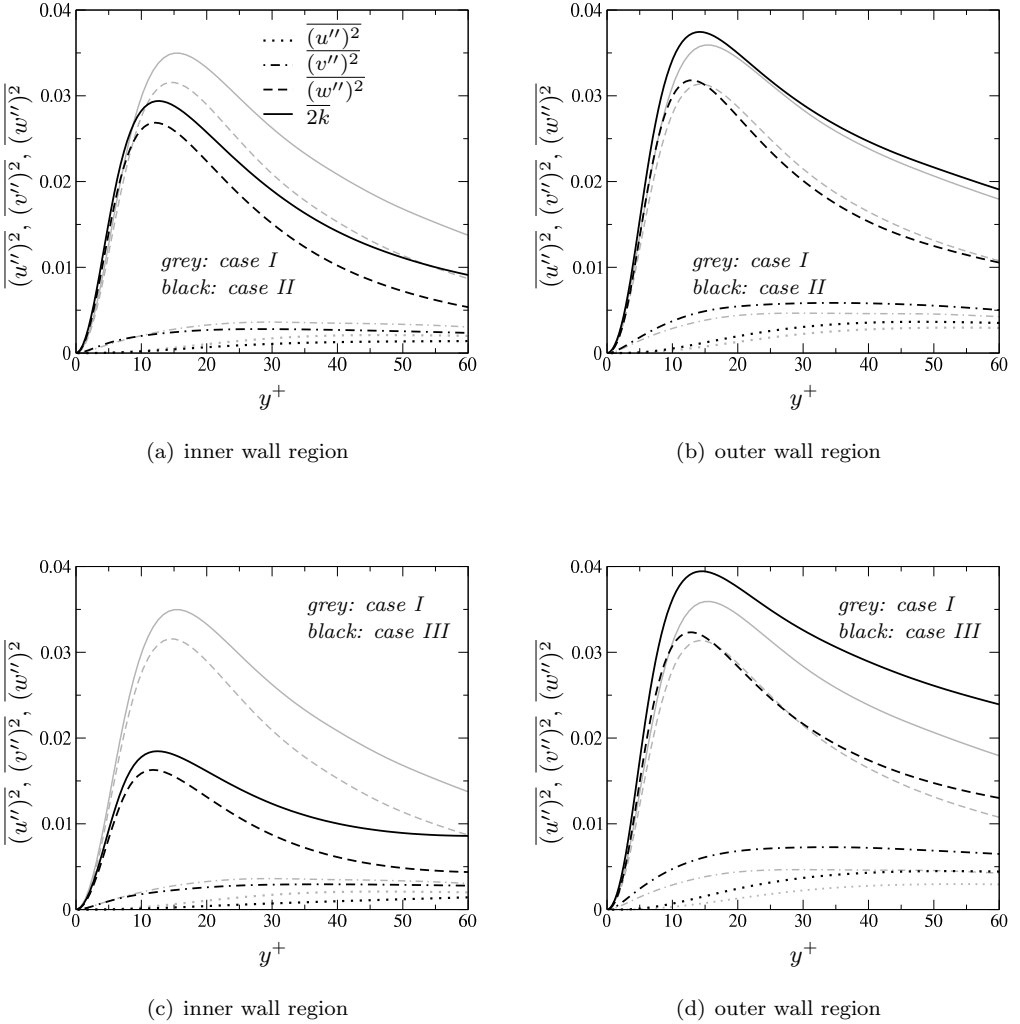


Figure 3.6: Comparison of the turbulent intensities between the reference case (I) and the sCO₂ forced (II) and mixed (III) convection cases.

3.3.4 Turbulence intensities

The previous section showed that the turbulent shear stress is appreciably affected by the mean dynamic viscosity and density stratification. Here, we will investigate the turbulent motions further. The turbulent intensities $\overline{u''^2}$, $\overline{v''^2}$, $\overline{w''^2}$ as well as the turbulent kinetic energy $k = 1/2(\overline{\mathbf{u}'' \cdot \mathbf{u}''})$ are shown in figure 3.6. Near the inner wall, for $y^+ > 10$, the magnitude of the stream-wise fluctuations w''^2 in the forced convection sCO₂ case (II,

see figure 3.6(a)) shows a large decrease when compared to the reference case (I). Closer to the wall, i.e. $y^+ < 10$, there is almost no change. Similar behaviour is observed for the other fluctuations (u''^2 and v''^2). The decrease in the magnitude of the turbulent intensities is even more apparent near the inner wall in the mixed convection case (III, see figure 3.6(c)). While in absolute value the decrease is most apparent in the stream-wise motions, it should be noted that relatively, the other motions are substantially affected as well. Consequently, the specific turbulent kinetic energy, which is primarily determined by the stream-wise velocity fluctuations, has decreased as well. The outer wall regions in both cases (II and III, see figures 3.6(b) and 3.6(d)) show the exact opposite of what happens near the inner wall. Here, the turbulent intensities and thus the kinetic energy have increased. Especially the wall normal and circumferential motions have increased in magnitude, while the stream-wise velocities have only increased slightly in magnitude.

The fact that all the turbulent intensities and the turbulent kinetic energy are appreciably affected in the same manner by sCO₂ thermophysical properties suggests that the turbulent flow can relaminarise near a heated surface, or become more turbulent near a cooled wall, in both forced convection and buoyancy opposed mixed convection conditions. The decrease (or increase) in intensities may however come from different effects, such as changes in local Reynolds number, production of turbulent kinetic energy, or changes to turbulent structures. This will be discussed in the subsequent sections.

3.3.5 Local Reynolds number effect

As a result of the mean density and dynamic viscosity profiles, the ratio of inertial stress magnitude to the viscous stress magnitude have changed. A Reynolds number can be defined that is representative of this ratio locally (Zonta et al. [2012]). With local, we refer to either the heated side of the flow or the cooled side. We define the following local mean densities:

$$\rho_{hot} = \frac{2}{R_z^2 - R_{in}^2} \int_{R_{in}}^{R_z} \bar{\rho}(r) r dr \quad \text{and} \quad \rho_{cold} = \frac{2}{R_{out}^2 - R_z^2} \int_{R_z}^{R_{out}} \bar{\rho}(r) r dr, \quad (3.5)$$

where R_z is the radial location where the total mean shear stress is zero. The local mean viscosities and velocities are obtained by replacing the density with the dynamic viscosity or stream-wise velocity, respectively in equation (3.5). The local mean density and dynamic viscosity can be used to define a local Reynolds number, or ratio of convective stress to viscous stress:

$$Re_{hot} = \frac{\rho_{hot} w_{hot} D_{hot}}{\mu_{hot}} \quad \text{and} \quad Re_{cold} = \frac{\rho_{cold} w_{cold} D_{cold}}{\mu_{cold}}, \quad (3.6)$$

where $D_{hot} = 2(R_z - R_{in})$ and $D_{cold} = 2(R_{out} - R_z)$. The local Reynolds numbers are shown for the different cases in table 3.4. In all variable thermophysical property

| Case | description | Re_{hot} | Re_{cold} | $\max((\tau - \tau^{ref})/\tau^{ref})$ |
|------|-------------------------------|-------------|-------------|--|
| I | reference | 3600 (0%) | 4400 (0%) | 0% |
| II | forced conv. sCO ₂ | 2802 (-22%) | 5055 (+15%) | -43%(hot), +23%(cold) |
| III | mixed conv. sCO ₂ | 1860 (-48%) | 5911 (+34%) | -65%(hot), +28%(cold) |
| IV | variable density | 3046 (-15%) | 5700 (+30%) | |
| V | variable viscosity | 3043 (-15%) | 5900 (+34%) | |

Table 3.4: Local Reynolds numbers for the simulated cases. τ in the last column denotes for the turbulent shear stress $\widetilde{\bar{\rho}u''w''}$.

cases, the local Reynolds number near the hot wall is decreased, while the Reynolds numbers near the cold wall are increased compared to the constant property reference case (I). If we compare the turbulent shear stress of the forced convection case (II) to that of the reference case (I), there is a maximum decrease of 43% near the hot wall. The change in the local Reynolds number however, shows a decrease of 22%. For the outer wall, the increase in turbulent shear stress is matched somewhat better by the increase in local Reynolds number. The mixed convection case (III) shows a similar trend. These results show that the changes in ratio of the inertial stress to the viscous stress are not sufficient in order to fully explain turbulence attenuation. This suggests that thermophysical property variations have an effect on turbulence as well.

3.3.6 Production of turbulent kinetic energy

The shift in turbulent shear stresses and the increase of magnitude of the the strain rate near the inner wall (and decrease near the outer wall) that were described earlier for the sCO₂ cases lead to changes in the production of turbulent kinetic energy, which may be written as $\mathcal{P}_k = -\bar{\rho}(\widetilde{u''w''})\partial_r\tilde{w}$. Figures 3.7(a) and 3.7(b) show P_k near the inner and outer wall regions, respectively. From these results, it is clear that, while the mean strain rate $\partial_r\tilde{w}$ may increase locally due to the low dynamic viscosity very close to the hot inner wall (and decrease very close to the cold outer wall due to high dynamic viscosity), the decrease in the magnitude of the turbulent shear stress is in fact of higher importance to the production of turbulent kinetic energy, since the production is smaller in the forced convection cases (II and III) than it is in the reference case (I).

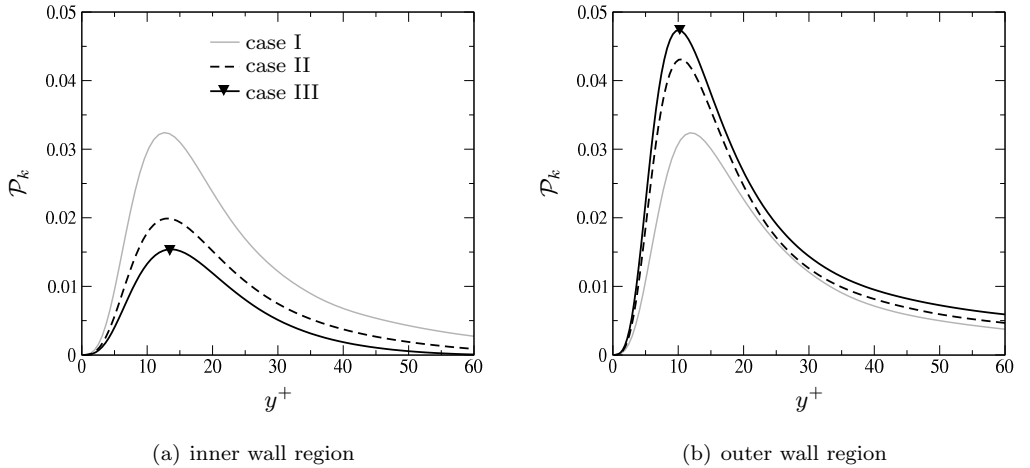


Figure 3.7: Production of turbulent kinetic energy in the reference case (I), forced sCO₂ (II) and mixed sCO₂ (III) convection cases.

3.4 Structures

While the previous section showed that the turbulent motions are affected by the mean dynamic viscosity and density stratification, it did not show whether the variable thermophysical properties fluctuations can influence the turbulent motions of the fluid. In this section, we will investigate the effect of instantaneous property fluctuations on the turbulent motions of the fluid. To that end, we will look at near wall streaks, as well as stream-wise vortices and how they are affected by the thermophysical property fluctuations.

It has been shown that near wall turbulence may be regarded as a self-regenerating process, consisting of the formation of stream-wise vortices and near wall streaks as well as their instabilities (Jimenez and Pinelli [1999], Schoppa and Hussain [2002], Waleffe [1997]). A flow may relaminarise if this self regenerating process is disrupted (Jimenez and Pinelli [1999], Kim [2011]). We will investigate here how near wall streaks, which are largely responsible for $\overline{w'^2}$, and stream-wise vortices, which contribute to $\overline{u'^2}$ and $\overline{v'^2}$, are affected by the fluctuations in thermophysical properties.

In the simulations with variable density, the momentum $\rho \mathbf{u}$ is a conserved quantity. Furthermore, the density is continuous (as opposed to multiphase liquid flows, in which the density is discrete, for example). Therefore, to investigate structures that are relevant in the self regenerating process, we chose to include the density in the mathematical

description of a structure. To analyze streaks, we will look at $(\rho w)' < 0$, which for instance was also done by Duan et al. [2011]. Similarly, we will use the definition $\chi_z = (\nabla \times \rho \mathbf{u})_z = r^{-1}(\partial_r(r\rho v) - \partial_\theta(\rho u))$ to analyze stream-wise vortices. To distinguish from the classical vorticity $\boldsymbol{\omega} = \nabla \times \mathbf{u}$, we will call $\boldsymbol{\chi} \equiv \nabla \times \rho \mathbf{u}$ the momentum-vorticity.

An evolution equation can be derived for the momentum-vorticity by taking the curl of equation (2.2). The result can be written as:

$$\begin{aligned} \partial_t \boldsymbol{\chi} &= -\nabla \times \mathbf{l} + Re^{-1} \nabla \cdot \mu \nabla \boldsymbol{\omega} \\ &+ Fr^{-1} \nabla \times \rho \hat{\mathbf{z}} - \nabla \times (\psi \rho \mathbf{u} + K \nabla \rho) \\ &+ Re^{-1} \nabla \cdot (2\nabla \mu \times \mathbf{S}), \end{aligned} \quad (3.7)$$

in which $\mathbf{l} \equiv \boldsymbol{\chi} \times \mathbf{u}$ is the Lamb vector, $\psi \equiv \nabla \cdot \mathbf{u}$ the divergence of the velocity and $K \equiv (\mathbf{u} \cdot \mathbf{u})/2$ the kinetic energy. This equation clearly shows the contributions of the variable thermophysical properties, as the second line is equal to zero in constant density flows, whereas the last term is equal to zero in constant viscosity flows. For this reason, this equation will form the basis of our analysis of near wall streak evolution and the generation of stream-wise vortices. The physical interpretation of each term in equation (3.7) will be discussed for streaks and stream-wise vortices separately, after an observational analysis is made first, in the following sections.

3.4.1 Generation of near wall streaks

The variations in thermophysical properties in the sCO₂ cases (II and III) are found to have a clear effect on the streaks. Figure 3.8 shows the streaks both near the hot inner wall and the cold outer wall for the reference case (I) and the sCO₂ cases (II and III). The magnitude $|(\rho w)'|$ of the streaks at the hot inner wall is reduced in the forced convection case (II, see figure 3.8(b)) when compared to the reference case (I, see figure 3.8(a)). $|(\rho w)'|$ is further decreased in the mixed convection case (III, see figure 3.8(c)). The reverse, however, is true for the cold wall: $|(\rho w)'|$ is increased in the forced convection (II, see figure 3.8(e)) and mixed convection (III, see figure 3.8(f)) cases. The streaks also look slightly more disorganised in the forced convection case (II). This is even more so for the mixed convection case (III). As the ejections of streaks are largely responsible for the existence of the turbulent shear stress (Corino and Brodkey [1969]), the results described above are consistent with our earlier observations in section 3.3.3, where we observed that the magnitude of the turbulent shear stress decreases near the inner wall, and increases near the outer wall as a result of the variable thermophysical properties.

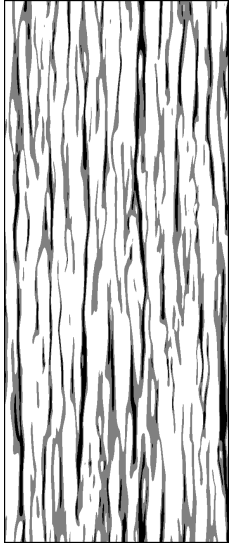
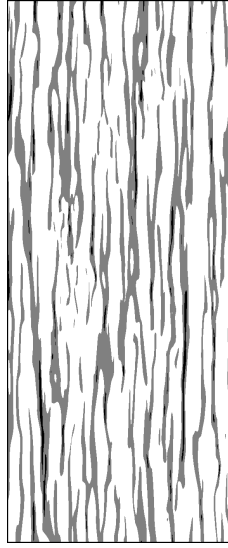
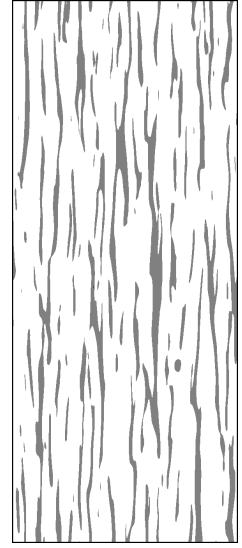
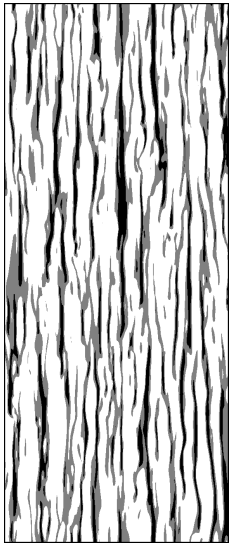
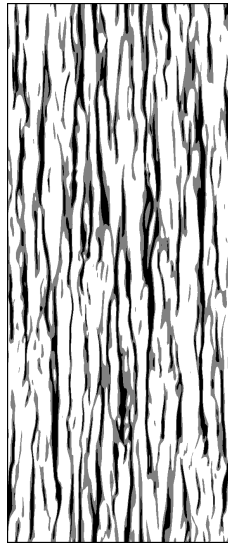
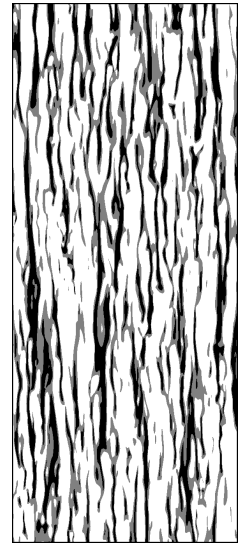
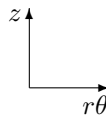
(a) reference case (I),
inner wall(b) forced sCO₂ (II),
inner wall(c) mixed sCO₂ (III),
inner wall(d) reference case (I),
outer wall(e) forced sCO₂ (II),
outer wall(f) mixed sCO₂ (III),
outer wall

Figure 3.8: Visualization of the streaks (defined as $(\rho w)' < 0$ near the hot (top) and cold (bottom) near wall region ($y^+ = 5$). Darker colours indicate larger values of $|(\rho w)'|$. The direction of the flow is upwards. Only a part of the complete circumference is shown for the cold outer wall region.

To investigate the effect of variable thermophysical properties on the streaks in a quantitative manner, we will extract instantaneous density and dynamic viscosity data from individual streak realizations in a manner that is similar to the method described by Schoppa and Hussain [2002]:

1. the location of local minima of $(\rho w)'$, with respect to the circumferential direction, denoted as θ_0 , are identified at constant y^+
2. data near the minima for different time instances is stored
3. the data from the entire length of the streak and for different time instances are superimposed on each other, so that the minima of $(\rho w)'$ are located at the same coordinate $r^{-1}(\theta - \theta_0)$.
4. by averaging the data, average thermophysical properties of a streak are acquired.
5. any quantity (...) that has been averaged according to the above described procedure will be denoted as $\langle(\dots)\rangle$.

Figures 3.9(a) and 3.9(b) show the result of the conditional averaging (streak extraction) procedure near the inner wall and the outer wall region, respectively, in the forced convection case (II). Just as stream-wise vortices redistribute mean shear to create momentum streaks, they redistribute the mean density and dynamic viscosity profile, which in turn exist because of mean heat transfer from the hot inner wall to the cold outer wall. Therefore, streaks consist of low density and dynamic viscosity fluid, near the hot inner wall. This is consistent with observations by Cheng and Ng [1982]. The exact opposite is the case for the streaks near the cold outer wall (i.e. streaks have a high density and high dynamic viscosity). The thermophysical property gradients across the streaks are the physical interpretation of the thermophysical property fluctuations that were shown earlier in figure 3.3(c). The effect of these property gradients on the generation of streaks will subsequently be discussed.

Jimenez and Pinelli [1999] investigated the evolution of streaks in a minimal box geometry by first deriving a parameter representative of streaks and subsequently deriving a transport equation for that parameter. Jimenez and Pinelli [1999] showed by artificially damping a source term in their streak evolution equation that turbulence can be suppressed or even be completely quenched. In the current study, streaks depend mostly on the radial and circumferential coordinates r and θ and they are coherent in the stream-wise coordinate z . In this study however, streaks are not as well defined as they are in Jimenez and Pinelli [1999], because the annulus in this study is not a minimal

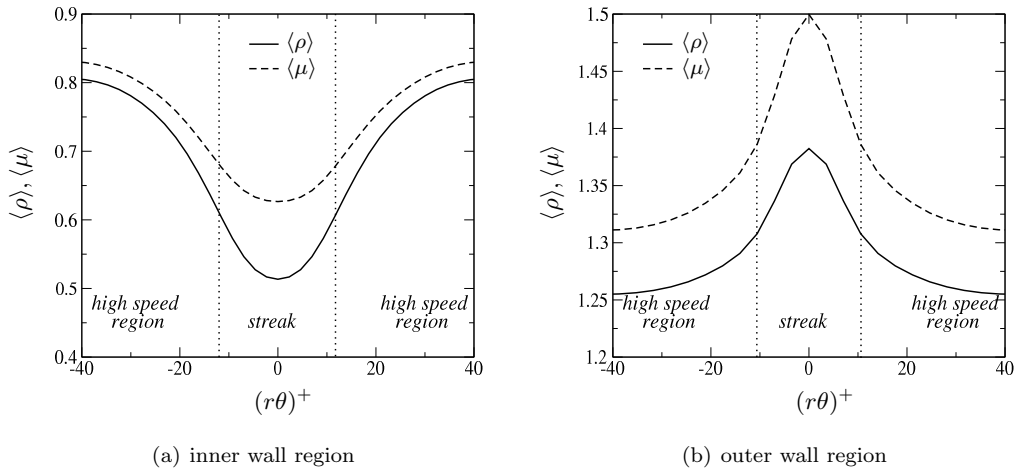


Figure 3.9: Conditionally averaged profiles of the density and dynamic viscosity across a streak at $y^+ = 10$. The dashed vertical lines represent the edges of the streak where $r^{-1}\partial_\theta(\rho w)' = 0$.

box. We will therefore define the streak parameter as the conditional average $\langle \dots \rangle$ of the radial component of the momentum vorticity χ .

$$\langle \chi_r \rangle = \langle r^{-1}\partial_\theta(\rho w) - \partial_z(\rho v) \rangle = \langle r^{-1}\partial_\theta(\rho w)' - \partial_z(\rho v)' \rangle \approx \langle r^{-1}\partial_\theta(\rho w)' \rangle \quad (3.8)$$

where we have used that $\partial_\theta(\overline{\rho w}) = 0$. $\langle \chi_r \rangle$ may therefore be thought of as the stream-wise coherent streak-flank strength and it is conceptually and physically close to the streak parameter that was defined by Jimenez and Pinelli [1999]. After applying the conditional averaging operator $\langle \dots \rangle$ to equation (3.7), an evolution equation for the stream-wise coherent streak flank strength is obtained. The end result is written as:

$$\begin{aligned} \partial_t \langle \chi_r \rangle &= -\langle (\nabla \cdot \mathbf{l})_r \rangle + Re^{-1} \langle (\nabla \cdot \mu \nabla \omega)_r \rangle \\ &+ (r Fr)^{-1} \langle \partial_\theta \rho \rangle - \langle (\nabla \times K \nabla \rho)_r \rangle - \langle (\nabla \times \psi \rho \mathbf{u})_r \rangle \\ &+ Re^{-1} \langle (\nabla \cdot 2\nabla \mu \times \mathbf{S})_r \rangle, \end{aligned} \quad (3.9)$$

We have assumed here that the operator $\langle \dots \rangle$ is linear. It is clear that for incompressible flows without variable thermophysical properties, all but the terms on the first line will be zero. Thus, the first line represents the evolution of streaks under constant thermophysical property conditions and it is the cylindrical counterpart to the streak evolution equation that is presented by Jimenez and Pinelli [1999]. These first terms represent sources of the generation of streaks and diffusion of streaks, respectively. The terms on

the second line all represent effects that may arise due to density gradients. The first term represents buoyancy, the second term involves a torque between kinetic energy and density gradients, while the third term is representative of thermal expansion effects, since by equation (2.1), $\psi = \nabla \cdot \mathbf{u}$ can be rewritten as $\psi = v^{-1}D_t v$, where v is the specific volume. The last term in the equation marks the effect of viscosity gradients on the evolution of streaks.

This equation however, may not be suited to quantify the effects of variable density and dynamic viscosity on the streak evolution with respect to the wall normal distance, because all terms will vanish after circumferential averaging. Therefore, we multiply equation (3.9) with $\langle \chi_r \rangle$ and subsequently average it with respect to the circumferential direction over an interval that is equal to $R_{in} \Delta \theta^+ = 100$ and is centred on the streak centre. This interval is close to the span-wise length of the minimal box that was used by Jimenez and Pinelli [1999]. The result is an evolution equation of what is in essence the magnitude of the stream-wise coherent streak flank strength:

$$\begin{aligned}
 \partial_t \overline{\langle \chi_r \rangle^2 / 2} &= - \underbrace{\overline{\langle \chi_r \rangle \langle (\nabla \cdot \mathbf{l})_r \rangle}}_{\text{sources}} + \underbrace{Re^{-1} \overline{\langle (\nabla \cdot \mu \nabla \omega)_r \rangle}}_{\text{diffusion \& dissipation}} \\
 &+ \underbrace{Fr^{-1} \overline{\langle \chi_r \rangle r^{-1} \langle \partial_\theta \rho \rangle}}_{\text{buoyancy}} - \underbrace{\overline{\langle \chi_r \rangle \langle (\nabla \times K \nabla \rho)_r \rangle}}_{\text{torque}} - \underbrace{\overline{\langle \chi_r \rangle \langle (\nabla \times \psi \rho \mathbf{u})_r \rangle}}_{\text{thermal expansion}} \\
 &+ \underbrace{Re^{-1} \overline{\langle \chi_r \rangle \langle (\nabla \cdot 2 \nabla \mu \times \mathbf{S})_r \rangle}}_{\text{viscosity gradient}},
 \end{aligned} \tag{3.10}$$

where $\overline{(\dots)}$ represents an average with respect to the circumferential direction. We will use this equation not only to determine the magnitude of the variable properties effects on the evolution of streaks, but also to investigate where exactly such effects are important, with respect to the wall normal distance. By multiplying equation (3.9) with $\langle \chi_r \rangle$, we have changed the meaning of the second term: it now represents the combined effects of diffusion and dissipation.

The budgets of equation (3.10), $\mathcal{B}(\overline{\langle \chi_r \rangle^2 / 2})$, are shown for the reference case (I, in grey lines) and the forced convection and mixed convection sCO₂ cases (II and III in black lines) in figure 3.10. Near the inner wall, see figure 3.10(a), the magnitude of the regular sources in the sCO₂ cases is clearly smaller than that of the reference case (I). While the sources are balanced by only diffusion and dissipation in the reference case (I), it is clear that in the sCO₂ forced convection case (II), the sources are also balanced by thermal expansion, a kinetic-energy-gradient-and-density-gradient torque and a viscosity-gradient-shear-interaction near the inner wall. In the mixed convection case (III), see figure 3.10(c), the sources are balanced by the effect of buoyancy as well. The kinetic-energy-gradient-and-density-gradient torque has a modest, yet positive effect on the coherent flank strength near in the inner wall. The thermal expansion has clearly

a negative impact on the coherent streak flank strength, while the effect of viscosity-gradient-shear-interaction has a very small, yet positive effect (near $y^+ = 8$) close to the inner wall. The influence of the thermal expansion has the largest influence.

Near the outer wall, see figures 3.10(b) and 3.10(d), the variable properties have a negligible effect, which is logical as the property variations are much smaller near the outer wall than near the inner wall. At the outer wall, the viscosity-gradient-shear-interaction acts as a sink term close to the outer wall, and as a source term further away from it. The thermal expansion and buoyancy effects are positive. The kinetic-energy-and-density-gradient torque has the smallest contribution to the coherent streak flank strength near the outer wall or $y^+ < 10$. The thermal expansion, and buoyancy terms have opposite signs at the outer wall when compared with the inner wall. This can be explained as follows: the thermophysical property gradients across the streaks and high speed fluid regions near the outer wall are of opposite sign when compared to the thermophysical property gradients across the streaks and high speed fluid regions near the inner wall, as was shown in figure 3.9. From equation (3.10) it follows then that the variable thermophysical property effects on the coherent streak flank strength should be of opposite sign as well. These results for the budgets of the coherent streak flank strength indicate that the variable thermophysical properties have a significant effect on the formation of streaks. The most prominent variable thermophysical properties effects are thermal expansion and the kinetic-energy-gradient-and-density-gradient torque.

While equation (3.10) allowed us to quantify the effect of the variable thermophysical properties on the generation of streaks, it is interesting to investigate the meaning of equation (3.10) further. The effect of the buoyancy term in the mixed convection case (III) can be interpreted as follows: as streaks and high speed fluid regions are formed by the stream-wise advection of a stream-wise vortex, they naturally have different densities, as was explained before (see also figure 3.9). Because a streak has a low density near the hot inner wall, the magnitude of the gravitational force that acts on it is smaller than the magnitude of the same force acting on a high speed, high density region. As a result, both the streaks, as well as the high speed fluid regions, will be weakened. For example, $|(\rho w)'|$ will be smaller when compared to the forced convection case (II). At the cold outer wall the opposite is true; the streaks have a high density which results in a larger gravitational force on them, while the high speed regions have a low density which results in a smaller gravitational force acting on them. Therefore, the streaks and high speed regions are enhanced near the cold outer wall ($|(\rho w)'|$ is enlarged by the gravitational force). The combination of density differences that exist across the streaks and the high speed regions and the downward pointing gravitational force acts in such a way that it counteracts the shear between the streak and high speed region near the hot wall, while it enforces it near the cold wall. As streaks are weakened near the hot

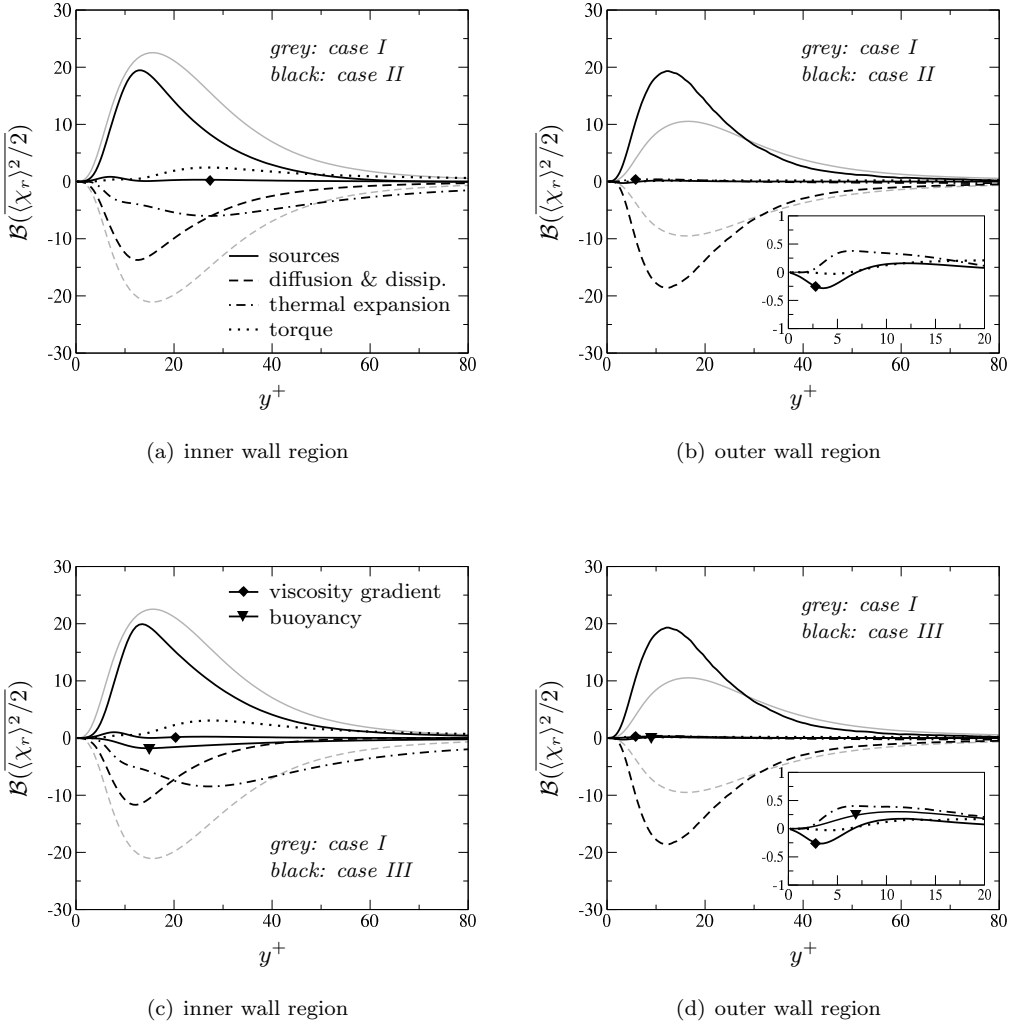


Figure 3.10: Budgets of the coherent streak flank strength $\mathcal{B}(\overline{\langle \chi_r \rangle^2 / 2})$, equation (3.10) in the reference case (I), the forced convection sCO₂ case (II) and the mixed convection sCO₂ case (III). The results have been scaled with bulk quantities.

wall and enhanced near the cold wall, it can be said that the gravitational force has a stabilizing effect on the flow field near the hot wall and a destabilizing effect near the cold wall in the present configuration. This became also clear from examining the attenuated turbulent intensities in figures 3.6(c) and 3.6(d).

The term containing the divergence of the velocity ($\psi = \nabla \cdot \mathbf{u} = r^{-1} \partial_r(ru) + r^{-1} \partial_\theta v +$

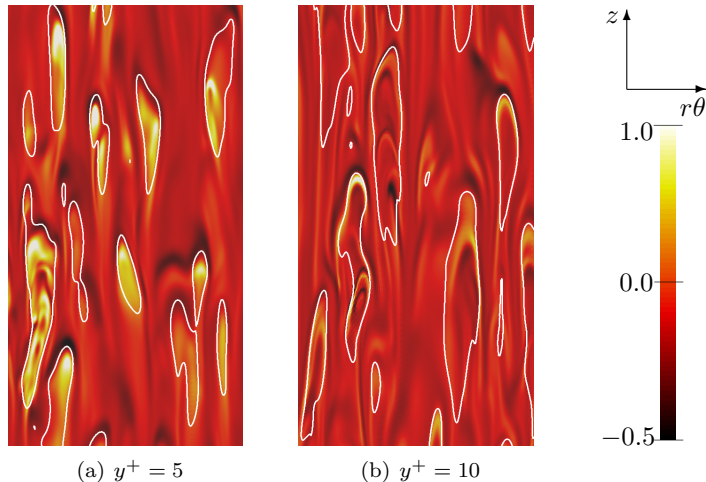


Figure 3.11: Contour plots of $\nabla \cdot \mathbf{u}$ in the (θ, z) -plane in the forced $s\text{CO}_2$ case (II). The white lines indicate iso-lines of $(\rho w)' > 0.2$.

$\partial_z w$) in equation (3.10) suggests that the thermal expansion across the streaks and high speed regions may be different. Figure 3.11 shows the divergence of the velocity at $y^+ = 5$ and $y^+ = 10$ with iso-lines of high speed momentum superimposed. At $y^+ = 5$ areas of positive thermal expansion coincide with high speed momentum regions. However, this connection between thermal expansion and high speed momentum does not seem to exist further away from the hot inner wall at $y^+ = 10$. Instead, both negative and positive values of ψ can be found across a high speed region. This observation can be tested by calculating the expected value of ψ conditioned on the fluctuating stream-wise momentum (variable conditioning was also used by Wang et al. [2012]). The results for $y^+ = 5$ and $y^+ = 10$ are shown in figure 3.12. At $y^+ = 5$, the observation that areas of positive thermal expansion coincide with high momentum fluid is indeed true. However, further away from the hot wall, this relation no longer exist. At $y^+ = 10$, the instantaneous values of ψ in figure 3.11 are large compared to the expectancy of ψ shown in figure 3.12. Therefore, areas of both positive and negative ψ and can be found at a streak or a high speed fluid region. The thermal expansion term in equation (3.10) can be interpreted as the effect that a high speed fluid region or streak may consist of both positively and negatively expanding regions, which interfere with the coherence or the formation of streaks.

The effect of the viscosity-gradient-shear-interaction was earlier shown to act as a source term close to the hot inner wall. $(\nabla \cdot \langle \nabla \mu \times \mathcal{S} \rangle)_r$ can be expanded as (see Bladel

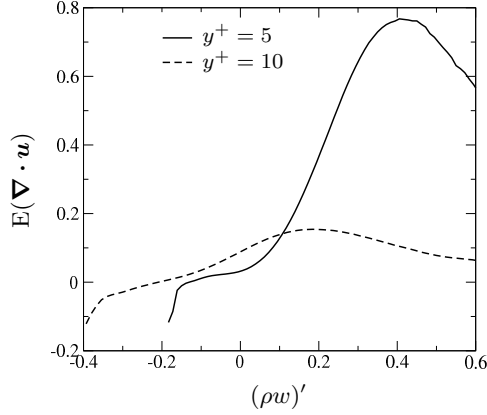


Figure 3.12: Expected value of $\nabla \cdot \mathbf{u}$ conditioned on $(\rho w)'$ in the forced convection sCO₂ case (II) at $y^+ = 5$ and $y^+ = 10$.

[2007]):

$$\begin{aligned}
 \overline{\langle \chi_r \rangle (\nabla \cdot \langle \nabla \mu \times \mathbf{S} \rangle)_r} &= \underbrace{\frac{\langle \chi_r \rangle}{r} \left\langle \frac{\partial}{\partial r} \left(r S_{zr} \frac{1}{r} \frac{\partial \mu}{\partial \theta} - r S_{\theta r} \frac{\partial \mu}{\partial z} \right) \right\rangle}_{A} & (3.11) \\
 &+ \underbrace{\frac{\langle \chi_r \rangle}{r} \left\langle \frac{\partial}{\partial \theta} \left(S_{z\theta} \frac{1}{r} \frac{\partial \mu}{\partial \theta} - S_{\theta\theta} \frac{\partial \mu}{\partial z} \right) \right\rangle}_{B} - \underbrace{\frac{\langle \chi_r \rangle}{r} \left\langle S_{r\theta} \frac{\partial \mu}{\partial z} - S_{z\theta} \frac{\partial \mu}{\partial r} \right\rangle}_{C} \\
 &+ \underbrace{\frac{\langle \chi_r \rangle}{r} \left\langle \frac{\partial}{\partial z} \left(S_{\theta r} \frac{\partial \mu}{\partial r} - S_{rr} \frac{1}{r} \frac{\partial \mu}{\partial \theta} \right) \right\rangle}_{D}
 \end{aligned}$$

Closer investigation of these terms shows that the viscosity-gradient-shear-interaction term is mostly determined by terms containing $r^{-1} \partial_\theta \mu$ and $\partial_z \mu$. More specifically, terms A and B in equation (3.11). This is shown in figure 3.13. In other words, the viscosity-gradient-shear-interaction term is determined by dynamic viscosity fluctuations, instead of the mean radial dynamic viscosity profile.

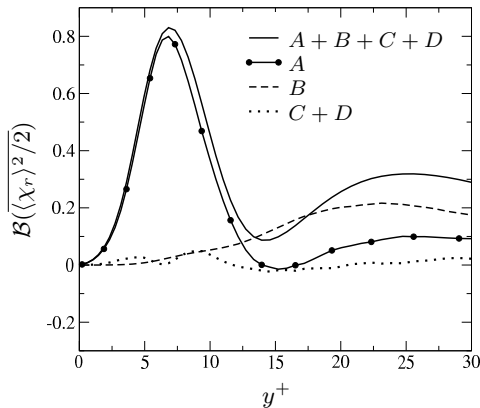


Figure 3.13: Part of $\overline{\langle \chi_r \rangle (\nabla \cdot \langle \nabla \mu \times \mathbf{S} \rangle)_r}$ that is determined by viscosity gradient fluctuations in the forced convection sCO₂ case (II). Letters refer to equation (3.11).

3.4.2 Generation of stream-wise vortical motions

Figure 3.14 shows instantaneous values of the stream-wise momentum-vorticity, χ_z , for the reference, forced convection sCO₂ (II) and mixed convection sCO₂ (III) cases. Stream-wise momentum vorticity is clearly visible at both the inner wall and the outer wall in the reference case (I), while the stream-wise momentum-vorticity is much less apparent in the forced convection sCO₂ case (II) near the inner wall. The stream-wise momentum-vorticity magnitude is not visibly decreased in the mixed convection case (III) near the inner wall. Both sCO₂ cases however, show increased momentum-vorticity near the outer wall, compared to the reference case (I). The decrease of stream-wise momentum vorticity near the inner wall suggests diminished wall-normal and circumferential motion. Vice versa, an increase of momentum vorticity suggests enhanced wall-normal and circumferential motion. The observations of the stream-wise momentum vorticity attenuation in the forced convection and mixed convection sCO₂ cases (II and III) are therefore consistent with our observations of the turbulent intensities in figure 3.6. The root mean square values of stream-wise momentum-vorticity, $\chi_z = r^{-1}(\partial_r(r\rho v) - \partial_\theta(\rho u))$, near the inner (figure 5.2(a)) and outer wall (figure 5.2(b)) reveal that the stream-wise momentum-vorticity has substantially decreased as a result of the property variations of the supercritical fluid near the inner wall and that it has increased near the outer wall. Near the inner wall, the difference between the inner wall in the forced convection sCO₂ (II) and the mixed convection sCO₂ (III) case is negligible. Near the outer wall, however, the stream-wise momentum-vortices appear to be spatially slightly larger in the mixed

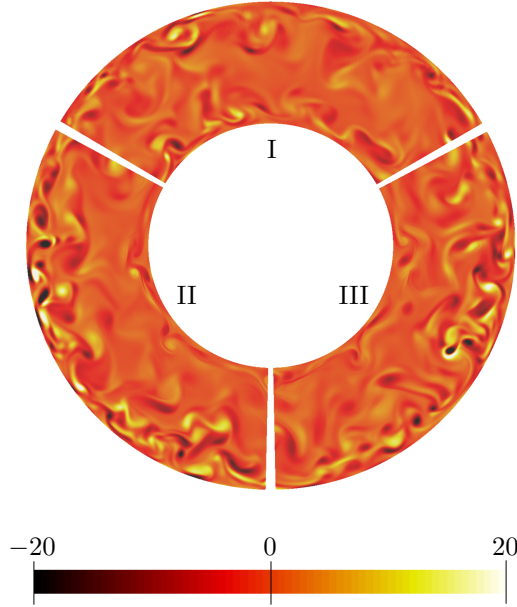


Figure 3.14: Cross-sectional visualization of the instantaneous stream-wise momentum vorticity in the reference case (I), forced convection sCO₂ (II) and mixed convection sCO₂ (III) cases.

convection sCO₂ case (III) case than they are in the forced convection sCO₂ (II) case. The magnitude of the stream-wise momentum vortices looks unaltered near the outer wall between the forced convection and mixed convection sCO₂ cases (II and III).

As before with the generation of streaks, we will use the evolution equation for momentum-vorticity to investigate how variable thermophysical properties affect stream-wise vortices. This equation is obtained by multiplying the stream-wise component of equation (3.7) with χ_z and subsequently averaging the result. The result is written as:

$$\begin{aligned}
 \partial_t(\overline{\chi_z^2/2}) &= -\underbrace{\overline{\chi_z(\nabla \times \mathbf{l})_z}}_{\text{sources}} + \underbrace{Re^{-1}(\overline{\nabla \cdot \chi_z \mu \nabla \omega_z})}_{\text{diffusion}} - \underbrace{Re^{-1}\overline{\nabla \chi_z \cdot \nabla \omega_z}}_{\text{dissipation}} \\
 &- \underbrace{\overline{\chi_z(\nabla \times \psi \rho \mathbf{u})_z}}_{\text{thermal expansion}} - \underbrace{\overline{\chi_z(\nabla K \times \nabla \rho)_z}}_{\text{torque}} \\
 &+ \underbrace{Re^{-1}\overline{\chi_z(\nabla \cdot 2\nabla \mu \times \mathbf{S})_z}}_{\text{viscosity gradient shear interaction}},
 \end{aligned} \tag{3.12}$$

where the first line represents sources, diffusion and dissipation of stream-wise momentum-vorticity, the second line represents the effects of variable density in the form of thermal expansion and a kinetic-energy-gradient-and-density-gradient torque and where the third

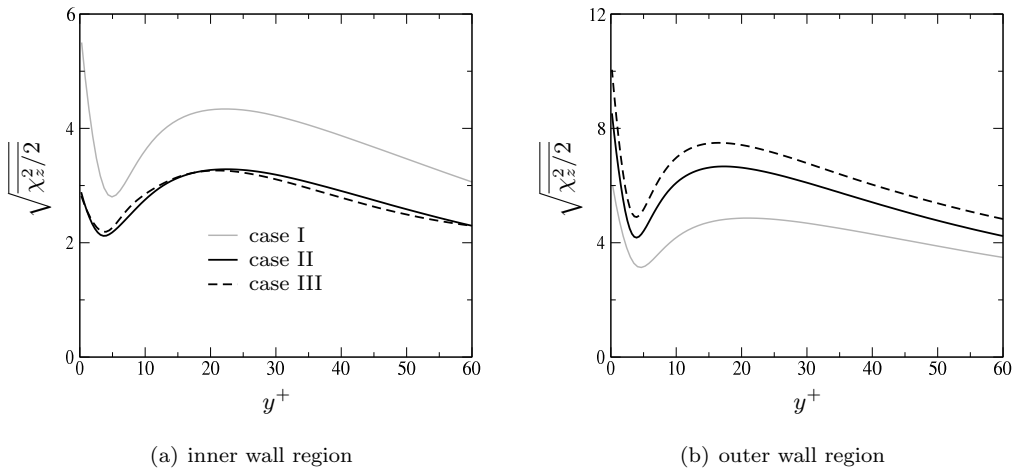


Figure 3.15: Root mean square values of the stream-wise momentum vorticity in the near wall regions in the reference case (I), forced convection sCO₂ (II) and mixed convection sCO₂ (III) case.

line represents the effect of variable-dynamic-viscosity-shear-interaction, as before. The buoyancy term is not shown here, because $Fr^{-1}(\nabla \times \rho \hat{z})_z = \mathbf{0}$, which suggests that the stream-wise momentum vortices are not directly affected by buoyancy. This is also supported by the rms-values of the stream-wise momentum-vorticity near the inner wall in figure 3.15.

The budgets $\mathcal{B}(\overline{\chi_z^2/2})$ of equation (3.12) are shown in figure 3.16 for the reference case (I) and the sCO₂ cases (II and III). Near the inner wall (figures 3.16(a) and 3.16(c)), in both the forced convection and the mixed convection sCO₂ cases (II and III), the contribution of the regular sources is smaller than it is in the reference case, except for a small region between $y^+ = 8$ and $y^+ = 23$ for the forced convection case and $y^+ = 10$ and $y^+ = 18$ for the mixed convection case. Near the outer wall however (figures 3.16(b) and 3.16(d)), the contribution of the regular sources is larger for all y^+ . The viscosity-gradient-shear-interaction has a negligible effect on the formation of stream-wise momentum vortices. The effect of thermal expansion is more significant than the variable viscosity effect, but only marginally. Both the variable viscosity and thermal expansion terms act as sink terms. The torque created by the kinetic energy and density gradients however, has a significant effect, as it is larger than the combined effects of diffusion and dissipation near the inner wall in both the forced convection case (II) and the mixed convection case (III). This is not the case near the outer wall, where it is

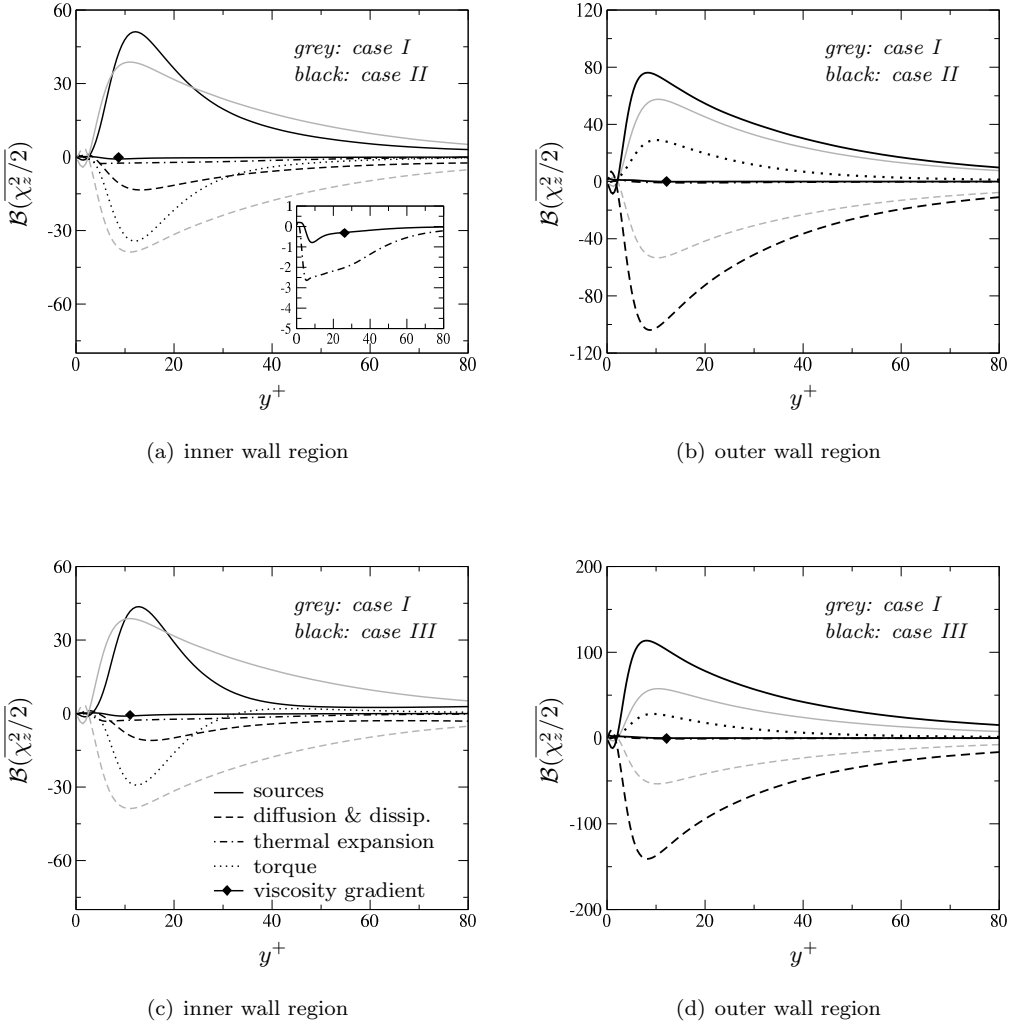


Figure 3.16: Budgets of the stream-wise vorticity $\mathcal{B}(\overline{\chi_z^2/2})$, equation (3.12). Black lines are used for the forced convection (II) and mixed convection (III) sCO₂ cases, while grey lines are reserved for the reference case (I).

smaller, yet still substantial compared to regular sources. The torque acts as a sink near the inner wall, but as a source near the outer wall. The changes in the regular sources in the sCO₂ cases (II and III) compared to the reference case (I) combined with the effects of the torque explains why the rms-values of the stream-wise momentum vortices of figure 16 are smaller in the sCO₂ cases (II and III) near the inner wall and larger near

the outer wall. The fact that the regular sources are larger near the outer wall in the mixed convection case (III) than in the forced convection case (II) is consistent with the rms values near the outer wall as well.

The torque effect can be further clarified by looking at figure 3.17. In this figure, a typical ejection of low speed, low density fluid near the hot inner wall is shown. This ejection generates a region of negative stream-wise momentum vorticity χ_z^- and a region of positive stream-wise momentum vorticity χ_z^+ , which have been marked by black iso-lines superimposed on the vector field $(\rho u, \rho v)^T$ in figure 3.17(a). The iso-contours of the kinetic energy and the density, shown in figure 3.17(b), are clearly not parallel, which indicates that $-\nabla K \times \nabla \rho = \nabla \rho \times \nabla K$ is non-zero. Figure 3.17(c) shows the kinetic energy and density gradient vectors. In the inner part of the mushroom like structure (region A and A'), the torque acts as to create a region of positive stream-wise momentum vorticity near A and a region of negative stream-wise momentum vorticity near A', see figure 3.17(d). At the top of the mushroom-like structure (region B and B'), the opposite occurs: the torque acts as to create negative stream-wise vorticity near B' and positive stream-wise vorticity near B. Therefore, the torque between the kinetic energy gradient and the density gradient both counteracts as well as aids the stream-wise momentum vorticity generated by the unstable low speed region. It is clear that the kinetic energy and density gradient vectors are almost parallel at the top, yet almost perpendicular to each other inside the mushroom-like structure. Thus, the magnitude of the torque is much smaller at the top near B and B' (as parallel gradients of the kinetic energy and density result in $\nabla \rho \times \nabla K = \mathbf{0}$) than the magnitude of the torque near the inner part near A and A' (where $\nabla \rho$ and ∇K make an almost 90° angle). The net result is that the torque acts as a sink term to the formation of stream-wise momentum-vorticity near a hot inner wall, which was also shown in figure 3.16. At the cold outer wall, high density fluid is ejected instead of low density fluid. This means that for a similar mushroom-like structure near the outer wall, the density gradient vector is of opposite sign when compared to the same vector near the inner wall. Therefore, near the outer wall, the kinetic-energy-gradient-and-density-gradient torque acts as a source term for the formation of stream-wise momentum vorticity on average, which can also be seen in figure 3.16. From the direction of the density gradient vector near the inner part of the mushroom-like structure it is clear that both $\partial_r \rho$ as well as $r^{-1} \partial_\theta \rho$ are important here, which shows that the density fluctuations are important to the generation of stream-wise vortices and thus in the turbulence attenuation that may occur in heated or cooled turbulent flows at supercritical pressure.

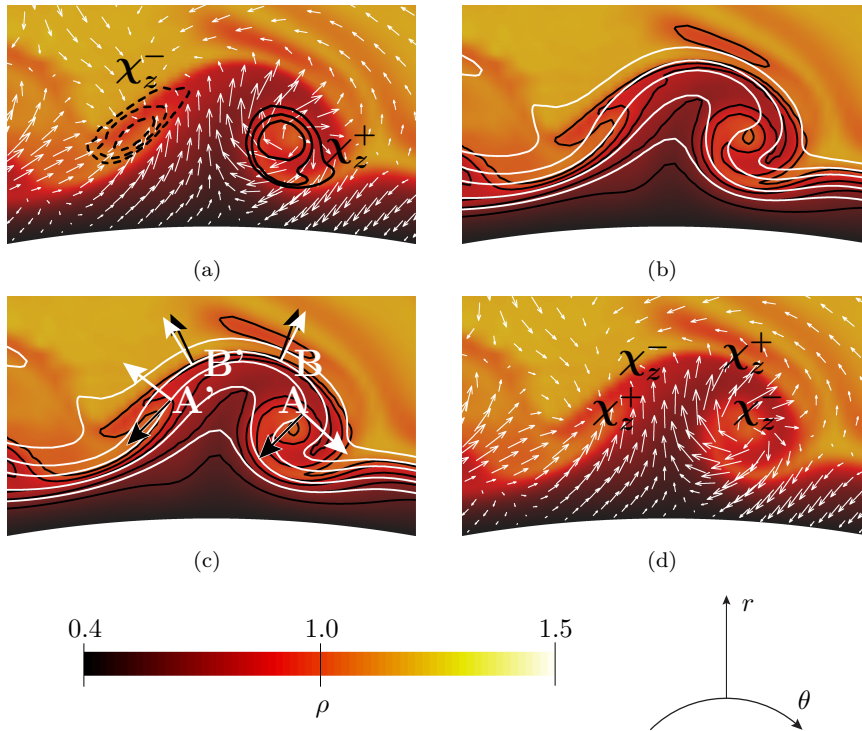


Figure 3.17: Four depictions of the same burst of a low speed, low density region near the inner wall in the wall normal plane. In (a), the momentum vector field is shown (not all vectors are shown). The solid contour lines indicate positive stream-wise vorticity, while the dashed contour lines indicate negative stream-wise momentum vorticity. In (b), the black contour lines are iso-density lines, the white lines represent iso-kinetic energy lines. Figure (c) shows the gradient vectors (not to scale) of the kinetic energy (white) and the density (black). Figure (d) shows locations of positive and negative stream-wise vorticity that are induced by the kinetic-energy-gradient-and-density-gradient torque.

3.4.3 Molecular Prandtl number effect

In the previous discussion it has become clear that thermophysical property fluctuations that occur as a result of the self regenerating process play an important role in the generation of streaks and stream-wise momentum vorticity. In this section, we will investigate how variable property effects scale between the forced convection sCO₂ case (II), the variable density case (IV) and the variable dynamic viscosity case (V). The magnitude of the thermophysical property fluctuations is only determined by the magnitude of the enthalpy fluctuations (under the low Mach number approximation assumption), which are in turn determined by the Reynolds number and the molecular Prandtl number. The variable thermophysical property effects on the generation of streaks and stream-wise momentum-vorticity should then be determined by the Prandtl number as well. In turbulent flows, gradients of fluctuations are typically larger than gradients of mean quantities (see for instance Tennekes and Lumley [1972]). Following Tennekes and Lumley [1972], we will choose \mathcal{U} to be a reference velocity scale and λ to be the Taylor micro-scale. The gradient of a velocity fluctuation then is $\mathcal{O}(\mathcal{U}/\lambda)$. Then, if λ_{th} is the thermal energy analogue of λ and \mathcal{R} the reference density scale, it follows for density gradient fluctuations that:

$$\nabla\rho \propto \mathcal{O}\left(\frac{\mathcal{R}}{\lambda_{th}}\right) = \mathcal{O}\left(\frac{\mathcal{R}}{\lambda}\frac{\lambda}{\lambda_{th}}\right) = \mathcal{O}\left(\frac{\mathcal{R}}{\lambda}\sqrt{Pr}\right). \quad (3.13)$$

We used here that $\lambda/\lambda_{th} = \sqrt{Pr}$, see Batchelor [1959]. Similar arguments can be made for the divergence of the velocity:

$$\nabla \cdot \mathbf{u} \propto \mathcal{O}\left(\frac{\mathcal{U}}{\lambda_{th}}\right) = \mathcal{O}\left(\frac{\mathcal{U}}{\lambda}\frac{\lambda}{\lambda_{th}}\right) = \mathcal{O}\left(\frac{\mathcal{U}}{\lambda}\sqrt{Pr}\right). \quad (3.14)$$

A similar estimate can be made for viscosity gradient fluctuations, but since the variable density effects are of greater importance to the generation of streaks and stream-wise momentum vorticity, we will focus on the variable density effects only. The scaling estimates (3.13), (3.14) suggest that if \mathcal{R} (or \mathcal{U}) and λ are kept constant under different conditions, that any property gradient term in equations (3.10) and (3.12) should scale with \sqrt{Pr} . Qualitatively, this suggests that the magnitude of the variable property effects between the sCO₂ forced convection case (II) and the variable density (IV) or dynamic viscosity case (V) scale with a factor of $\gamma \equiv (\overline{Pr}^{forced}/Pr^{ref})^{1/2}$, if λ remains the same (which is reasonable because the local Reynolds numbers are very similar). Note that \overline{Pr}^{forced} refers to the average molecular Prandtl number in case II (which varies from 1.6 to 12), while Pr^{ref} refers to the molecular Prandtl number in cases I, IV and V (which is equal to 2.85). Figure 3.18 shows the factor γ as function of the wall distance. The profile of γ suggests that the variable property effects of the sCO₂ case (II) should be

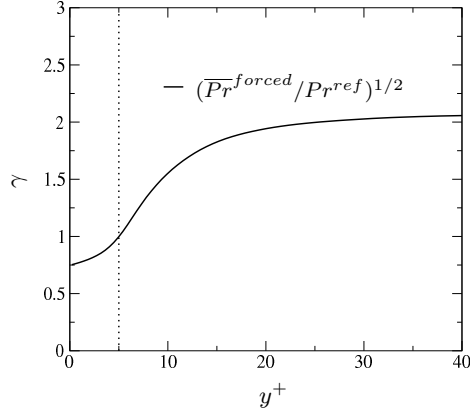


Figure 3.18: The factor $\gamma \equiv (\overline{P_r}^{forced} / P_r^{ref})^{1/2}$ as a function of the inner wall distance. The vertical dotted line denotes the position where $\overline{P_r}^{forced} = P_r^{ref}$.

smaller than those of the variable density and dynamic viscosity cases for $y^+ < 5$ and vice versa for $y^+ > 5$.

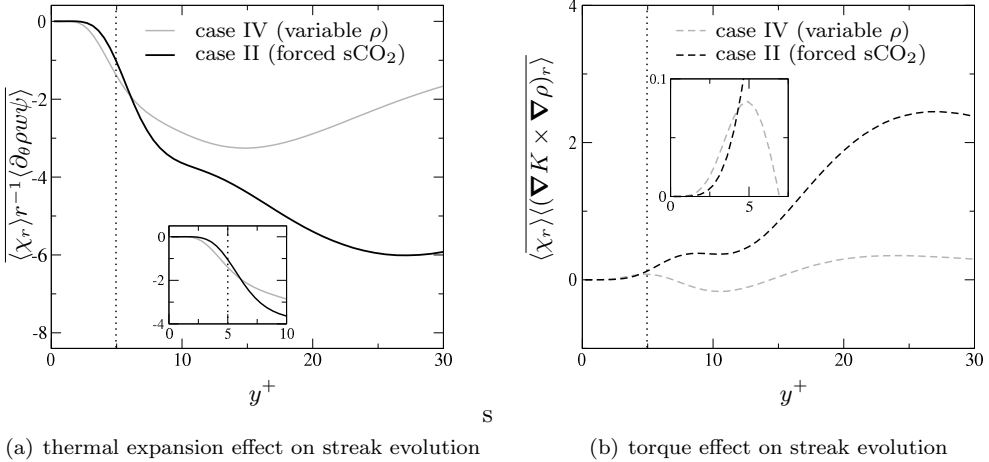
Figure 3.19 shows again the thermal expansion term and the kinetic-energy-gradient-and-density-gradient torque of equation (3.10), but now for both the sCO₂ case (II) and the variable density (IV) case. The region where the thermal expansion effect in the variable density case (IV) is larger than that of the sCO₂ forced convection sCO₂ case (II) is found for $y^+ < 6$, which is close to the point where $\overline{P_r}^{forced} = P_r^{ref}$. It can be seen that the thermal expansion effect in the forced convection sCO₂ case shows a sudden increase near $y^+ = 10$, when compared with the variable density case (IV). This is logical according to estimate (3.14), as γ strongly increases around $y^+ = 10$, see figure (3.18), with respect to the wall normal distance. The physical interpretation is that due to the increase of the Prandtl number with y^+ , the thermal fluctuations will increase with y^+ in the forced convection sCO₂ case when compared to the variable density case (IV), which results in the sudden increase in the magnitude of the thermal expansion term. It should be noted here that differences in turbulence intensities also affect the magnitude of the thermal fluctuations; this is further discussed in chapter 4.

The kinetic-energy-gradient-and-density-gradient torque shows a similar trend as the thermal expansion term. The torque is smaller in the forced convection sCO₂ case (II) for $y^+ < 4.3$ than it is in the variable density case (IV). For $y^+ > 5$, the torque effect is much larger in the sCO₂ case (II). Near $y^+ = 10$, the torque is slightly negative in the variable density case (IV), while in the forced convection sCO₂ case, it is slightly

positive: this difference cannot be explained by the scaling estimate (3.13).

The effect of the kinetic-energy-gradient-and-density-gradient torque on stream-wise vorticity is shown in figure 3.20. The region where the kinetic-energy-gradient-and-density-gradient torque is larger in the variable density case (IV) than it is in the forced convection sCO₂ (II) case, is found for $y^+ < 8.6$. Before, we assumed that λ would be constant between the cases. However, if we assume that this does not hold for the momentum vorticity length scales, the scaling estimate 3.13 suggests that the effect of the kinetic-energy-gradient-and-density-gradient torque in the forced convection sCO₂ case (II) to that of the variable density case (IV), scales as $(\lambda^{IV}/\lambda^{II})\gamma$. This suggests that the spatial scales of the stream-wise momentum vorticity are different between the sCO₂ (II and III) and variable density (IV) cases.

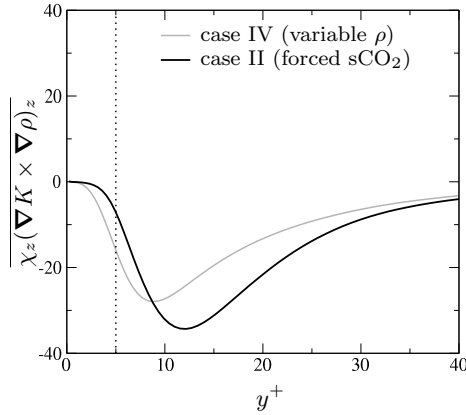
While the scaling arguments that were made above should be seen as a qualitative analysis, it is reasonable to assume that the variable Prandtl number of fluids at supercritical pressure has a clear effect on the evolution of turbulent structures, through the magnitude of the variation of the density gradients.



(a) thermal expansion effect on streak evolution

(b) torque effect on streak evolution

Figure 3.19: Comparison of the thermal expansion term (left) and kinetic-energy-gradient-and-density-gradient torque (right) in equation (3.10) between the sCO₂ forced convection case (II) and the constant molecular Pr cases (grey lines). The vertical dotted line denotes the position where $\overline{Pr}^{forced} = Pr^{ref}$.



(a) torque effect on stream-wise momentum vorticity

Figure 3.20: Comparison of the kinetic-energy-gradient-and-density-gradient torque equation (3.12) between between the sCO₂ forced convection case (black lines), the variable density case (grey lines). The vertical dotted line denotes the position where $\overline{Pr}^{forced} = Pr^{ref}$.

3.5 Conclusions

In this chapter, we have investigated the effect of variable thermophysical properties of supercritical fluids on a turbulent annular flow that is heated at the inner wall and cooled at the outer wall by means of direct numerical simulations. Near the inner wall, the fluid has a low density and dynamic viscosity and vice versa at the outer wall. Due to the fact that both walls are kept at different temperatures, a mean radial dynamic viscosity and density profile exists. Large density and viscosity variations were found near the inner wall.

While looking at classical turbulent statistics, it was found that the mean velocity profiles, turbulent shear stresses and turbulent intensities were significantly affected by the mean variation in dynamic viscosity and density. The differences in mean strain rate and turbulent shear stresses lead to a decreased production of turbulent kinetic energy near the hot inner wall and an enhanced production near the outer wall. However, these observations did not show how the variable properties have a direct influence on turbulent motions. To investigate further, turbulent structures were analysed in detail.

As stream-wise momentum vortices interact with the mean velocity to create streaks, they also interact with the mean density and mean dynamic viscosity. As a result, low speed streaks near the hot wall have a low density and dynamic viscosity, compared to the high speed fluid that surrounds them. Both positive and negative thermal expansion regions existing within the streaks were found to have a negative impact on the coherence of the streaks. The dynamic viscosity gradient across the streaks was observed to act as a source term very close to the inner wall and to be negligible to variable density effects. Buoyancy acts as to counteract the shear between low density momentum streaks and high density, high speed regions in buoyancy opposed flow. The opposite holds for the cold outer wall as the thermophysical property gradients across the streaks are of opposite sign compared to the gradients across the streaks near the inner wall. The density and dynamic viscosity fluctuations therefore influence the stream-wise momentum fluctuations directly.

The stream-wise vorticity was found to be negligibly affected by the dynamic viscosity fluctuations and thermal expansion. However, the torque between the kinetic energy gradient and the density gradient was found to act as a very large sink term near the inner wall and as a source term near the outer wall. It was shown that stream-wise momentum vorticity, created by the instability of a low speed region, is counteracted or enhanced by this torque. Both the radial density gradient as well as the circumferential density gradient were found to be important; the density and dynamic viscosity fluctuations therefore also influence the wall normal and circumferential turbulent motions of the fluid.

As both streaks and stream-wise vortices are important to the self regenerating near wall cycle, it is feasible that a complete disruption of this cycle, and thus relaminarisation, may occur as a result of thermal expansion, a viscosity-gradient-shear-interaction, buoyancy as well as a kinetic-energy-gradient-and-density-gradient torque in heated supercritical fluids. In other words, local thermophysical property variations can be responsible for decreased or increased turbulent motions in heated or cooled fluids at supercritical pressure.

Bibliography

- Joong Hun Bae, Jung Yul Yoo, and Haecheon Choi. Direct numerical simulation of turbulent supercritical flows with heat transfer. *Physics of Fluids*, 17(10):105104, 2005.
- Joong Hun Bae, Jung Yul Yoo, and Donald M. McEligot. Direct numerical simulation of heated CO₂ flows at supercritical pressure in a vertical annulus at Re=8900. *Physics of Fluids*, 20(5):055108, 2008.
- G. K. Batchelor. Small-scale variation of convected quantities like temperature in turbulent fluid part 1. General discussion and the case of small conductivity. *Journal of Fluid Mechanics*, 5:113–133, 1959. ISSN 1469-7645.
- J. Bladel. *Electromagnetic Fields*. Wiley-IEEE Press, 2007.
- B. J. Boersma. A 6th order staggered compact finite difference method for the incompressible Navier-Stokes and scalar transport equations. *Journal of Computational Physics*, 230(12):4940 – 4954, 2011a.
- B. J. Boersma. Direct numerical simulation of turbulent pipe flow up to a Reynolds number of 61,000. In *Journal of Physics: Conference Series*, volume 318. IOP publishing, 2011b. 13th European Turbulence Conference (ETC13).
- B. J. Boersma and W.-P. Breugem. Numerical Simulation of Turbulent Flow in Concentric Annuli. *Flow, Turbulence and Combustion*, 86(1):113–127, 2011.
- R. K. Cheng and T. T. Ng. Some aspects of strongly heated turbulent boundary layer flow. *Physics of Fluids*, 25(8):1333–1341, 1982.
- E. R. Corino and Robert S. Brodkey. A visual investigation of the wall region in turbulent flow. *Journal of Fluid Mechanics*, 37:1–30, 1969.
- L. Duan, I. Beekman, and M. P. Martin. Direct numerical simulation of hypersonic turbulent boundary layers. Part 3. Effect of Mach number. *Journal of Fluid Mechanics*, 672:245–267, 2011.
- A. Fenghour, W. A. Wakeham, and V. Vesovic. The viscosity of carbon dioxide. *Journal of Physical and Chemical Reference Data*, 27:31–44, 1998.
- J. M. Hamilton, J. Kim, and F. Waleffe. Regeneration mechanisms of near-wall turbulence structures. *Journal of Fluid Mechanics*, 287:317–348, 3 1995.

- J. Jimenez and A. Pinelli. The autonomous cycle of near-wall turbulence. *Journal of Fluid Mechanics*, 389:335–359, 1999.
- H. Kawamura, K. Ohsaka, H. Abe, and K. Yamamoto. DNS of turbulent heat transfer in channel flow with low to medium-high Prandtl number fluid. *International Journal of Heat and Fluid Flow*, 19:482–491, 1998.
- J. Kim. Physics and control of wall turbulence for drag reduction. *Philosophical Transactions of the Royal Society A*, 369:1396–1411, 2011.
- O. Kunz, W. Wagner R. Klimeck, and M. Jaeschke. The GERG-2004 wide-range equation of state for natural gases and other mixtures. Technical report, 2007. GERG Technical Monograph 15, Fortschritt-Berichte VDI, VDI-Verlag, Düsseldorf.
- V.A. Kurganov and A.G. Kaptil'ny. Velocity and enthalpy fields and eddy diffusivities in a heated supercritical fluid flow. *Experimental Thermal and Fluid Science*, 5(4):465 – 478, 1992.
- J. Lee, A.Y. Jung, J.J. Sung, and T.A. Zaki. Effect of wall heating on turbulent boundary layers with temperature-dependent viscosity. *Journal of Fluid Mechanics*, 726:196–225, 2013.
- E.W. Lemmon, M.L. Huber, and M.O. McLinden. NIST standard reference database 23: Reference fluid thermodynamic and transport properties-REFPROP. Version 9.1, National Institute of Standards and Technology, Standard Reference Data Program, Gaithersburg, 2013.
- P.D. McMurtry, W.-H. Jou, J. Riley, and R.W. Metcalfe. Direct numerical simulations of a reacting mixing layer with chemical heat release. *AIAA Journal*, 24(6):962–970, 1986.
- H. N. Najm, P. S. Wyckoff, and O. M. Knio. A semi-implicit numerical scheme for reacting flow: I. stiff chemistry. *Journal of Computational Physics*, 143(2):381 – 402, 1998.
- H. Nemati, A. Patel, B.J. Boersma, and R. Pecnik. Mean statistics of a heated turbulent pipe flow at supercritical pressure. *International Journal of Heat and Mass Transfer*, 83:741 – 752, 2015.
- K. Nishikawa and I. Tanaka. Correlation lengths and density fluctuations in supercritical states of carbon dioxide. *Chemical Physics Letters*, 244:149–152, 1995.

- A. Patel, J.W.R. Peeters, B.J. Boersma, and R. Pecnik. Semi-local scaling and turbulence modulation in variable property turbulent channel flows. *Physics of Fluids*, 27(9): 095101, 2015.
- B.S. Petukhov and A.F. Polyakov. *Heat transfer in turbulent mixed convection*. Hemisphere publishing corporation, 1988.
- W. Schoppa and F. Hussain. Coherent structure generation in near-wall turbulence. *Journal of Fluid Mechanics*, 453:57–108, 2002.
- H. Tennekes and J. L. Lumley. *A First Course in Turbulence*. The MIT Press, Cambridge, 1972.
- V. Vesovic, W. Wakeham, G. Olchoway, J. Sengers, J. Watson, and J. Millat. The transport properties of carbon dioxide. *Journal of Physical and Chemical Reference Data*, 19:763, 1990.
- F. Waleffe. On a self-sustaining process in shear flows. *Physics of Fluids*, 9:883–900, 1997.
- J. Wang, Y. Shi, L.-P. Wang, Z. Xiao, X.T. He, and S. Chen. Effect of compressibility on the small-scale structures in isotropic turbulence. *Journal of Fluid Mechanics*, 713: 588–631, 2012.
- W. W. Willmarth and S. S. Lu. Structure of the reynolds stress near the wall. *Journal of Fluid Mechanics*, 55:65–92, 1972.
- B. Zappoli, D. Beysens, and Y. Garrabos. *Heat transfers and related effects in supercritical fluids*. Springer, 2015.
- F. Zonta. Nusselt number and friction factor in thermally stratified turbulent channel flow under Non-Oberbeck-Boussinesq conditions. *International Journal of Heat Fluid Flow*, 44:489–494, 2013.
- F. Zonta and A. Soldati. Effect of temperature dependent fluid properties on heat transfer in turbulent mixed convection. *Journal of Heat Transfer*, 136:022501–1, 2014.
- F. Zonta, C. Marchioli, and A. Soldati. Modulation of turbulence in forced convection by temperature-dependent viscosity. *Journal of Fluid Mechanics*, 697:150–174, 2012.
- F. Zonta, C. Marchioli, and A. Soldati. Turbulence and internal waves in stably-stratified channel flow with temperature-dependent fluid properties. *Journal of Fluid Mechanics*, 697:175–203, 2012.

CHAPTER 4

HEAT TRANSFER ATTENUATION

4.1 Introduction

In the previous chapter, it was shown that density and dynamic viscosity variations can either attenuate or enhance turbulent motions in a fluid. The thermophysical property variation does not only ‘reconstruct’ total shear stress profiles (and therefore turbulent shear stress profiles), but also the turbulent structures that are integral parts of the self regenerating cycle. In this chapter, heat transfer attenuation and enhancement by variations in thermophysical properties are investigated. Specifically, the effects of variations in the specific heat capacity, thermal diffusivity, density and molecular Prandtl number on turbulent heat transfer are emphasised. Figure 4.1 show that the specific heat capacity c_p , molecular Prandtl number Pr , thermal diffusivity a and thermal conductivity k vary significantly with the temperature. Understanding how these thermophysical properties variations of a fluid at supercritical pressure affect heat transfer may help to develop better heat transfer models.

The lay-out of this chapter is as follows: firstly, three numerical cases that were also used in the previous chapters are briefly described again for purposes of readability. Subsequently, the effects of the thermophysical properties variations on heat transfer is meticulously analysed. At the end, the conclusions are presented.

4.2 Numerical cases

We will use three of the numerical cases that were described in the previous chapter to analyse how the variations of the thermophysical properties affect heat transfer. The annular geometry and simulation methods were described in chapter three and will not be repeated here. For ease of reading, we will reiterate the specifics of the investigated cases, though. The details of these cases are summarised in table 4.1. The results of the sCO₂ cases (II and III) will be compared against the results of the reference case (I).

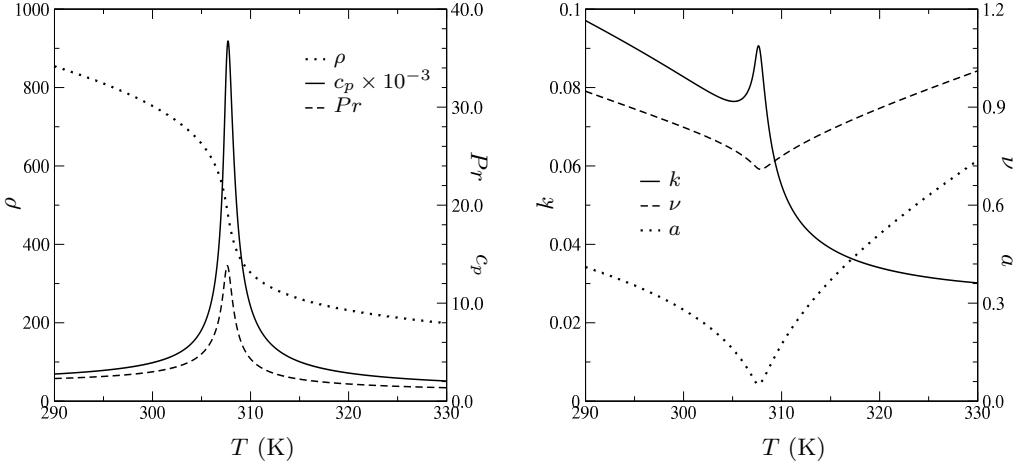


Figure 4.1: Properties of CO₂ at 8 MPa. Shown are the density ρ (kg/m³), the specific heat capacity c_p (J/kg.K), the molecular Prandtl number Pr (–), the thermal conductivity k (W/m.K), the kinematic viscosity ν (m²/s) and the thermal diffusivity a (m²/s).

| case | properties | Pr |
|------------------------------|--------------------------|--------|
| reference (I) | constant | 2.85 |
| forced sCO ₂ (II) | sCO ₂ (8 MPa) | 1.6–14 |
| mixed sCO ₂ (III) | sCO ₂ (8 MPa) | 1.6–14 |

| case | flow condition | Fr^{-1} | grid size |
|------------------------------|-------------------|-----------|-----------------|
| reference (I) | forced convection | 0 | 192 × 480 × 512 |
| forced sCO ₂ (II) | forced convection | 0 | 256 × 768 × 768 |
| mixed sCO ₂ (III) | mixed convection | -0.1 | 256 × 768 × 768 |

Table 4.1: Case details of the numerical simulations.

Mixed convection conditions are only considered in the last case (III); heated upward flow occurs near the inner wall, while cooled upward flow occurs near the outer wall. In all three cases, the wall temperatures are kept constant; the inner wall is kept at $T^o = 323$ K, while the outer wall is kept at $T^o = 303$ K. In both sCO₂ cases, T_{pc} can be found close to the inner wall. The reference Prandtl number Pr_h is equal to 2.85 in all three cases. The molecular Prandtl number $Pr = \mu^o c_p^o / k^o$, is equal to Pr_h in the reference case. In the sCO₂ cases, however, the molecular Prandtl number varies by an order of magnitude. The Reynolds number equals 8000 in all cases.

4.3 Mean statistics

In this section we aim to characterise the differences between turbulent heat transfer in fluids at super-critical pressure and fluids with constant thermophysical properties. We will begin by discussing instantaneous visualizations of the enthalpy, temperature and thermophysical properties in the forced convection sCO₂ case (II). Then, for each case, we will show mean statistics of the thermophysical property variations as well as the turbulent intensities. These observations are necessary for the analyses that follow thereafter.

We will first analyse the effect of the variable specific heat capacity on heat transfer by comparing the mean thermal statistics (specifically the mean enthalpy and temperature profiles, the enthalpy and temperature rms values, as well as their respective probability density functions) between the different cases. We will proceed by analysing how the molecular and turbulent heat fluxes are affected by the variable thermal diffusivity as well as the molecular Prandtl number. Subsequently, we will analyse the effect of the instantaneous variations of the Prandtl number and the density by using conditional averaging techniques in conjunction with a relation between the Nusselt number and the turbulent heat flux. This analysis shows how the turbulent heat flux is influenced by fluctuations of the molecular Prandtl number as well as the density.

4.3.1 Mean thermophysical property and velocity statistics

Before discussing the mean thermophysical property variations, it is convenient to write equation (2.3) completely in terms of enthalpy (see A.1.4 for a derivation):

$$\partial_t(\rho h) + \nabla \cdot \rho \mathbf{u} h = (RePr_h)^{-1} \nabla \cdot \rho a \nabla h. \quad (4.1)$$

Equation (4.1) shows that the evolution of enthalpy is determined by the Reynolds and the reference Prandtl number, as well as the variations in the density and the thermal diffusivity $a \equiv k/(\rho c_p)$. The variation of the temperature can then be discussed by means of $dh = c_p dT$ (see A.1.4). Therefore, when discussing the effect of variable thermophysical properties on (turbulent) heat transfer, we will restrict the discussion to the effect of ρ , a and c_p . The molecular Prandtl number $Pr = \mu c_p/k$ will be used to discuss the transport of heat in relation to the transport of momentum.

Figure 4.2 (left) shows instantaneous values of the enthalpy, temperature and specific heat capacity. The temperature fluctuations are much less apparent than the enthalpy fluctuations. Starting at the hot inner wall, the specific heat capacity is small. Further away from it, however, c_p has a much larger value. Qualitatively, this explains why the temperature fluctuations are much less apparent than the enthalpy fluctuations; the large value of the specific heat capacity suppresses the temperature fluctuations. Figure

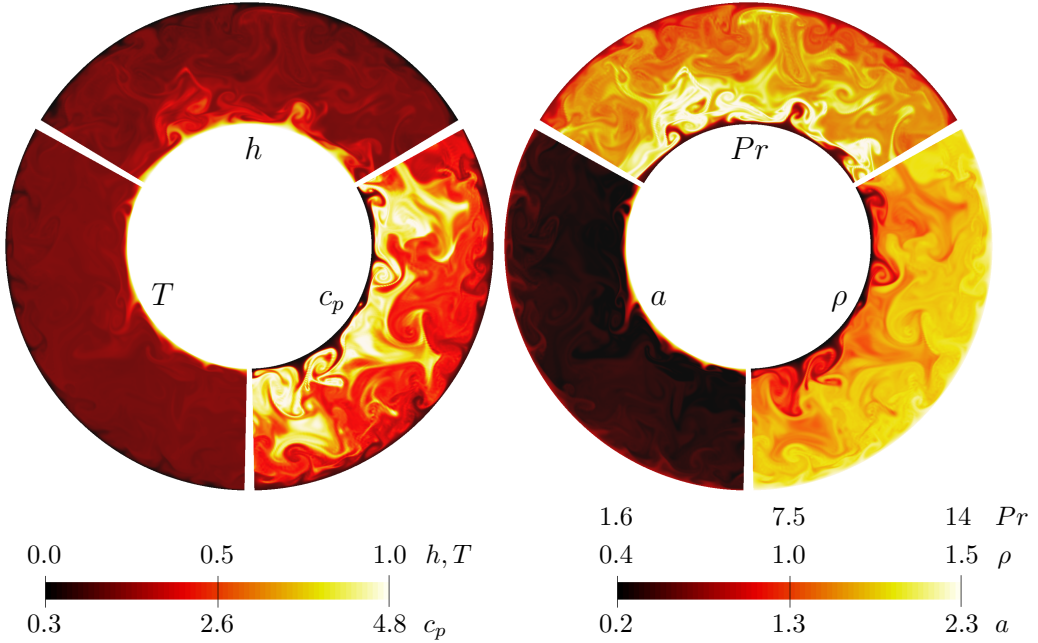


Figure 4.2: Instantaneous cross-sectional visualization of thermophysical properties for the super-critical forced convection case. On the left, the enthalpy, temperature and specific heat capacity are shown. On the right, the molecular Prandtl number, thermal diffusivity and density are shown.

4.2 shows instantaneous values of the thermal diffusivity, the density and the molecular Prandtl number. Hot fluid near the inner wall has low thermal diffusivity, density and a low Prandtl number. Especially the Prandtl number and the thermal diffusivity show large variations. The Prandtl number has a maximum quite close to the inner wall, while the thermal diffusivity has a large value at the inner wall, but rapidly decreases with wall distance.

Figure 4.3 shows the mean variation of the density, thermal diffusivity, density and the molecular Prandtl number near the inner (left) and the outer wall (right) as a function of the wall distance y^+ , which is defined as $y^+ = (r - R_{in})/\delta_{\nu,in}$ and $y^+ = (R_{out} - r)/\delta_{\nu,out}$ for the inner and outer wall respectively. $\delta_{\nu,in} = \mu_{w,in}/(\rho_{w,in}u_{\tau,in})$ and $\delta_{\nu,out} = \mu_{w,out}/(\rho_{w,out}u_{\tau,out})$ and $u_{\tau,in}$ and $u_{\tau,out}$ are the friction velocities at the inner and outer wall, respectively. The largest mean variation of the thermophysical properties can be found near the hot inner wall for $y^+ < 20$. The mean variation is much smaller near the outer wall than it is near the inner wall. Figure 4.4 shows the root mean square values of the density and the thermal diffusivity near the inner wall (left) and the outer wall (right). The relative fluctuations of the thermal diffusivity are larger than those

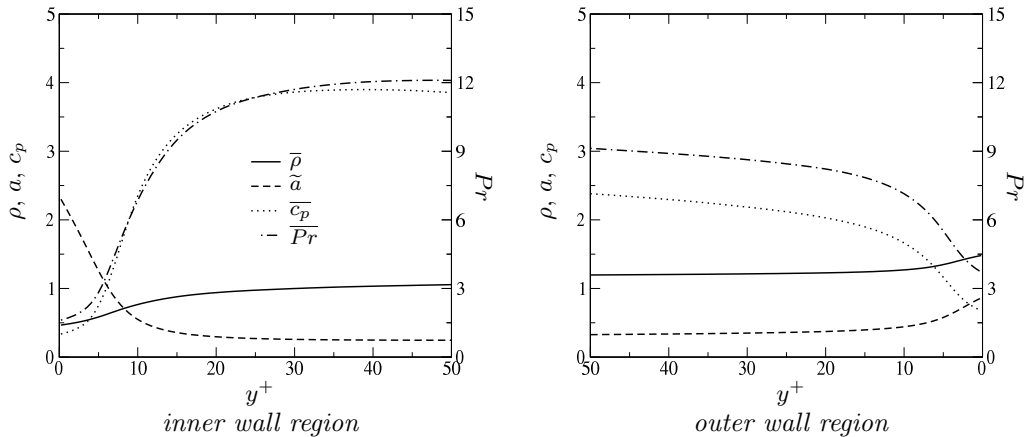


Figure 4.3: Mean profiles of the density, thermal diffusivity, specific heat capacity and molecular Prandtl number near the inner wall (left) and the outer wall (right) in the forced convection sCO₂ case (II).

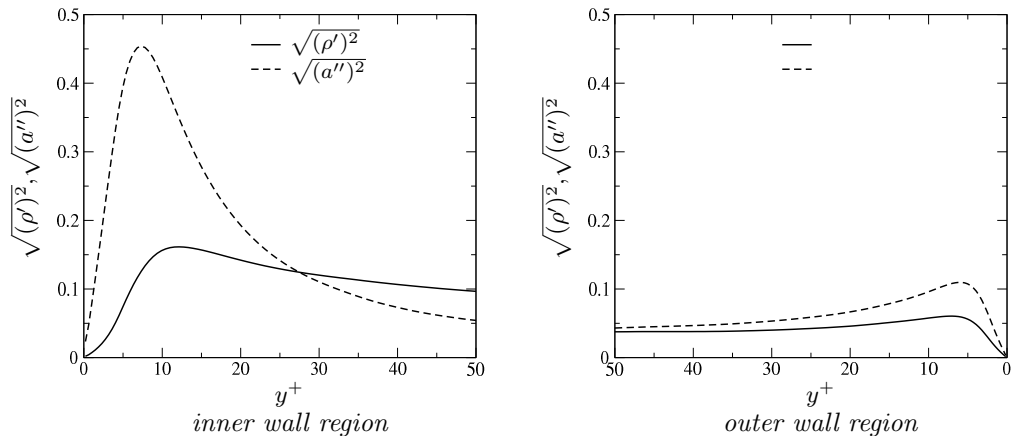


Figure 4.4: Root mean square values of the density and the thermal diffusivity near the inner wall (left) and the outer wall (right) in the forced convection sCO₂ case (II).

of the density. Relatively, the largest value of $a_{rms}/\tilde{a} \approx 80\%$, while the largest value of $\rho_{rms}/\bar{\rho} \approx 20\%$. The $\widetilde{(\dots)}$ denotes a Favre-averaged quantity, while $\overline{(\dots)}$ denotes a Reynolds averaged quantity. The results of the thermophysical property variations of the mixed convection case (III) are qualitatively similar to that of the forced convection case (II); these results are therefore not shown here.

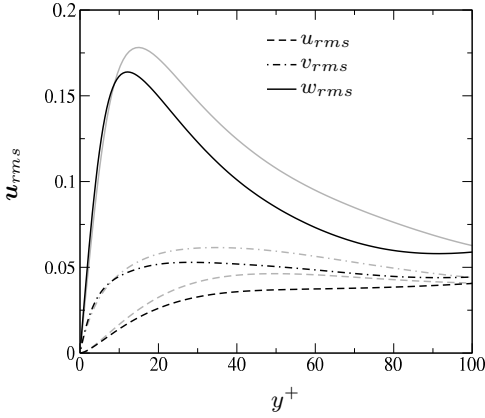
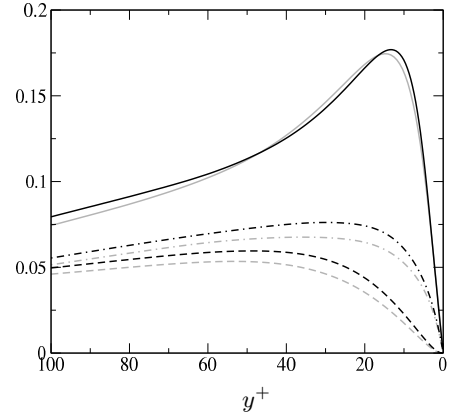
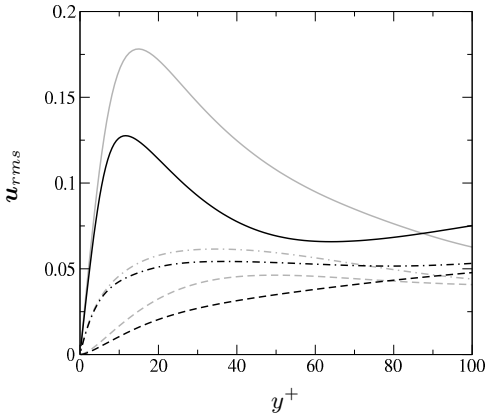
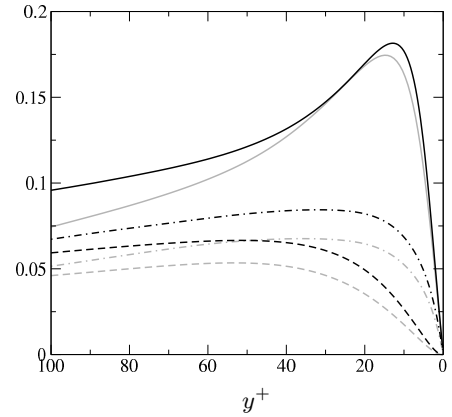
(a) forced sCO₂, inner wall region(b) forced sCO₂, outer wall region(c) mixed sCO₂, inner wall region(d) mixed sCO₂, outer wall region

Figure 4.5: Root mean square values of the velocity fluctuations in the forced convection sCO₂ and the mixed convection sCO₂ cases. The grey lines indicate rms values of the velocity fluctuations of the reference case.

The root mean square values of the velocity fluctuations, $\mathbf{u}'' = \mathbf{u} - \tilde{\mathbf{u}}$, of the wall normal, circumferential and streamwise motions, denoted as u_{rms} , v_{rms} , w_{rms} , respectively, for the forced convection case (II) and the mixed convection case (III), are shown in figure 4.5. Near the inner wall, the magnitude of the turbulent intensities is clearly smaller in the forced convection sCO₂ case (II) than it is in the reference case (I) for $y^+ > 7$. Near the outer wall, only u_{rms} and v_{rms} are larger in the forced convection sCO₂ case (II), but

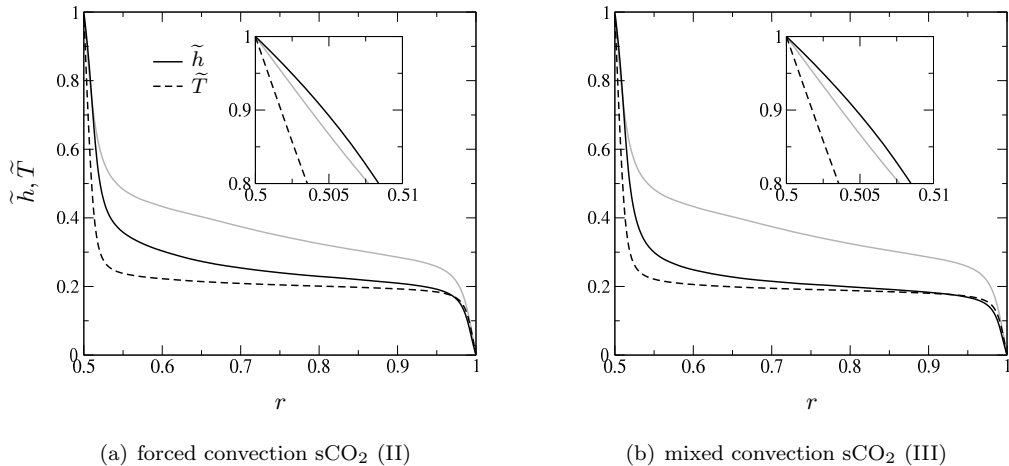


Figure 4.6: Mean profiles of the enthalpy and the temperature in the forced convection sCO₂ and the mixed convection sCO₂ cases. The grey lines indicate results of the reference case, where $\bar{h} = \bar{T}$.

for all y^+ ; w_{rms} is near the outer wall in the forced convection sCO₂ very similar to that of the reference case. The magnitudes of w_{rms} and u_{rms} near the inner wall in the mixed convection sCO₂ case (III) are smaller than they are in the forced convection sCO₂ case (II). The magnitude of v_{rms} in the mixed convection case (III) is very similar to that of the forced convection case (II). The magnitude of the turbulent intensities near the outer wall in the mixed convection sCO₂ case are all larger than the magnitudes of the intensities in the reference case (I). These results show that the turbulent motions are affected by the variable properties in both sCO₂ cases, which can be traced to variable thermophysical property effects on the near wall self regenerating cycle between streaks and quasi streamwise vortices. The observation that the momentum intensities are attenuated near the hot wall and enhanced near the outer wall will be referred to later, when investigating heat transfer characteristics.

4.3.2 Mean thermal statistics

In the previous section, we discussed that the thermophysical properties ρ , c_p , a and Pr show large mean and instantaneous variations near the hot inner wall of the annulus. In this section, we will investigate how these variations affect the mean profiles, as well as the fluctuations of the enthalpy and the temperature.

The mean enthalpy and temperature profiles for the forced convection case sCO₂ (II)

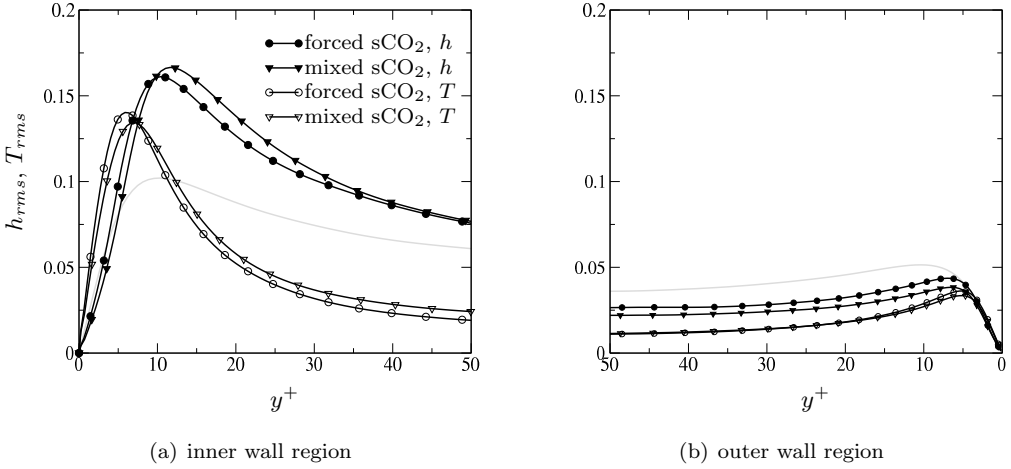


Figure 4.7: Root mean square values of the enthalpy in the forced convection sCO₂ and the mixed convection sCO₂ cases. The grey lines indicate rms values of the enthalpy in the reference case, $h_{rms} = T_{rms}$.

and the mixed convection sCO₂ case (III) are shown in figure 4.6a and 4.6b, respectively. The mean enthalpy values are lower for sCO₂ cases (II and III) than they are for the reference case (I), which shows that heat transfer is affected by the thermophysical property variations. This is more clear in the mixed convection sCO₂ case (III) than it is in the forced convection sCO₂ case (II). The lower values of the mean enthalpy profile in the bulk region of the sCO₂ case indicates that less heat from the wall is transported to the bulk region of the flow. This will be addressed further in section 4.4.1. Very close to the inner wall, however (see the inset of figures 4.6a and 4.6b), the mean enthalpy values are slightly larger in the forced convection sCO₂ case than they are in the reference case.

The mean temperature values are smaller than the mean enthalpy values, which is the result of the large values of the mean specific heat capacity. Both the temperature and the enthalpy were non-dimensionalised such, that their values are equal to unity at the hot inner wall. Since $\partial_r T = \partial_r h / c_p$, the magnitude of the temperature must be smaller than the magnitude of the enthalpy for increasing radial distance r , as c_p is larger than unity for $y^+ > 6$.

Large differences are also observed in the root mean square values of the enthalpy and the temperature fluctuations, $h'' = h - \tilde{h}$ and $T' = T - \bar{T}$. h_{rms} and T_{rms} are shown in figures 4.7(a) and 4.7(b) for the inner and outer wall regions, respectively. The enthalpy fluctuations are larger in the sCO₂ case than they are in the reference case (I)

for $y^+ > 5$; this is typical of flows with high Prandtl numbers, see for instance Kawamura et al. [1998]. The region where h_{rms} is larger in the sCO₂ case than it is in the reference case coincides with the region where \overline{Pr} is larger in the sCO₂ case than it is in the reference case. Due to the non-dimensionalisation of the temperature and the enthalpy, as well as the constant specific heat capacity, $T_{rms} = h_{rms}$ in the reference case (I). This does not hold for the sCO₂ cases. Near the inner wall, in both sCO₂ cases (II and III), see figure 4.7(a) and figure 4.7(b), the magnitude of h_{rms} is much larger than that of the reference case. The magnitude of T_{rms} in the sCO₂ case is larger than that of h_{rms} for $y^+ < 7.1$, but smaller for $y^+ > 7.1$ in the forced convection sCO₂ case (II). The mixed convection sCO₂ case (III) shows a similar trend. This is logical as large values of the specific heat capacity will dampen temperature fluctuations. Looking back at figure 4.3a, $c_p < 1.0$ for $y^+ < 6.0$. Near the outer wall, the magnitude of T_{rms} is much smaller than that of the enthalpy as well for the sCO₂ cases for $y^+ > 4.7$, which is consistent with the fact that near the outer wall, $c_p < 1.0$ only for $y^+ < 4.0$. These findings indicate that a high average specific heat capacity dampens the magnitude of T_{rms} .

However, the previous analysis does not show how instantaneous changes in temperature are related to changes in the enthalpy and changes in specific heat capacity. To investigate the relation between the instantaneous changes of the temperature and the enthalpy, probability distribution functions of the enthalpy fluctuations and the temperature fluctuations can be compared. Figures 4.8(a) and 4.8(b) show probability density functions of the enthalpy and temperature fluctuations near the inner wall at $y^+ = 5$ and $y^+ = 10$, respectively. At these locations, the average temperature is higher than the pseudo-critical temperature, which means that when the enthalpy of a fluid particle increases, the specific heat capacity decreases. Vice versa, when the enthalpy decreases, the specific heat capacity increases. This means that for increasing enthalpy, the temperature increases faster due to the decrease of the specific heat capacity. This suggests that positive extreme temperature fluctuations are more likely to occur than negative extreme temperature fluctuations. This is clearly the case at $y^+ = 5$; $T' > 2T_{rms}$ has a much higher probability than $h'' > 2h_{rms}$ and $T' < 3T_{rms}$ has a much lower probability than $h' < 3h_{rms}$. At $y^+ = 10$ the differences between the probability density distribution between the enthalpy fluctuations and the temperature fluctuations are even more apparent; $T' < T_{rms}$ fluctuations are extremely unlikely, when compared to $h'' < h_{rms}$ fluctuations, while $T' > 2T_{rms}$ values are much more likely to occur than $h' > 2h_{rms}$.

Figures 4.8(c) and 4.8(d) show the probability density functions of the enthalpy and temperature fluctuations in the mixed convection sCO₂ case (III), also at a wall distance of $y^+ = 5$ and $y^+ = 10$, respectively. The probability density functions are broader in the mixed convection sCO₂ case. This may be the result of y^+ not being the same wall distance in the mixed convection sCO₂ case (III) as it is in the forced convection

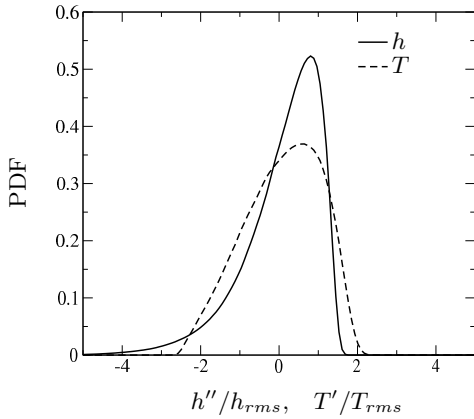
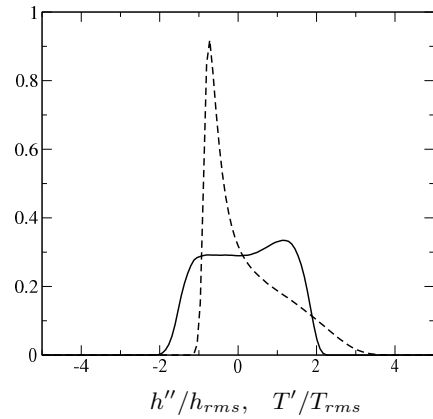
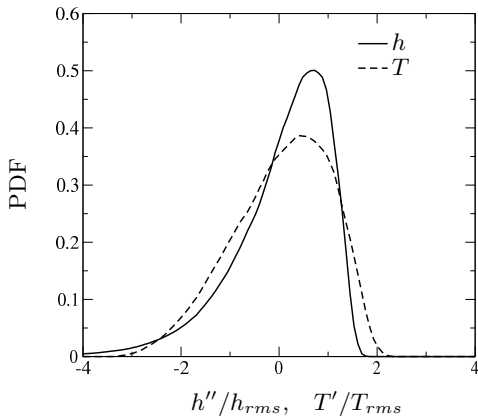
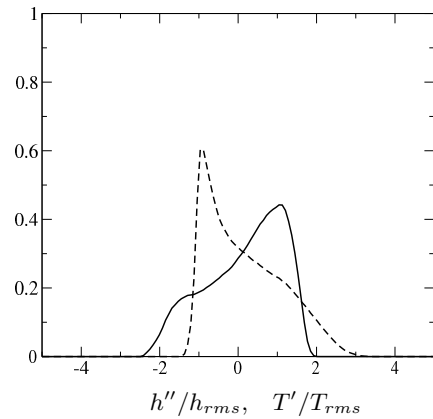
(a) forced convection sCO₂ case (II), $y^+ = 5$ (b) forced convection sCO₂ case (II), $y^+ = 10$ (c) mixed convection sCO₂ case (III), $y^+ = 5$ (d) mixed convection sCO₂ case (III), $y^+ = 10$

Figure 4.8: Probability density functions of the enthalpy and the temperature in the forced convection sCO₂ case (II).

case sCO₂ (II) case. Alternatively, this suggests that extreme enthalpy or temperature fluctuations are more likely in the mixed convection case than they are in the forced convection case. This can be observed for large negative fluctuations of the enthalpy or the temperature when comparing figures 4.8(c) and 4.8(d) with figures 4.8(a) and 4.8(b), respectively. This is most clear for $h''/h_{rms} < 2$ when comparing figure 4.8(d) with figure 4.8(b).

4.3.3 Heat fluxes

In the previous section it was shown that the mean enthalpy has a lower magnitude in the sCO₂ cases than it has in the reference case. We will investigate this further by looking at the heat fluxes that are present. The total heat flux q^{tot} can be written as a sum of three terms.

$$q^{tot} = \widetilde{\rho a} d_r \widetilde{h} + \widetilde{\rho a''} \partial_r \widetilde{h''} - Re_b Pr_h \widetilde{\rho u''} \widetilde{h''}, \quad (4.2)$$

where d_r is the derivative with respect to the radial direction, ∂_r the partial derivative with respect to the same direction. The first term in equation (4.2) represents conduction, the second term a correlation between thermal diffusivity fluctuations and enthalpy gradient fluctuations, which we will refer to as *turbulent conduction*, and the last term represents the turbulent heat flux. The total heat flux can be expressed as $q^{tot} = q_{w,in} R_{in}/r$, where $q_{w,in} = \widetilde{\rho a} d_r \widetilde{h}|_{r=R_{in}}$. Note that the quantity $\widetilde{\rho a}$ can qualitatively be thought of as the average thermal conductivity divided by the average specific heat capacity. The radial profiles of these fluxes are shown in figures 4.9(a) and 4.9(b) in the near inner and outer wall region, respectively, for the forced convection sCO₂ case.

It is clear that the total heat flux and the turbulent heat flux are smaller in the forced convection sCO₂ case, which means that less heat is transported from the hot wall to the cold wall. Molecular conduction near the inner wall shows two distinct differences when compared to the reference case (I). Firstly, at the inner wall it is smaller than it is in the

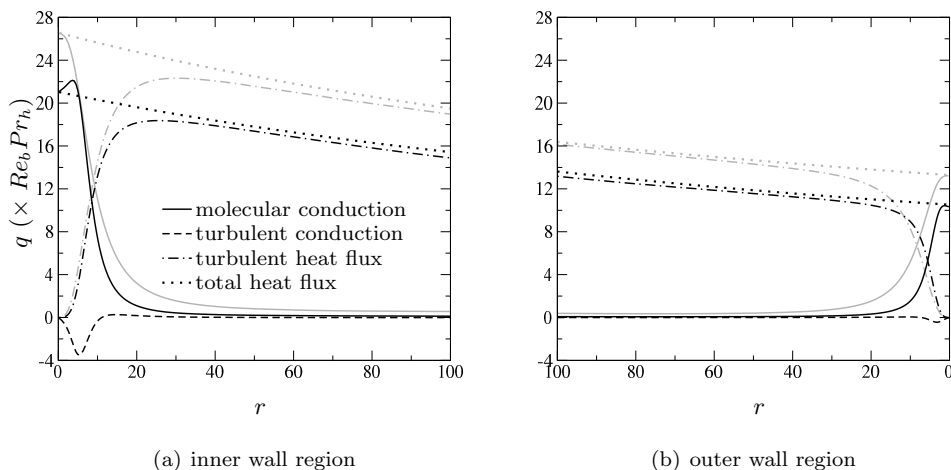


Figure 4.9: Heat fluxes in the forced convection sCO₂ case (II) and the reference case (I). Grey lines indicate results of the reference case.

reference case (I), but secondly it increases in magnitude for increasing wall distance up to $y^+ < 4$. This increase in magnitude must be the result of a relative increase in the mean enthalpy gradient, as the thermal diffusivity decreases with increasing wall distance, near the inner wall. This is in agreement with the results presented in figure 4.6(a). At $y^+ = 5$, the magnitude of molecular conduction is similar between the forced convection sCO₂ case (II) and the reference case (I). For $y^+ > 5$, molecular conduction becomes smaller again in the forced convection sCO₂ case; this can be attributed to the low values of $\bar{\rho}\tilde{a}$. Near the outer wall, molecular conduction is smaller in the forced convection sCO₂ case than it is in the reference case for all y^+ .

The heat flux by turbulent conduction is negative both near the inner wall and the outer wall, which means that, on average, it results in transport of relatively hot fluid from the bulk region towards the hot wall and relatively cold fluid from the bulk region towards the cold wall. The reason that the heat flux by turbulent conduction is negative at both walls can be explained as follows: near the inner wall, as a fluid particle heats up, the thermal diffusivity will increase as well, while near the outer wall, as a fluid particle cools down, the thermal diffusivity will decrease as well.

The fact that the turbulent heat flux is smaller in the sCO₂ forced convection case (II) than it is in the reference case (I) can be partially attributed to the low density region near the inner wall in the sCO₂ forced convection case (II). However, the correlation $\widetilde{u''h''}$ changes as well. Figure 4.10(a), shows that $\widetilde{u''h''}$ is altered by the thermophysical properties of sCO₂, as well as the mixed convection condition, near the inner wall of the annulus. For $y^+ < 15$, $\widetilde{u''h''}$ is larger in the forced convection sCO₂ case (II) than it is in the reference case (I); for $y^+ > 15$, the opposite is true. $\widetilde{u''h''}$ is smaller for all y^+ in the mixed convection case (III), when compared to $\widetilde{u''h''}$ in the forced convection sCO₂ case (II), although it is almost equal to $\widetilde{u''h''}$ in the reference case up to $y^+ = 10$. Even though the wall normal velocity fluctuations are attenuated, the enthalpy fluctuations are enhanced for $y^+ > 5$, which was already shown in section 4.3.2. Therefore, opposing effects are here at play; the high average Prandtl number leads to large enthalpy fluctuations, but the density and dynamic viscosity variations attenuate the wall normal velocity.

Although of lesser importance to the current configuration, it is also interesting to investigate the streamwise turbulent heat flux $\bar{\rho}\widetilde{w''h''}$, which is an important quantity in configurations with thermal developing boundary layers. Near the hot wall, the correlation $\widetilde{w''h''}$ can be physically interpreted to represent near wall streaks (low speed regions, $w'' < 0$) that have a relatively high enthalpy ($h'' > 0$). Figure 4.10(b) shows $\widetilde{w''h''}$ near the inner wall. $\widetilde{w''h''}$ has a larger magnitude in the forced convection sCO₂ case (II) than it has in the reference case (I). This is again the result of the larger Prandtl number, as this leads to higher enthalpy fluctuations close to the inner wall, while w_{rms} is smaller in

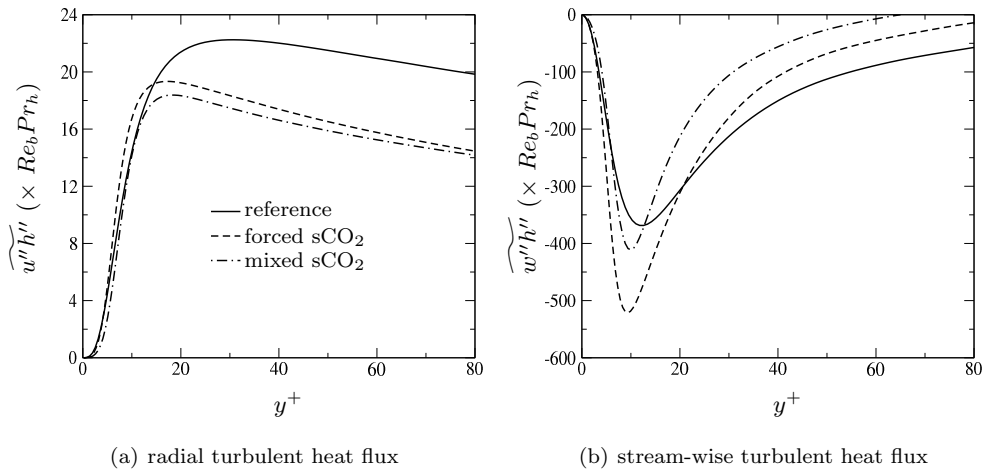


Figure 4.10: $\overline{u''h''}$ and $\overline{w''h''}$ near the inner wall in the reference case (I), the forced convection case (II) and the mixed convection case (III). Grey lines indicate values of the reference case.

the sCO₂ cases, near the inner wall. The streamwise turbulent heat flux is smaller in the mixed convection sCO₂ case (II) than in the forced convection sCO₂ case (III), which can be attributed to the attenuated streamwise velocity fluctuations, which were shown in figure 4.5. Thus, the same opposing effects of turbulence attenuation and enthalpy fluctuation enhancement as before with the radial turbulent heat flux are here at play.

4.3.4 Turbulent heat flux transport equation

To investigate the differences in $\overline{u''h''}$ and $\overline{w''h''}$ further, the transport equation of the turbulent heat flux can be analysed. The transport equation of the radial turbulent heat flux can be written as:

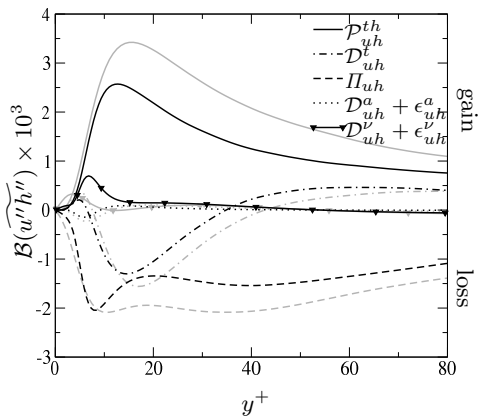
$$\begin{aligned}
 \bar{\rho} D_t \overline{u''h''} &= \underbrace{Re^{-1} \overline{(\nabla \cdot 2\rho\nu h'' \mathbf{S})}_r}_{\mathcal{D}_{uh}^\nu} - \underbrace{Re^{-1} \overline{(2\rho\nu \mathbf{S}^T \cdot \nabla h'')}_r}_{\epsilon_{uh}^\nu} \\
 &+ \underbrace{(Re_b Pr_h)^{-1} \overline{\nabla \cdot \rho a u'' \nabla h}}_{\mathcal{D}_{uh}^a} - \underbrace{(Re_b Pr_h)^{-1} \overline{\rho a (\nabla u'' \cdot \nabla h'')}}_{\epsilon_{uh}^a} \quad (4.3) \\
 &- \underbrace{r^{-1} d_r (\overline{r \bar{\rho} u'' u'' h''}) + r^{-1} \overline{\bar{\rho} v''^2 h''}}_{\mathcal{D}_{uh}^t} - \underbrace{\overline{\bar{\rho} u''^2 d_r \tilde{h}}}_{\mathcal{P}_{uh}^{th}} - \underbrace{\overline{h'' \partial_r p}}_{\Pi_{uh}},
 \end{aligned}$$

in which D_t represents the material derivative, $\mathbf{S} = 1/2(\nabla \mathbf{U} + (\nabla \mathbf{U})^T) - 1/3(\nabla \cdot \mathbf{u})\mathbf{I}$, \mathcal{D}_{uh}^t

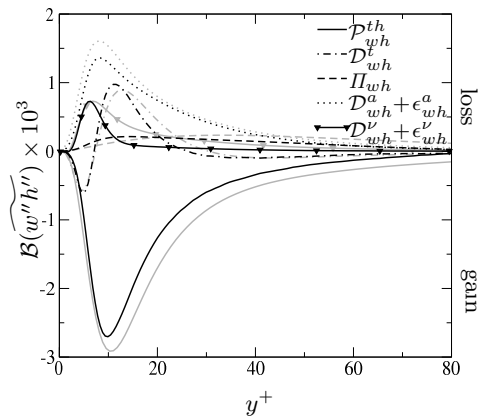
represents the turbulent mixing, \mathcal{P}_{uh}^{th} thermal production and Π_{uh} pressure scrambling. The dissipation and diffusion terms consist of a viscous part and thermal part. For the dissipation, these terms are ϵ_{uh}^ν and a thermal part ϵ_{uh}^a and for diffusion these are \mathcal{D}_{uh}^ν and a \mathcal{D}_{uh}^a . Note that \mathcal{D}_{uh}^a , ϵ_{uh}^ν , \mathcal{D}_{uh}^a and ϵ_{uh}^ν can be further decomposed, using $a = \tilde{a} + a''$ and $\tilde{\nu} + \nu''$. However, this is not done here, as the fluctuating thermophysical properties parts of these terms are small. An equivalent transport equation can be derived for $\widetilde{w''h''}$, the terms of which will be denoted as $(\dots)_{wh}$. The budgets of equation (4.3) will be denoted with $\mathcal{B}(\widetilde{w''h''})$.

Figures 4.11(a) and 4.11(c) show that the thermal production \mathcal{P}_{uh}^{th} is smaller in the sCO₂ cases than it is in the reference case (I); this is the result of the decreased velocity fluctuations in the wall-normal direction. The turbulent mixing term and the pressure scrambling term Π_{uh} are smaller as well. Comparing figures 4.11(a) and 4.11(c), reveals that the pressure scrambling term in the forced convection case is only marginally different from that in the mixed convection case. Π_{uh} can be shown to consist of four different contributions: a return-to-isotropy term, a rapid part, a buoyancy contribution and a wall-reflection term, see for instance Dol et al. [1999]. In other words, buoyancy has no direct influence on the radial turbulent heat flux. There is, however, an increase in the contribution of the viscous parts of the diffusion and dissipation terms; we will investigate this below.

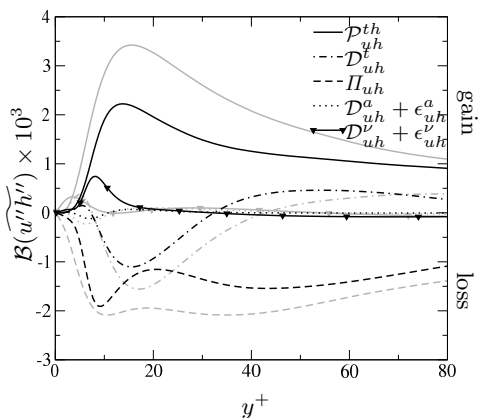
The thermal part of the streamwise turbulent heat flux production, \mathcal{P}_{wh}^{th} , is smaller in the forced convection sCO₂ case (II) than it is in the reference case (I), as can be seen in figure 4.11(b). For $y^+ < 10$, the thermal diffusivity and dissipation contribution, which acts as a sink, is smaller in the forced convection sCO₂ case, which is the result of the low values of $\tilde{\rho}\tilde{a}$ near the inner wall. The contributions of the viscous parts of the diffusivity and dissipation are substantially smaller as well for $y^+ > 10$, which is the result of turbulence attenuation due the variation of the density and the dynamic viscosity. It follows that this analysis does not yield any more insight into the production of $\widetilde{w''h''}$ than our analysis in section 4.3.3. However, comparing the budgets of the mixed convection sCO₂ case, figure 4.11(b), with those of the forced convection sCO₂ case, figure 4.11(d), shows that the pressure scrambling term is notably larger in the mixed convection sCO₂ case (III) than it is in the forced convection sCO₂ case. Thus, buoyancy influences the streamwise turbulent heat flux directly and it has a negative effect on $\widetilde{w''h''}$ near the inner wall. This is intuitive as near wall streaks (low speed regions) tend to have a relatively high enthalpy and therefore have a relatively low density. Similarly, a high speed region will have a relatively low enthalpy and therefore have a high density. Peeters et al. [2016] reasoned that, if the flow direction and the gravitational acceleration point in opposite direction, buoyancy will hamper the formation of streaks. Buoyancy therefore acts as a sink to the correlation $\widetilde{w''h''}$ through the pressure scrambling term.



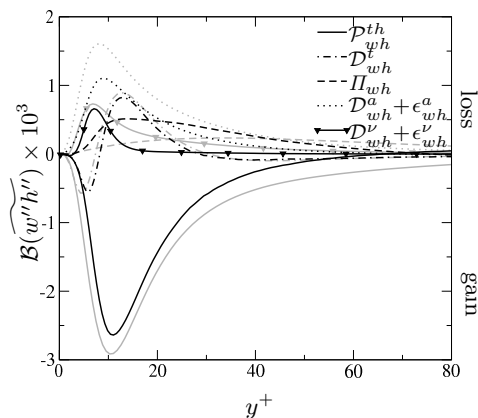
(a) $\mathcal{B}(\widetilde{u''h''})$ in the forced convection sCO₂ case (II)



(b) $\mathcal{B}(\widetilde{w''h''})$ in the forced convection sCO₂ case (II)



(c) $\mathcal{B}(\widetilde{u''h''})$ in the mixed convection sCO₂ case (III)



(d) $\mathcal{B}(\widetilde{w''h''})$ in the mixed convection sCO₂ case (III)

Figure 4.11: Budgets of the turbulent heat flux transport equation in the forced (top figures) and mixed convection sCO₂ cases (bottom figures).

We observed before that the contribution of the viscous parts of the diffusion and dissipation terms of $\mathcal{B}(\widetilde{u''h''})$ are increased in the sCO₂ cases. Figure 4.12 shows the viscous parts of the diffusion and dissipation terms separately for the forced convection case (II). The diffusion term in the forced convection case has shifted away from the wall, when compared to the same term in the reference case. The dissipation term is larger

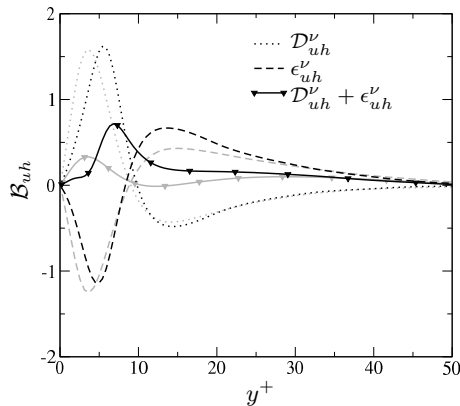


Figure 4.12: Viscous parts of the diffusion and dissipation terms of the radial turbulent heat flux for reference case (I) and the forced convection $s\text{CO}_2$ case. The results of the reference case (I) are in grey.

in the forced convection case. The increase of the dissipation term is most clear in the region $y^+ = 10 - 30$. This coincides with the region where $\overline{Pr} > 9$, see figure 4.3(a), which leads to larger enthalpy fluctuations in the same region, which was already shown in figure 4.7(a). The strong correlation between the velocity gradients and the gradient of the enthalpy fluctuations is associated with the near wall turbulent structures, such as quasi-streamwise vortices, streaks and internal shear layers, which was shown by Abe et al. [2009]. The dissipation of the turbulent heat flux is therefore increased as a result of larger instantaneous enthalpy gradients across the near wall turbulent structures.

4.4 Nusselt relation

4.4.1 Influences of the heat fluxes on the Nusselt number

By comparing Nusselt numbers for the hot and cold wall of the different cases, we can determine if the local variations in thermophysical properties cause heat transfer enhancement, or heat transfer deterioration. We will first define two separate Nusselt numbers for the hot and cold wall respectively, after which we will introduce a relation between the Nusselt number and the heat fluxes as they were defined in section 4.3.3. The latter will allow us to connect previous observations to changes in the Nusselt number due to variable thermophysical properties directly.

Since heating occurs at the inner wall and cooling occurs at the outer wall, we will

divide the annulus into a hot side and a cold side. This will allow us to compare the effectiveness of heat transfer at both walls separately. To distinguish between the hot side and the cold side, we will choose the location where $\partial_r \tilde{w} = 0$, denoted as $r = R_a$, to be the boundary between the hot side and the cold side. We can now define a Nusselt number for both the hot wall and the cold wall;

$$Nu_h = \frac{q_w^o D_h^o}{k_{pc}^o (T_h^o - T_{b,h}^o)} \quad \text{and} \quad Nu_c = \frac{q_w^o D_h^o}{k_{pc}^o (T_c^o - T_{b,c}^o)}, \quad (4.4)$$

where $T_{b,h}$ is the bulk temperature on the hot side and $T_{b,c}$ is the bulk temperature on the cold side. $T_{b,h}$ and $T_{b,c}$ are functions of $h_{b,h}$ and $h_{b,c}$, respectively, which in turn are defined as;

$$h_{b,h} = \frac{\int_{R_{in}}^{R_a} \rho w h r dr}{\int_{R_{in}}^{R_a} \rho w r dr} \quad \text{and} \quad h_{b,c} = \frac{\int_{R_a}^{R_{in}} \rho w h r dr}{\int_{R_a}^{R_{in}} \rho w r dr}, \quad (4.5)$$

respectively. R_a denotes the radial location where the shear stress is equal to zero. Fukugata et al. [2005] showed that a relation between the Nusselt number and the heat fluxes can be derived for heated turbulent channel flows. A similar relation may be derived for the hot and cold Nusselt numbers. For the sake of readability, these derivations can be found in the appendix. The relation between the hot Nusselt number and the heat fluxes can be written as:

$$Nu_h = \Gamma_h \Theta_h \left\{ \underbrace{\int_{R_{in}}^{R_a} \tilde{\rho} a \tilde{r} \tilde{h} dr}_{\text{molecular conduction}} + \underbrace{\int_{R_{in}}^{R_a} \tilde{\rho} a'' \tilde{\partial}_r h'' dr}_{\text{turbulent conduction}} - \underbrace{Re_b Pr_h \int_{R_{in}}^{R_a} \tilde{\rho} u'' \tilde{h}'' dr}_{\text{turbulent heat flux}} \right\} \quad (4.6)$$

In this relation, the factors Γ_h and Θ_h represent a shape factor $(1/R_{in})/\ln(R_{in}/R_a)$ and the temperature difference ratio $(T_h - T_i)/(T_h - T_b)$. The relation for the cold Nusselt number Nu_c , is simply obtained by setting R_{in} to R_{out} , Γ_h to $\Gamma_c = (1/R_{out})/\ln(R_a/R_{out})$ and Θ_h to $\Theta_c = (T_h - T_i)/(T_b - T_c)$. For the reference case, ρ and a are equal to unity, which may be used to reduce equation (4.6) to:

$$Nu_h = \Gamma_h \Theta_h \left\{ \underbrace{\tilde{h}(R_a) - \tilde{h}(R_{in})}_{\text{molecular conduction}} - \underbrace{Re_b Pr_h \int_{R_{in}}^{R_a} u'' \tilde{h}'' dr}_{\text{turbulent heat flux}} \right\}. \quad (4.7)$$

Equations (4.6) and (4.7) are useful to determine the contribution of the different heat fluxes to the Nusselt number. These contributions are listed in table 4.2 for the hot wall and in table 4.3 for the cold wall, for all cases. In the reference case, the Nusselt number at the cold wall is slightly larger than the Nusselt number at the hot wall. Intuitively, this is logical as turbulence intensities near the outer wall are slightly larger than turbulence intensities near the inner wall in the reference case (I). The hot Nusselt number is smaller in the $s\text{CO}_2$ cases, while the cold Nusselt number is larger. At the hot side, this means

that less heat is transported from the hot wall to the bulk region of the flow in the sCO₂ cases (II and III) when compared to the reference case (I), which results in a larger difference between $T_{w,h}$ and $T_{b,h}$ as was already clear from figure 4.6. At the cold side, the increase in the cold Nusselt number indicates that more heat is transported towards the cold wall, which results in a smaller difference $T_{w,c}$ and $T_{b,c}$, which is also visible in figure 4.6.

Qualitatively, the differences between the Nusselt numbers between the sCO₂ cases and the reference case (I), are in agreement with our earlier observations that the turbulent intensities have decreased in the sCO₂ cases near the inner wall (see figure 4.5(a) and 4.5(c)), but increased near the outer wall (see figure 4.5(b) and 4.5(d)). However, this does not mean that the other thermophysical properties, such as the density, thermal diffusivity and molecular Prandtl number have no effect, as was discussed in the previous sections 4.3.3 and 4.3.4. Furthermore, it is also clear that the mixed convection conditions only have a small negative effect on the hot Nusselt number, but an appreciably large positive effect on the cold Nusselt number. In the mixed convection sCO₂ case (III), the contribution of the turbulent heat flux to the hot Nusselt number has decreased. However, this decrease is opposed by an increase in the molecular conduction contribution, which can only be the result of an increase of the mean enthalpy gradient (with respect to the radial distance), since the product $\tilde{\rho}\tilde{a}$ (which occurs in the first term of equation (4.6)) is smaller than unity for $y^+ > 5$. The contribution of the heat flux by turbulent conduction is negligible in all cases, both to the Nusselt number at the hot wall and that at the cold wall. Finally, the results presented in this section show that heat transfer deterioration or enhancement can occur without mean streamwise acceleration or mixed convection conditions.

Table 4.2: Contributions to the Nusselt number at the hot inner wall.

| Case | Nu_h | molecular conduction | turbulent conduction | turbulent convection |
|-------------------------|--------|-------------------------|-------------------------|-------------------------|
| reference | 41.7 | 5.7 | - | 36.0 |
| forced sCO ₂ | 26.4 | 3.9 | -0.3 | 22.8 |
| mixed sCO ₂ | 26.2 | 5.3 | -0.5 | 21.4 |

Table 4.3: Contributions to the Nusselt number at the cold outer wall.

| Case | Nu_c | molecular conduction | turbulent conduction | turbulent convection |
|-------------------------|--------|-------------------------|-------------------------|-------------------------|
| reference | 44.9 | 3.6 | - | 41.3 |
| forced sCO ₂ | 52.5 | 2.3 | 0.0 | 50.2 |
| mixed sCO ₂ | 56.5 | 2.3 | 0.0 | 54.2 |

4.4.2 Heat flux events and characteristics

The previous section gave insight how the different heat fluxes contribute to the Nusselt number at the hot wall and the cold wall. It was shown that the variable thermophysical properties have a large effect on turbulent heat flux contribution to the Nusselt numbers. Here, we will investigate the contribution of the turbulent heat flux to the Nusselt number further by making a quadrant analysis of the turbulent heat flux. For a comprehensive overview on quadrant analysis, we refer to Wallace [2016]. The turbulent heat flux can be decomposed into four different terms or quadrants, which can be summarised as:

- F₁: $u'' > 0$, $h'' > 0$, hot ejection
- F₂: $u'' > 0$, $h'' < 0$, cold ejection
- F₃: $u'' < 0$, $h'' < 0$, cold sweep
- F₄: $u'' < 0$, $h'' > 0$, hot sweep

Note that for determining $u'' > 0$ or $u'' < 0$, we mean to denote positive or negative radial velocity fluctuations with respect to the wall normal direction. Near the hot wall, the F₁ and F₃ quadrants yield a positive product $u''h''$ and thus, these quadrants have a positive effect on the Nusselt number Nu_{hot} , while the F₂ and F₄ quadrants yield a negative product and thus have a negative effect. Near the cold wall, this is reversed; the F₂ and F₄ events have a positive effect, while the F₁ and F₃ have a negative effect. The turbulent heat flux quadrants can physically be interpreted as follows. Close to the hot inner wall, characteristic 'mushroom'-like enthalpy (or temperature) structures can be observed, as can be seen in the top part of figure 4.2(a) and is shown more

clearly in figure 4.13(a). A schematic of such a structure is shown in figure 4.13(b). The mushroom structure can be regarded as the result of the near wall cycle that exists in near wall bounded turbulence. Low speed regions near the hot inner wall generally have a higher enthalpy than the surrounding fluid; the low speed regions are indicated by the black contours in figure 4.13(a). Such a low speed region grows unstable which results in the ejection of hot fluid (indicated in the figure by F_1). The ejection leads to the formation of quasi-streamwise vortices. These vortices then convect hot fluid towards the wall (indicated in the figure by F_4). These vortices also draw in relatively cold fluid from the bulk region of the flow (indicated by F_3). The inrush of cold fluid is subsequently reflected due to the presence of the wall, which results in relatively cold fluid moving away from the heated wall (indicated by F_2).

We will distinguish between small and large values of the turbulent heat flux, by defining a hole parameter H (which is similar to the approach of Willmarth and Lu [1972] for the Reynolds shear stress):

$$|\rho u'' h''| > H(\overline{\rho u'' h''}) \quad (4.8)$$

The hole parameter H is a real positive number between zero and infinity. For large values of the hole parameter H , $\rho u'' h''$ represents extreme events in turbulent heat transfer, by which we mean large correlations of u'' and h'' . The hole parameter is graphically represented in figure 4.14.

The integral of the radial turbulent heat flux of equation (4.6) can be decomposed into four terms, which represent the different flux quadrants:

$$\int_{R_{in}}^{R_a} \overline{\rho u'' h''} dr = \int_{R_{in}}^{R_a} \left\{ \left(\overline{\rho u'' h''} \right)_{F_1} + \left(\overline{\rho u'' h''} \right)_{F_2} + \left(\overline{\rho u'' h''} \right)_{F_3} + \left(\overline{\rho u'' h''} \right)_{F_4} \right\} dr. \quad (4.9)$$

Equations (4.6), (4.8), (4.9) allow us to determine the contributions of the turbulent heat flux quadrants on the Nusselt number for different values of the hole parameter H . Figures 4.15(a), 4.15(b) show the Nusselt number contributions of the turbulent heat flux quadrants F_1 - F_4 in the forced convection sCO₂ case near the hot wall and the cold wall, for the condition given by equation (4.8). Figures 4.16(a) and 4.16(b) show the same, but then for the mixed convection sCO₂ case. Figure 4.15(a) shows that the positive contributions to Nu_{hot} , F_1 and F_3 , have substantially decreased in the forced convection sCO₂ case, when compared to the same contributions in the reference case (I). For large values of H (> 8), however, the difference between the F_1 and F_3 events is very small; this is especially true for the F_3 contributions. The magnitude of the F_2 contributions has increased in the forced convection sCO₂ case, as has the magnitude of the F_4 contributions for large values of H (> 4). This is surprising, because we have seen before in figure 4.5(a) that the wall normal motions have decreased in magnitude near the

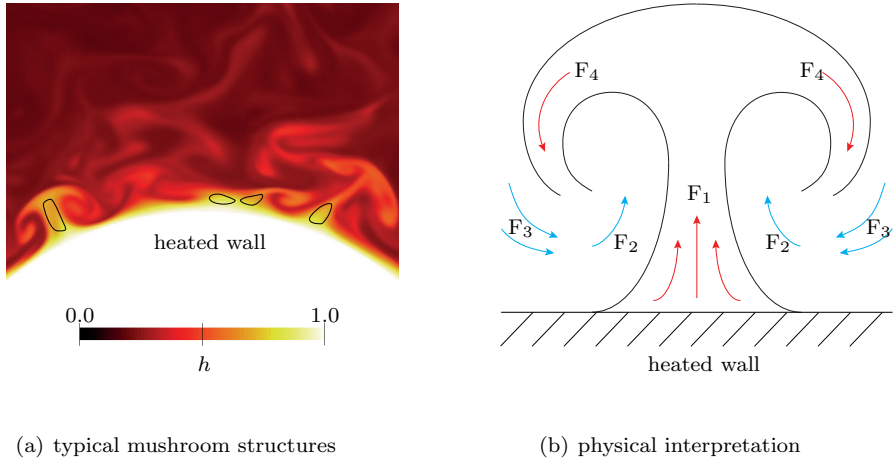


Figure 4.13: Left: typical mushroom structures near the hot wall of the annulus in the forced convection $s\text{CO}_2$ case. The black contour lines denote low speed fluid regions (streaks). Right: a physical interpretation of the the flux quadrants using the mushroom structure as an example.

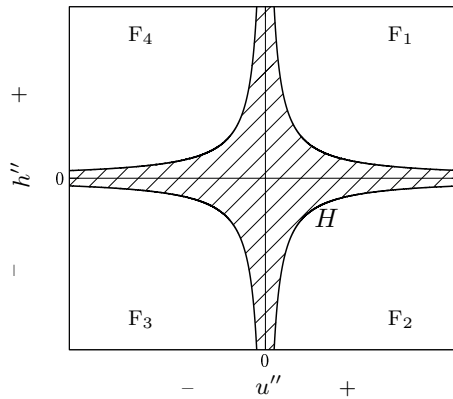


Figure 4.14: Graphic representation of the hole parameter H .

hot wall in the forced convection case (II), when compared to the values of the reference case (I). In other words, based purely on the observation that the magnitude of wall normal fluctuations is smaller in the $s\text{CO}_2$ cases, one would expect that the contribution of all flux quadrants to the Nusselt number should be smaller in the $s\text{CO}_2$ cases as well.

Near the cold outer wall, see figure 4.15(b), all flux quadrant contributions to Nu_{cold} , both negative, F_1 and F_3 , and positive, F_2 and F_4 , have increased in magnitude. This is consistent with the fact that the magnitude of u'' are enhanced near the outer wall in the forced convection case (II) than they are in the reference case (I).

The mixed convection condition (heated, upward flow) near the hot inner wall acts as to decrease the magnitude of all the flux quadrant contributions to Nu_{hot} ; this can be deduced from comparing figures 4.15(a) and 4.16(a). Near the outer wall, however, the mixed convection condition (cooled, upward flow) enhances the magnitude of all flux quadrant contributions to Nu_{cold} . This is consistent with our earlier observations that the magnitude of the wall-normal fluctuations near the hot wall in the mixed convection case (III) is smaller than it is in the forced convection case (II). Similarly, the increase of the flux quadrant contributions to Nu_{cold} is consistent with the increased turbulence near the outer wall.

It has become clear that the turbulent heat flux quadrants near the hot inner wall in the sCO₂ cases show unexpected results that cannot be fully explained by investigating the wall-normal turbulent fluctuations. We will therefore investigate how the attenuated (near the inner wall) or enhanced (near the outer wall) wall normal motions, as well as the variable thermophysical properties affect the instantaneous turbulent heat flux $\rho u'' h''$. Figures 4.17(a) and 4.17(b) show the expected value of the wall normal velocity u'' near the hot inner wall and the cold outer wall (both at $y^+ = 20$). Near the hot inner wall, the magnitude of the wall normal velocity of the forced convection sCO₂ case (II) is clearly attenuated for all the flux quadrants, when compared to that of the reference case (I). The attenuation of the wall normal velocity magnitude of the F_1 quadrant is less than that of the other quadrants. Near the cold outer wall, the magnitude of the wall normal motion of the forced convection sCO₂ case is enhanced, when compared to that of the reference case (I). These findings are consistent with the results for the turbulent intensities, which were shown in figures 4.5(a) and 4.5(b).

The instantaneous density directly influences the magnitude of the turbulent heat flux $\rho u'' h''$. Figures 4.18(a) and 4.18(b) show the expected values of the density, $E(\rho)$, conditioned on the four quadrants of the turbulent heat flux. Near the hot inner wall, the F_1 and F_4 turbulent heat flux quadrants of the forced convection sCO₂ case (II) have a low density compared to the density of the reference case (I), the F_2 and F_3 turbulent heat flux quadrants have a higher density. The density of the F_1 quadrant is generally lower than that of the F_4 quadrant. This can physically be interpreted as follows; the fluid regions that constitute F_1 quadrant are generally hotter than the fluid regions that constitute the F_4 quadrant. Similarly, the density of the F_3 quadrant is higher than the density of F_2 quadrant, which means that fluid regions that constitute the F_3 quadrant are colder than regions that constitute the F_2 quadrant. At the outer wall, see figure

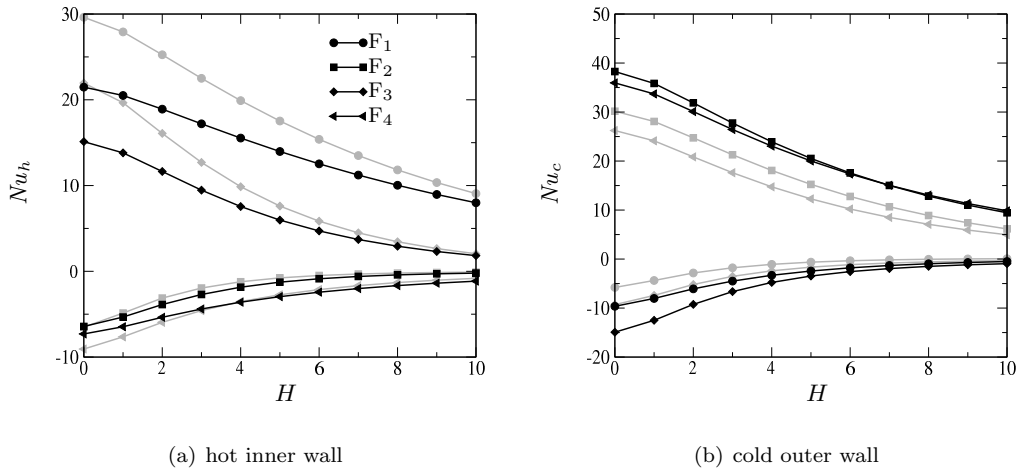


Figure 4.15: Contributions of the turbulent heat flux events as a function of the hole size H in the reference case (I) and the forced convection $s\text{CO}_2$ case (II).

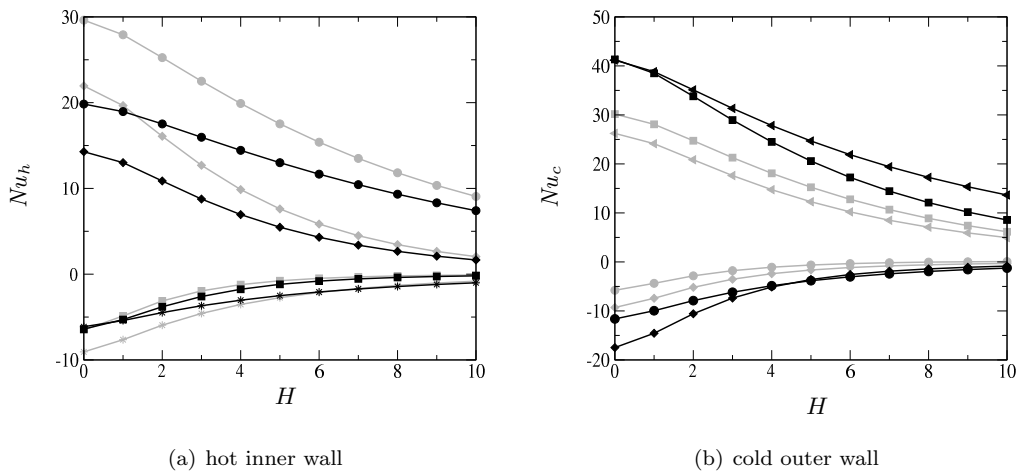


Figure 4.16: Contributions of the turbulent heat flux events as a function of the hole size H in the reference case (I) and the mixed convection $s\text{CO}_2$ case (III).

4.18(b), all turbulent heat flux quadrants in the forced $s\text{CO}_2$ case have a density that is higher than the density in the reference case (I). The conditional averaging analysis shows that different quadrants are affected differently by the density variations. Fluid regions with relatively low density may result in a smaller instantaneous turbulent heat

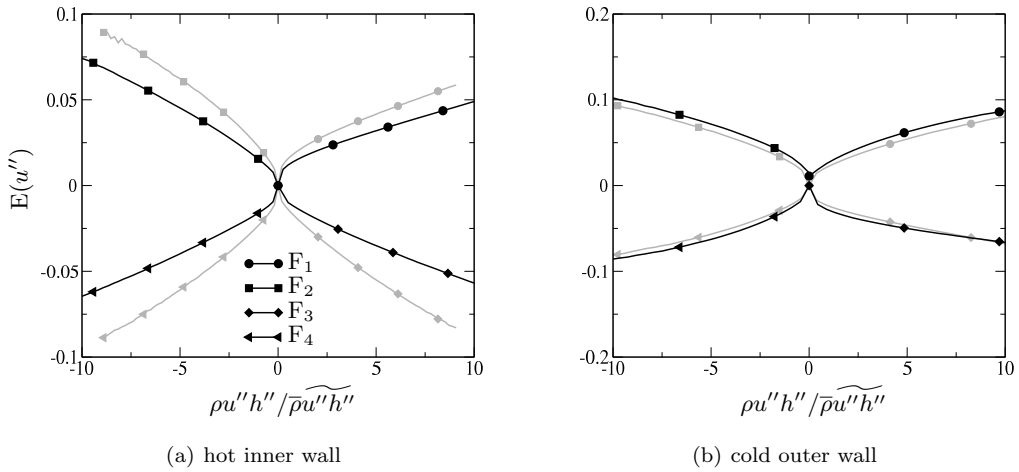


Figure 4.17: Expected value of the wall normal velocity u'' conditioned on all four quadrants of the turbulent heat flux in the forced convection $s\text{CO}_2$ case (II). The constant grey line represents the density in the reference case (I).

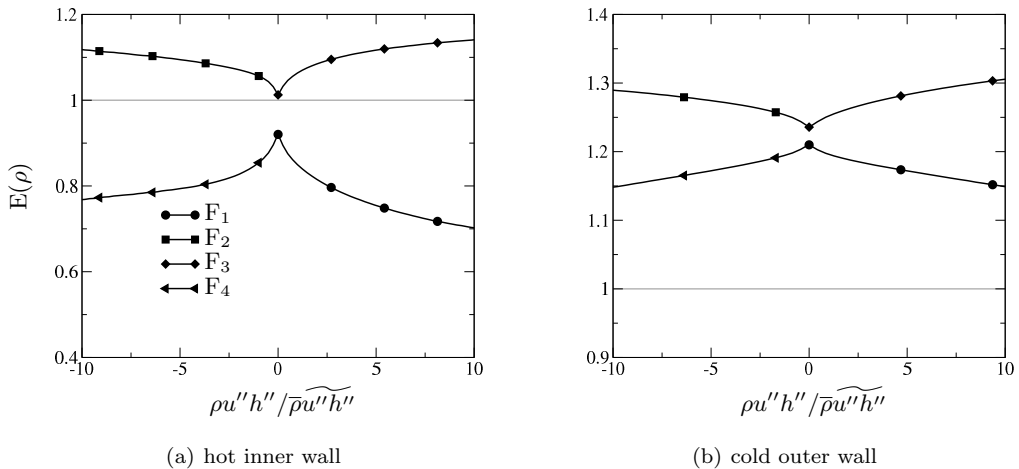


Figure 4.18: Expected value of the density for a given value of the turbulent heat flux in the forced convection $s\text{CO}_2$ case (II). The constant grey line represents the density in the reference case (I).

flux, while regions with a high density may result in a larger instantaneous turbulent heat flux.

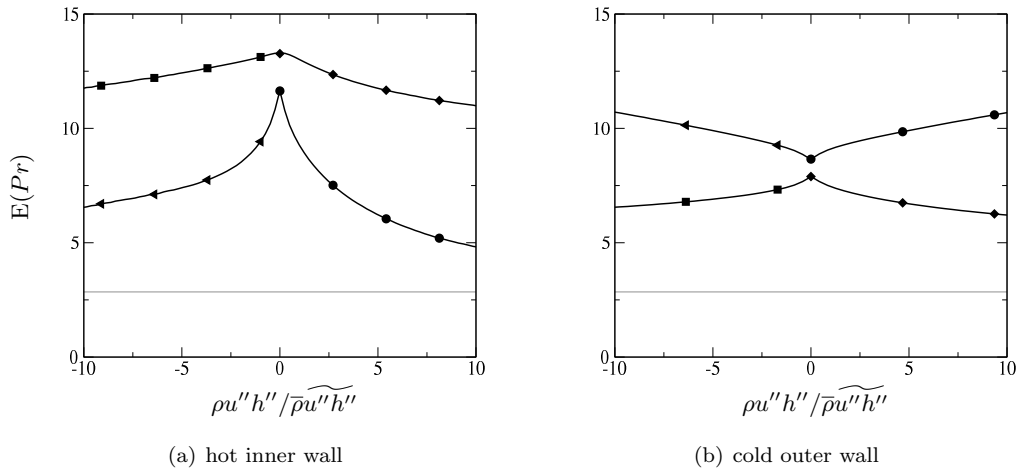


Figure 4.19: Expectancy of the molecular Prandtl number for a given value of the turbulent heat flux in the forced convection sCO₂ case. Legends are the same as in figure 4.18. The constant grey line represents the molecular Prandtl number in the reference case (I). Results are shown for $y^+ = 20$.

Another interesting parameter to investigate is the time-scale ratio, which is defined as:

$$R = \frac{\tau_\theta}{\tau_k} \equiv \frac{\overline{h''^2 \bar{\epsilon}}}{2 \bar{k} \epsilon_\theta} = \left(\frac{\tilde{\nu}}{\tilde{a}} \right) \frac{\overline{h''^2 (2 \mathbf{S}'' : \nabla \mathbf{u}'')}}{\bar{k} (\nabla h'' \cdot \nabla h'')}, \quad (4.10)$$

where $\bar{\epsilon}$ is the dissipation of the turbulent kinetic energy, $\bar{\epsilon}_\theta$ the dissipation of $\overline{h''^2}$ and $\bar{k} = 1/2(\mathbf{u}'' \cdot \mathbf{u}'')$ the turbulent kinetic energy. This time scale ratio can be regarded as the ratio of heat decay time to the mechanical (turbulent kinetic energy) decay time. The factor $\tilde{\nu}/\tilde{a}$ suggest that the time scale ratio scales with the Prandtl number. In fact, as $y^+ \rightarrow 0$, $R \rightarrow Pr$, see Kawamura et al. [1998] and Kawamura et al. [1999]. In other words, heat will decay slower than momentum in regions with high Prandtl numbers.

Figures 4.19(a) and 4.19(b) show the expected values of the molecular Prandtl number, $E(Pr)$, conditioned on the turbulent heat flux quadrants, at the inner and outer wall, respectively. Near both walls, all turbulent heat flux quadrants have a molecular Prandtl number that is higher than the molecular Prandtl number of the reference case. Near the inner wall, the F₁ quadrant has generally a lower molecular Prandtl number than the F₄ quadrant. The same is true for the F₃ quadrant with respect to the F₂ quadrant. Near the outer wall, the F₄ and the F₁ quadrants have very similar molecular Prandtl numbers, which are lower than the molecular Prandtl number values of the F₂ and the F₃ quadrants.

To summarise, all flux quadrants are diminished by the reduced wall normal fluctuations. It is clear that all flux quadrants have different densities and molecular Prandtl numbers. The density affects the instantaneous turbulent heat flux, $\rho u''h''$, directly, while the Prandtl number affects how fast heat will decay in comparison to how fast momentum decays. A fluid particle with a high molecular Prandtl number will convect thermal energy further away from a hot wall, for instance, than a particle with a low molecular Prandtl number (if both particles have similar density and velocity), which will result in more effective heat transfer.

The results of the conditional averaging of the density and the molecular Prandtl number can be used to explain the differences in the turbulent heat flux quadrant contributions to the Nusselt numbers at the hot and cold walls between the sCO₂ cases and the reference case. The high Prandtl number compensates the effect of the low density and the attenuated velocity of the positive F₁ contribution and the negative F₄ contribution to Nu_h in the sCO₂ case. For the F₄ contribution, the effect of the high Prandtl number outweighs that of the attenuated velocity and the low density for large values of $\rho u''h''$ (large H) only. The F₂ and F₃ quadrants benefit from a high density and molecular Prandtl number. For F₃, this is visible only for very high values of $\rho u''h''$ (large H), but for F₂, the increase due to the high thermophysical properties is visible for all values of $\rho u''h''$. Near the outer wall, both positive and negative heat flux contributions to Nu_c are enhanced, as all quadrants contributions benefit from relatively high density, molecular Prandtl number and enhanced wall normal motions. The results show that the Nusselt number is influenced by both the density and molecular Prandtl number of relatively hot fluid as well as the density and molecular Prandtl number of relatively cold fluid.

4.5 Conclusions

In this work, we have investigated characteristics of turbulent heat transfer to CO₂ at a supercritical pressure of 8 MPa in an annular geometry using Direct Numerical Simulations. The inner wall of the annulus was kept at a temperature that is higher than the pseudo-critical temperature, while the outer wall was kept at a lower temperature than the pseudo-critical temperature. Results of a reference case with constant properties were compared with results of a forced convection case and a mixed convection sCO₂ case.

The variation of the thermophysical properties was found to have a large effect on mean thermal statistics. The variation of the specific heat capacity causes the mean profiles of the enthalpy and the temperature to be substantially different. High values of the specific heat capacity tend to dampen the temperature fluctuations; this is evident from both instantaneous temperature plots, as well as probability density functions of the temperature and enthalpy fluctuations. Near the hot wall, it was also found that

under mixed convection conditions, the probability density functions of enthalpy and temperature fluctuations are slightly broader than under forced convection conditions.

The thermophysical properties variations also lead to a decrease in the total heat flux compared to a flow with constant thermophysical properties. The mean thermal diffusivity profile causes local changes in the mean enthalpy gradient. The turbulent conduction term, $\overline{\rho a'' \partial_r h''}$, that arises due to fluctuations in the thermal diffusivity and the enthalpy gradient can have a significant effect locally with respect to molecular conduction and the turbulent heat flux. The fact that the turbulent heat flux is reduced by the sCO₂ conditions cannot solely be attributed to a variation in the mean density profile, as the product of the wall-normal velocity and the enthalpy fluctuations is clearly affected by both the thermophysical property variations and the mixed convection condition. Near the hot wall, both $\overline{u'' h''}$ and $\overline{w'' h''}$ are modulated by two different effects. These correlations can be attenuated due to the attenuation of the turbulent intensities, which is, in turn, the result of variations in the density and the dynamic viscosity, but may also be enhanced by a high average molecular Prandtl number, which results in larger enthalpy fluctuations. While analysing the budgets of $\overline{w'' h''}$, it was found that the pressure-scrambling term has a significant detrimental impact on the production of the streamwise turbulent heat flux in mixed convection conditions near the hot inner wall of the annulus. Physically, this is due to the fact that buoyancy forces hinder the formation of near wall streaks.

Using a relation between the Nusselt number and the radial heat fluxes, molecular conduction, turbulent conduction and turbulent heat flux, shows that turbulent conduction, $\overline{\rho a'' \partial_r h''}$, has a negligible contribution to the Nusselt number, even though locally, it can be significant with respect to molecular condition and the turbulent heat flux. The Nusselt number at the hot and cold walls of the forced convection sCO₂ case show that heat transfer deterioration or enhancement can occur without mean streamwise acceleration or mixed convection conditions. Using quadrant decomposition of the turbulent heat flux, which can be physically be interpreted as hot or cold fluid moving towards or away from a wall, it was found that different quadrants are affected differently by the variable thermophysical properties. Conditional averaging showed that the different heat flux quadrants have significantly different densities and molecular Prandtl numbers. This is important as fluid with high density is more effective at convecting heat than fluid with low density. High Prandtl numbers raise the heat decay time to mechanical decay time ratio; therefore, quadrants with a high molecular Prandtl number are more effective than quadrants with a low molecular Prandtl number. Therefore, different heat flux quadrants' contributions to the Nusselt number are affected differently if they have different properties. This means that the fluctuations of the density and the molecular Prandtl number are important in understanding heat transfer to fluids at supercritical

pressure in addition to the mean profiles of the density and the molecular Prandtl number. Concretely, this means that heat transfer to a fluid at supercritical pressure depends on the thermophysical properties of both the hot ejections as well as the cold sweeps.

Bibliography

- H. Abe, R.A. Antonia, and H. Kawamura. Correlation between small-scale velocity and scalar fluctuations in a turbulent flow. *Journal of Fluid Mechanics*, 627:1–32, 2009.
- H.S. Dol, K. Hanjalic, and T.A.M. Versteegh. A DNS-based thermal second-moment closure for buoyancy convection at vertical walls. *Journal of Fluid Mechanics*, 391: 211–247, 1999.
- A. Fenghour, W. A. Wakeham, and V. Vesovic. The viscosity of carbon dioxide. *Journal of Physical and Chemical Reference Data*, 27:31–44, 1998.
- K. Fukugata, K. Iwamoto, and N. Kasagi. Novel turbulence control strategy for simultaneously achieving friction drag reduction and heat transfer augmentation, Proc. 4th Int. Turbulence and Shear Flow phenomena, Williamsburg, Virginia, June 27-29, pp. 307-312. 2005.
- W.B. Hall and J.D. Jackson. Laminarization of a turbulent pipe flow by buoyancy forces, ASME-AIChE Natl. Heat Transf. Conf., 11th, Minneapolis, MN, ASME pap. 69-HT-55. 1969.
- H. Kawamura, K. Ohsaka, H. Abe, and K. Yamamoto. DNS of turbulent heat transfer in channel flow with low to medium-high prandtl number fluid. *International Journal of Heat and Fluid Flow*, 19:482–491, 1998.
- H. Kawamura, H. Abe, and Y. Matsuo. DNS of turbulent heat transfer in channel flow with respect to reynolds and prandtl number effects. *International Journal of Heat and Fluid Flow*, 20:196–207, 1999.
- O. Kunz, W. Wagner R. Klimeck, and M. Jaeschke. The GERG-2004 wide-range equation of state for natural gases and other mixtures. Technical report, 2007. GERG Technical Monograph 15, Fortschritt-Berichte VDI, VDI-Verlag, Düsseldorf.
- H. Li, H. Wang, Y. Luo, H. Gu, X. Shi, and T. Chen. Experimental investigation on heat transfer from a heated rod with a helically wrapped wire inside a square vertical channel to water at supercritical pressures. *Nuclear Engineering and Design*, 239:4–12, 2004.
- J.W.R. Peeters, R. Pecnik, M. Rohde, T.H.J.J. van der Hagen, and B.J. Boersma. Turbulence attenuation in simultaneously heated and cooled annular flows at supercritical pressure. *accepted for publication in Journal of Fluid Mechanics*, xx(xx):xx–xx, 2016.

- I.L. Pioro, H.F. Khartabil, and R.B. Duffey. Heat transfer to supercritical fluids flowing in channels - empirical correlations (survey). *Nuclear Engineering and Design*, 230: 69–91, 2004.
- M. Sharabi and W. Ambrosini. Discussion of heat transfer phenomena in fluids at supercritical pressure with the aid of CFD models. *Annals of Nuclear Energy*, 36:60–71, 2009.
- J. M. Wallace. Quadrant Analysis in Turbulence Research: History and Evolution. *Annual Review of Fluid Mechanics*, 48:131–158, 2016.
- W. W. Willmarth and S. S. Lu. Structure of the reynolds stress near the wall. *Journal of Fluid Mechanics*, 55:65–92, 1972.
- J.Y. Yoo. The turbulent flows of supercritical fluids with heat transfer. *Annual Review of Fluid Mechanics*, 45(1):495–525, 2013.
- B. Zappoli, D. Beysens, and Y. Garrabos. *Heat transfers and related effects in supercritical fluids*. Springer, 2015.

CHAPTER 5

TOWARDS A NEW MODEL

5.1 Introduction

In chapter 3, it was shown that turbulence can be attenuated or strengthened by the density and dynamic viscosity variations that occur in heated flows at supercritical pressure. In chapter 4 the influence of the other variable thermophysical properties on heat transfer was analysed. A relation between the Nusselt number and the turbulent heat flux quadrants was also presented. The Nusselt relation presented in chapter 4 is useful for the analysis of (turbulent) heat transfer, but not for predicting heat transfer. In this chapter, a model is created using heuristic arguments that are based on the observations and analyses of the two previous chapters. Therefore, by comparison, this chapter will be more conceptual in nature.

First, a new heat transfer model is explained conceptually. Then, a general heat transfer model is derived. Subsequently, a new friction factor and Nusselt number analogy is created from that general model, which accounts for the variations in the molecular Prandtl number and changes in turbulence through the friction factor. The new analogy is then demonstrated first, after which the model performance is shown with respect to experimental results from literature. A short discussion is presented at the end.

5.2 The model

5.2.1 Concept

On a rather simplistic level, wall bounded turbulent flows can be regarded to be locally either in a quasi-laminar state (i.e. small momentum variations) or a bursting state (locally large momentum variations). For the heat transfer model, it is assumed that the quasi-laminar state has a duration t_{lam} , while the bursting phase has a duration t_{burst} . During the bursting phase, hot fluid moves away from a heated surface, while cold fluid moves towards it. These motions will be referred to as hot ejections and cold

sweeps, which have a duration of t_h and t_c , respectively. The total time during which heat transfer takes place is denoted as t . In reality, hot ejections and cold sweep have complicated shapes. Following Hetsroni et al. [1996], the hot ejection is modelled as an axisymmetric jet. The effect of the cold sweep is considered here as well and is likewise modelled. Figure 5.1 shows the concept of a hot ejection and a cold sweep that occur in a flow near a heated surface. The hot ejection is assumed to have a cross-sectional area of A_h with a corresponding radius of $\xi_{h,0}$, while the cold sweep is assumed to have an area of A_c and a radius of $\xi_{c,0}$. The burst phase is assumed to constitute both the hot ejection and the cold sweep. The burst has therefore an cross-sectional area $A = A_h + A_c$. Both the hot ejection and the cold sweep have a temperature distribution, as is indicated by the coloured curves in figure 5.1. The mean temperatures of the hot ejection and cold burst are denoted as \overline{T}_h and \overline{T}_c .

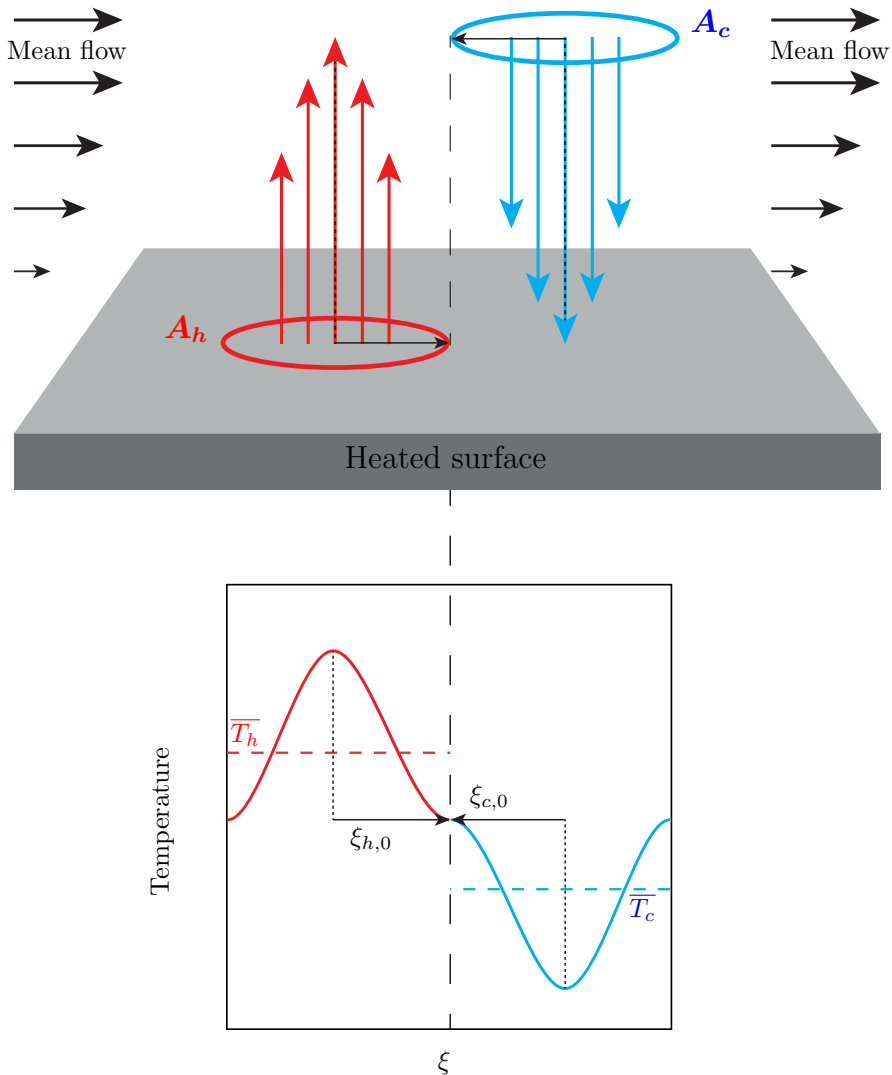


Figure 5.1: Heat transfer model concept. The top part shows a flow past a heated surface and a hot ejection and a cold sweep with cross-sectional area's A_h and A_c , respectively. The bottom part shows conceptually the temperature distributions of the hot ejection and cold sweep with their respective mean temperatures \overline{T}_h and \overline{T}_c , as well as their respective radii $\xi_{h,0}$ and $\xi_{c,0}$.

5.2.2 Derivation

The derivation that was presented by Hetsroni et al. [1996] is largely followed here, except for the fact that the cold sweep is included and that the hot ejection and cold sweep have different thermophysical properties.

The total heat transport transferred is written as Q^{tot} and is split into a contribution from conduction and a contribution from turbulence:

$$Q^{tot} = \overbrace{Q^{cond}}^{\text{laminar}} + \underbrace{Q^{hot} + Q^{cold}}_{\text{turbulent}}, \quad (5.1)$$

in which the turbulence contribution is split into a part that represents hot fluid moving away from the wall and a part that represents cold fluid moving towards the wall. The total heat flux can be represented as:

$$Q^{tot} = HTC(T_w - T_b) \times A \times t, \quad (5.2)$$

where HTC is the heat transfer coefficient and T_w the wall temperature. The conduction part is written as

$$Q^{cond} = q_w \times A \times t_{lam} \quad (5.3)$$

Q^{hot} can be modelled as an axially symmetrical jet, with a radius $\xi_{h,0}$. The total energy that is transported from the wall is

$$Q^{hot} = 2\pi \int_0^{\xi_{h,0}} \phi_h \Delta h \xi d\xi \times t_h \quad (5.4)$$

Here, Δh is the enthalpy difference between that of the fluid moving away from the wall (h) and that of the bulk region of the fluid (h_b). The subscript h refers to the hot part of the flow. This enthalpy difference corresponds to a temperature difference $\Delta T = T - T_b$. Defining the non-dimensional radius $\eta \equiv \xi/\xi_{h,0}$ yields for the hot part:

$$Q^{hot} = 2\pi \xi_{h,0}^2 \int_0^1 \phi_h \Delta h \eta d\eta \times t_h \quad (5.5)$$

Hetsroni et al. [1996] assume that the velocity profile is a function of η and that the temperature difference is a function of η and the Prandtl number Pr , based on results reported by Abramovich [1963]. Similarly, it is assumed here that,

$$\frac{\Delta h}{h_w - h_b} = f_{\Delta h}(\eta, Pr_h) \quad \text{and} \quad \frac{\phi_h}{\phi_{h,l}} = f_{\phi_h}(\eta) \quad (5.6)$$

where ϕ is the wall normal mass flux of the jet and $\phi_{h,l}$ represents the centreline mass flux of the jet-like ejection. Equation (5.6) can now be used to rewrite equation (5.5) into:

$$Q^{hot} = 2\pi \xi_{h,0}^2 \phi_{h,l} (h_w - h_b) \underbrace{\int_0^1 f_{\Delta h}(\eta, Pr_h) f_{\phi_h}(\eta) \eta d\eta}_{I(Pr_h)} \times t_h \quad (5.7)$$

Making similar assumptions as before for the cold part of the flow,

$$\frac{\Delta h}{h_w - h_b} = f_{\Delta h}(\eta, Pr_b), \quad \text{and} \quad \frac{\phi_c}{\phi_{c,l}} = f_{\phi_c}(\eta) \quad (5.8)$$

yields;

$$Q^{cold} = 2\pi\xi_{c,0}^2\phi_{c,l}(h_w - h_b) \underbrace{\int_0^1 f_{\Delta h}(\eta, Pr_c)f_{\phi_c}(\eta)\eta d\eta}_{I(Pr_c)} \times t_c \quad (5.9)$$

The result of equations (5.7) and (5.9) is that the hot fluid depends on the molecular Prandtl number of the hot fluid, while the cold part of the fluid depends on the molecular Prandtl number of the bulk region of the fluid. Combining equations (5.1), (5.3), (5.2), (5.7) and (5.9) results in

$$\begin{aligned} HTC(T_w - T_b) \times A \times t &= q_w \times A \times t_{lam} \\ &+ 2\phi_{h,l}(h_w - h_b)I(Pr_h) \times \pi\xi_{h,0}^2 \times t_h \\ &+ 2\phi_{c,l}(h_w - h_b)I(Pr_c) \times \pi\xi_{c,0}^2 \times t_c \end{aligned} \quad (5.10)$$

Multiplying the left and right side of equation (5.10) with the length scale d and dividing by the bulk thermal conductivity λ_b , $T_w - T_b$, A and t gives:

$$\begin{aligned} Nu_b = \frac{HTC \times d}{\lambda_b} &= \frac{q_w d}{\lambda_b(T_w - T_b)} \times \alpha_{t_{lam}} \\ &+ 2 \left(\frac{\phi_{h,l}(h_w - h_b)d}{\lambda_b(T_w - T_b)} \right) I(Pr_h) \times \alpha_{A_h} \times \alpha_{t_h} \\ &+ 2 \left(\frac{\phi_{c,l}(h_w - h_b)d}{\lambda_b(T_w - T_b)} \right) I(Pr_c) \times \alpha_{A_c} \times \alpha_{t_c} \end{aligned} \quad (5.11)$$

The fractions, denoted with $\alpha_{(\dots)}$, here are defined as follows: $\alpha_{t_{lam}} \equiv t_{lam}/t$, $\alpha_{A_c} \equiv \pi\xi_{c,0}^2/A$, $\alpha_{A_h} \equiv \pi\xi_{h,0}^2/A$, $\alpha_{t_c} \equiv t_c/t$, $\alpha_{t_h} \equiv t_h/t$. The relation between the time constants is $1 = \alpha_{t_{lam}} + \alpha_{t_h} + \alpha_{t_c}$. As the burst duration is much smaller than the quasi-laminar state, it follows that $1 - \alpha_{t_h} - \alpha_{t_c} \approx 1$ for $\alpha_{t_h} + \alpha_{t_c} \ll 1$. Defining $Nu_{cond} \equiv q_w d/\lambda_b(T_w - T_b)$, $Re_b = \rho_b w_b d/\mu_b$ and $\overline{Pr} = \mu_b \Delta h/(\lambda_b \Delta T)$, yields;

$$\begin{aligned} Nu_b &= Nu_{cond} \\ &+ 2 \left(\frac{\phi_{h,l}}{G} \right) Re_b \overline{Pr} I(Pr_h) \times \alpha_{A_h} \times \alpha_{t_h} \\ &+ 2 \left(\frac{\phi_{c,l}}{G} \right) Re_b \overline{Pr} I(Pr_c) \times \alpha_{A_c} \times \alpha_{t_c} \end{aligned} \quad (5.12)$$

Equation (5.12) represents a general form of a Nusselt relation that could be used to model heat transfer to fluids with variable thermophysical properties.

5.2.3 Creating a relation

Equation (5.12) is not ready to be used as a heat transfer model, since the parameters Nu_{cond} , $u_{h,l}/w_b$, $u_{c,l}/w_b$, $I(Pr_w)$, $I(Pr_c)$, as well as the fractions $\alpha_{(\dots)}$ need to be modelled. If a relation that predicts heat transfer to supercritical fluids accurately for a broad range of conditions (i.e. different pressures, different substances), all mechanisms that lead to heat transfer attenuation should be included. Direct effects of heat transfer modulate that were identified in this thesis and in literature are;

- the mean Prandtl number enhances enthalpy fluctuations (chapter 4, section 4.3.2).
- and hot ejections have a different Prandtl number than cold sweeps (chapter 4, section 4.4.2)

Mechanisms that lead to turbulence attenuation (and therefore affect heat transfer) are;

- the reconstruction of the total shear stresses and thereby the turbulent shear stress due to mean variations in the density and the dynamic viscosity, but also due to mixed convection conditions (chapter 3, section 3.2.3 and Jackson [2013]),
- the attenuation of the turbulent near wall cycle, which is visible in streaks (where ejection occur) and in the wall normal motions (chapter 3, section 3.3),
- and turbulence attenuation due to mean streamwise acceleration in situations with a developing thermal boundary layer (Jackson [2013]).

A model for the wall-normal motions is sought first. We assume that the wall temperature and the cold temperature are decent estimates for the hot and cold molecular Prandtl numbers. $\phi_{h,l}$ and $\phi_{c,l}$ are a result of the near wall cycle of a wall bounded turbulent flow. It is therefore assumed that the magnitude of both can be modelled as $\phi_{h,l} = \phi_{c,l} = \epsilon G$, with $\epsilon < 1$, where G ($\text{kg}/\text{m}^2\text{s}$) is the mean streamwise mass flux. Furthermore, the time and surface fractions are left. $\alpha_{t_h} = (t_h/t_{burst}\gamma)$ and $\alpha_{t_c} = (t_c/t_{burst}\gamma)$. Hetsroni et al. [1996] uses experimental observations, see for instance Blackwelder and Haritonidis [1983], to estimate the burst duration. His reasoning is as follows: the burst duration scaled with wall units is approximately constant, or $t_{burst}^+ \equiv t(u_\tau^2/\nu) = 91.5$. t_{burst} is modelled as $t_{burst} = b\bar{v}/w_b^2$, where b is a model constant. This model yields $t_{burst}/t = b_2(u_\tau/w_b)^2 = \gamma$. u_τ can be estimated from a friction correlation, i.e. $u_\tau \equiv \sqrt{\tau_w/\rho} = 1/2\rho_b w_b^2 f$, where f is the friction factor. This yields $\gamma = (f/2)$. We make an ‘ad hoc’ assumption here that in a non-isothermal flow with variable thermophysical properties the same time ratio $\gamma \approx f/2$. Combining this result with $\phi_{h,l} = \phi_{c,l} = \epsilon w_b$ and with

equation (5.12), yields:

$$\begin{aligned}
 Nu_b &= Nu_{cond} \\
 &+ \left(2\epsilon \times \alpha_{A_h} \times \frac{t_h}{t_{burst}} \right) \frac{f}{2} Re_b \overline{Pr} I(Pr_w) \\
 &+ \left(2\epsilon \times \alpha_{A_c} \times \frac{t_c}{t_{burst}} \right) \frac{f}{2} Re_b \overline{Pr} I(Pr_c)
 \end{aligned} \tag{5.13}$$

If the friction factor reduces to its value under (near) isothermal conditions, it may be possible to construct a relation that reverts to the Colburn–Chilton analogy for constant thermophysical properties, which may be written as:

$$Nu_b = \frac{f}{2} Re_b Pr_b^{1/3} \tag{5.14}$$

Hetsroni et al. [1996] estimate the integral $I(Pr)$ by using explicit functions of the temperature and velocity distributions of the burst. Simply by requiring that the new relation reverts to the Chilton–Colburn analogy under constant thermophysical property conditions, $I(Pr)$ can be estimated as $I(Pr) \approx APr^n$, with $n = -2/3$, who reports $n = 0.57-0.8$. This estimate is very close to the result by Hetsroni et al. [1996]. The factors α_{A_h} , α_{A_c} , t_h/t_{burst} and t_c/t_{burst} suggest that the contribution of the hot part to the Nusselt number is different from the contribution by the cold part. In the last chapter it was shown that this is indeed the case by using a relation between the turbulent heat flux and the Nusselt number. In the reference case (I), the contribution of the hot part Nu_{hot} is 16.81 and the contribution of the cold part Nu_{cold} is 11.83. In the forced supercritical CO₂ case (II), the hot part is 18.66, while the cold part is 13.78. The fractional contributions of the hot part and the cold part in the reference case are $Nu_{hot}/(Nu_{hot} + Nu_{cold}) = 0.58$ and $Nu_{cold}/(Nu_{hot} + Nu_{cold}) = 0.42$, respectively. In the supercritical case, the fractional contributions are $Nu_{hot}/(Nu_{hot} + Nu_{cold}) = 0.59$ and $Nu_{cold}/(Nu_{hot} + Nu_{cold}) = 0.41$. The differences between the fractional contributions of the hot part and the cold part are very small when comparing the reference case (I) with the supercritical CO₂ case (II). Therefore, it is assumed that $2\epsilon \times \alpha_{A_h} \times \frac{t_h}{t_{burst}} = 0.58$ and that $2\epsilon \times \alpha_{A_c} \times \frac{t_c}{t_{burst}} = 0.42$. Finally, by neglecting the conduction contribution to the Nusselt number, Nu_{cond} , the following relation is obtained:

$$Nu_b = \frac{f}{2} Re_b \overline{Pr} \left\{ \underbrace{0.58 Pr_w^{-2/3}}_{\text{hot part}} + \underbrace{0.42 Pr_b^{-2/3}}_{\text{cold part}} \right\} \tag{5.15}$$

We will refer to equation (5.15) as the ejection–sweep analogy. This intermediate result is a relation in which the contributions of the hot ejections and the cold sweeps are clearly present. Of course, the analogy reverts to the Chilton–Colburn analogy, if the thermophysical properties are constant, i.e. when $\overline{Pr} = Pr_w = Pr_b$, and when f reduces to the friction factor under isothermal conditions, f_{iso} .

5.3 Results

5.3.1 A demonstration

In the previous section, a number of heuristic and ‘ad hoc’ assumptions were made in order to transform equation (5.12) into equation (5.15). Equation (5.15) can be used to demonstrate the effect of the ejection–sweep analogy on the heat transfer coefficient for the special case that $f = f_{iso}$. For now, we will take $f_{iso} = 0.046Re_b^{-0.2}$. Figure 5.2 shows a comparison between heat transfer coefficients predicted by the Chilton–Colburn analogy and heat transfer coefficients predicted by equation (5.15) for water at 24.5 MPa for different heat flux to mass flux ratios. There are two obvious differences; the chilton–colburn analogy predicts that the maximum of the heat transfer coefficients always occurs when the bulk enthalpy equals the pseudo-critical enthalpy, while the ejection–sweep formulation predicts that the maximum heat transfer coefficient shifts towards lower bulk enthalpy values. Furthermore, there is an obvious change in the maximum heat transfer coefficient magnitude in the Colburn–Chilton analogy predictions, which is not seen in the ejection–sweep formulation. Lastly, the ejection–sweep formulation shows small local maxima both before and after the pseudo-critical enthalpy $h_{pc} = 2160$. The first is created due to the sudden drop of the Prandtl number at the wall, after the wall temperature passes the pseudo-critical temperature. The second is arises when the bulk Prandtl number decreases, after the bulk enthalpy has passed the pseudo-critical enthalpy.

This demonstration shows how the variation of the Prandtl number in the ejection–sweep formulation affects the heat transfer coefficient. In the next section, an attempt is made to mould this formulation into a useful Nusselt relation.

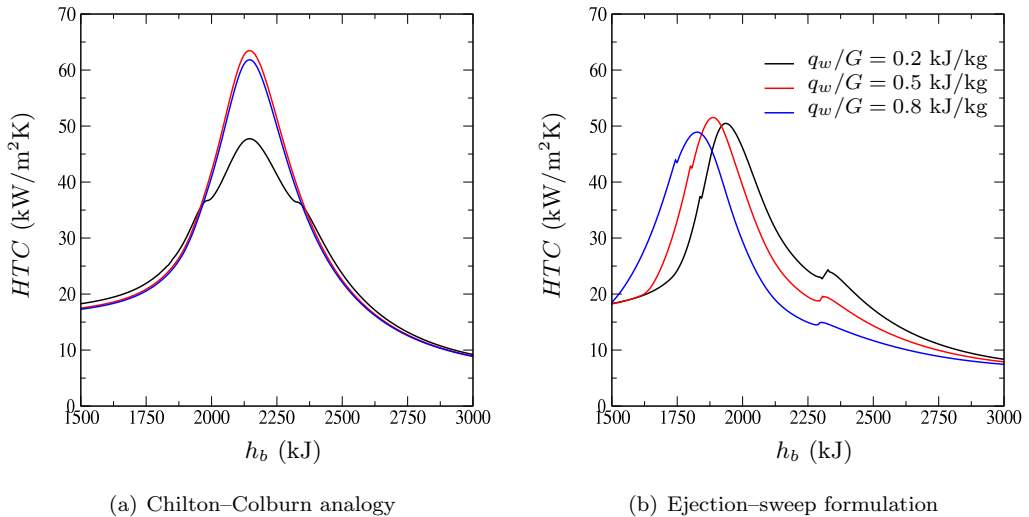


Figure 5.2: Predicted heat transfer coefficient values using the Chilton–Colburn analogy and the ejection–sweep formulation.

5.3.2 Low heat flux

In order to test if the ejection–sweep formulation might be a useful tool to predict heat transfer to fluids at supercritical pressure, it should be tested against experimental data. This is rather difficult as heat transfer to fluids at supercritical pressure is affected by various factors, which were already mentioned in section 5.2.3. Especially at high heat flux to mass flux ratios, heat transfer can be severely deteriorated as a result of relaminarisation due to buoyancy and acceleration influences. The validity of the ejection–sweep analogy may therefore only be apparent at low heat fluxes, when the flow is still turbulent, albeit attenuated. Jackson [2013] provides criteria to determine if buoyancy and acceleration influences have non-negligible effects, which may be used to identify experimental data that can be used to validate the ejection–sweep formulation:

$$\left(\frac{Gr_b}{Re_b^{2.7}} \right) \left(\frac{\mu_w}{\mu_b} \right) \frac{\rho_w}{\rho_b} < 10^{-4} \quad \text{and} \quad Ac_b < 10^{-6}, \quad (5.16)$$

where $Gr_b = gD_h^3(\rho_b - \rho_w)/(\rho_b\nu_b^2)$ is the Grashof number, which represents the ratio of buoyancy forces to viscous forces. $Ac_b = (q_w\beta_b D_h/k_b)/(Re_b^{1.625} Pr_B)$ is the so-called acceleration parameter. If the criteria of equation (5.16) hold, then buoyancy and acceleration may be considered to be negligible. Typically, cases with low heat flux to mass flux cases have negligible buoyancy or acceleration effects. However, the attenuation of turbulence due to variations in the viscosity and the density can also affect heat transfer, which is modelled by equation (5.15) by the friction factor. A recent literature review by

Fang et al. [2012] shows that the friction factor is indeed lower for heated turbulent flows at supercritical pressure than it is for similar isothermal flows. Many proposed friction factor relations are of the form;

$$f = f_{iso} \times \mathcal{F} \left(\frac{\rho_w}{\rho_b}, \frac{\mu_w}{\mu_b} \right), \quad (5.17)$$

where \mathcal{F} is the function that represents the attenuation of the friction factor due to variations in the density and the dynamic viscosity. We will chose a relation by Fang et al. [2012] that takes both the variable density and the variable viscosity into account;

$$f = f_{iso} \left(\frac{\mu_w}{\mu_b} \right)^s \quad \text{with} \quad s = 0.49 \left(\frac{\rho_f}{\rho_{pc}} \right)^{1.31}, \quad (5.18)$$

where ρ_f is the density at the film temperature $T_f = (T_w + T_b)/2$ and ρ_{pc} the density at the pseudo-critical temperature. Equation (5.18), will be used to test the validity of equation (5.15).

5.3.3 Comparisons

The experimental cases that were selected using the criteria that were described earlier by equation (5.16) are listed in table 5.1. In all experimental cases, the heated fluid is water at supercritical pressure. The wall heat flux to mass flux ratio, q_w/G varies from 0.2 to 0.4, while the thermodynamic pressure ranges from 24.1 MPa to 31 MPa. The hydraulic diameter D_h is similar in all cases. The ejection–sweep analogy will be tested against experimental results, as well as the Colburn–Chilton analogy in conjunction with (5.18). For the isothermal friction factor, the following relation is used: $f_{iso} = 0.046Re_b^{-0.2}$. The bulk temperature of the flow is determined from the bulk enthalpy, which is determined as:

$$h_b(z) = h_0 + \left(\frac{q_w}{G} \right) \left(\frac{P}{A_G} \right) (z - z_0), \quad (5.19)$$

where $h_b(z)$ (J) is the bulk enthalpy at location z (m), q_w (W/m²) the wall heat flux, G the average streamwise mass flux (kg/m²s), P (m) the perimeter of the heated geometry, A_G (m²) the cross-sectional area of the flow and h_0 (J) the inlet enthalpy at location z_0 (m). After the bulk temperatures are known, equation (5.15) is used iteratively to solve for the wall temperature $T_w(z)$ at a location z .

Figure 5.3 shows a comparison between the heat transfer coefficient from case E-1, the coefficients as predicted by the Chilton–Colburn analogy and the ejection–sweep analogy. There are two distinct differences between the Chilton–Colburn analogy and the ejection–sweep correlation. Firstly, the erroneous deterioration prediction by Chilton–Colburn between $T_f = 360$ and $T_f = 400$ is not present in the ejection–sweep correlation.

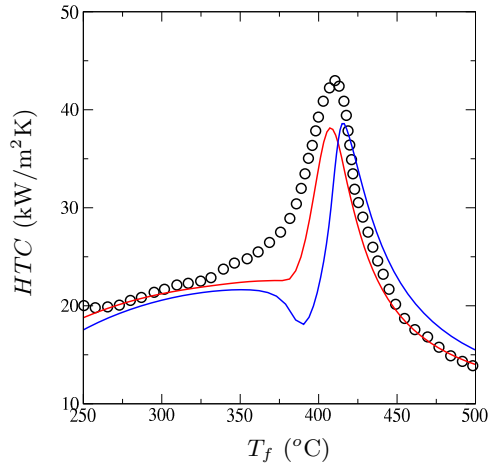


Figure 5.3: Comparison of heat transfer coefficients as predicted by the ejection-sweep analogy (red) and the Chilton–Colburn analogy with an experiment from Swenson et al. [1965] (Case E–I). $T_f \equiv (T_w + T_b)/2$ is the film temperature.

Furthermore, the heat transfer coefficient peak location (with respect to the film temperature) is different. Overall, the ejection-sweep analogy performs better, both qualitatively and quantitatively. Qualitatively similar results are obtained for cases E–2 to E–V. Comparisons between predicted wall temperatures of both analogies and experimental results are shown in figures 5.4 and 5.5. It is clear from these results that a sudden rise in wall temperature, which is the result of a decrease in friction factor (and therefore turbulence), is suppressed by the ejection-sweep formulation.

| Case | q/G (kJ/kg) | D_h (mm) | Pressure (MPa) |
|--------------------|---------------|------------|----------------|
| ¹ E–I | 0.37 | 9.42 | 31.0 |
| ² E–II | 0.28 | 10 | 24.1 |
| ² E–III | 0.39 | 10 | 24.1 |
| ³ E–IV | 0.18 | 8 | 24.5 |
| ³ E–V | 0.37 | 8 | 24.5 |

Table 5.1: Experimental cases with negligible or small acceleration and/or buoyancy effects in heated water at supercritical pressure. **For a large range of positive coefficients, excellent predictions may be obtained. ¹Swenson et al. [1965], ²Mokry et al. [2011], ³Yamagata et al. [1972].

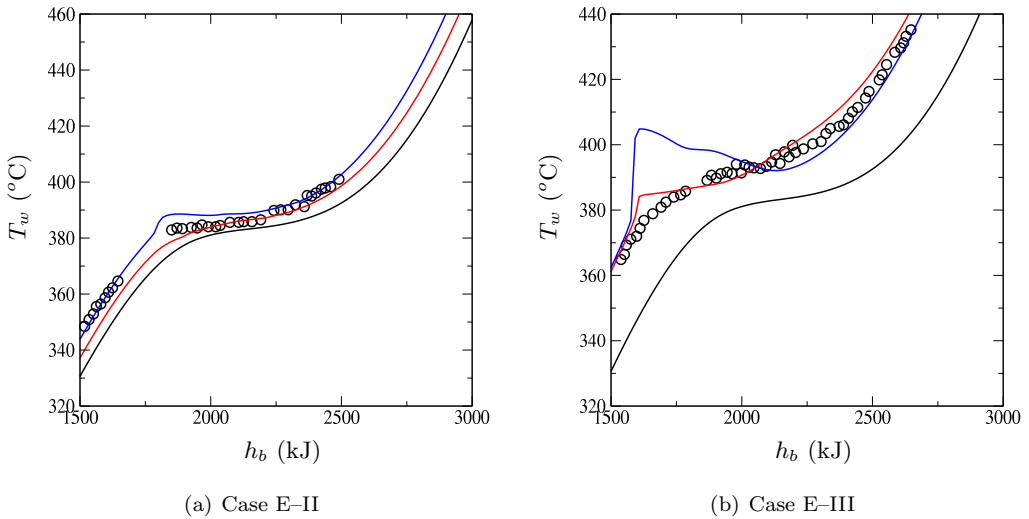


Figure 5.4: Comparison of wall temperatures as predicted by the ejection-sweep analogy (red) and the Chilton–Colburn analogy with an experiment from Yamagata et al. [1972].

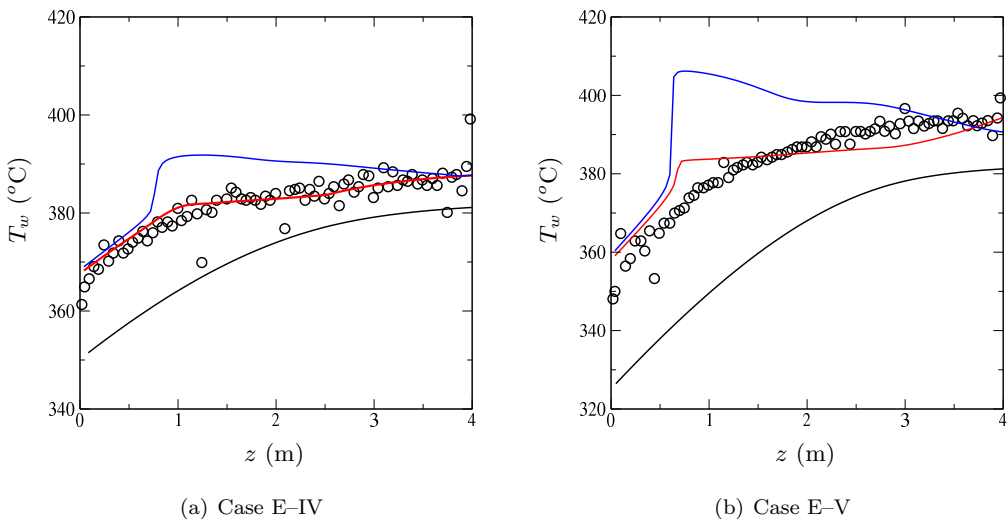


Figure 5.5: Comparison of wall temperatures as predicted by the ejection-sweep analogy (red) and the Chilton–Colburn analogy with an experiment from Mokry et al. [2011].

5.4 Discussion

A new analogy between the Nusselt number and the friction factor was derived in this chapter. This derivation was based on the observation that the most important contribu-

tions to turbulent heat transfer are hot fluid motions from a heated surface (hot ejections) and cold fluid motions towards a heated surface (cold sweeps). These observations are literally present in the new analogy in the form of a molecular Prandtl number based on the wall temperature and a molecular Prandtl number based on the bulk temperature. The new analogy (called the ejection–sweep analogy) is intuitive for heated fluids with large thermophysical property variations; through the friction factor, heat transfer is predicted by the analogy to be attenuated (in heated flows). The attenuation is mitigated by the Prandtl numbers at wall temperature and at bulk temperature. The ejection–sweep was tested against five experimental cases (with a relatively low heat flux) from literature. Using a friction relation developed for heated flows at supercritical pressure, available from literature, it was shown that the ejection–sweep analogy gives better predictions than the Chilton–Colburn analogy. The ejection–sweep analogy results are therefore in line with the observations and analyses of chapter four. These results indicate that the ejection–sweep analogy may be a valid model for heat transfer to fluids at supercritical pressure at low heat flux to mass flux ratios. Furthermore, the ejection–sweep formulation may not be valid for situations where the turbulent flow completely laminarises, since in such a flow there are no ejections and sweeps.

Bibliography

- G.N. Abramovich. *The theory of turbulent jets*. Massachusetts Institute of Technology, Cambridge, MA, 1963.
- R.F. Blackwelder and J.H. Haritonidis. Scaling of the bursting frequency in turbulent boundary layers. *Journal of Fluid Mechanics*, 132:87–103, 1983.
- X. Fang, Y. Xu, X. Su, and R. Shi. Pressure drop and friction factor correlations of supercritical flow. *Nuclear Engineering and Design*, 242:323–330, 2012.
- G. Hetsroni, L.P. Yarin, and D. Kaftori. A mechanistic model for heat transfer from a wall to a fluid. *International Journal of Heat and Mass Transfer*, 39:1475–1478, 1996.
- J.D. Jackson. Fluid flow and convective heat transfer to fluids at supercritical pressure. *Nuclear Engineering and Design*, 264:24–40, 2013.
- S. Mokry, I. Pioro, A. Farah, K. King, S. Gupta, W. Peiman, and P. Kirillov. Development of supercritical water heat-transfer correlation for vertical bare tubes. *Nuclear Engineering and Design*, 241:1126–1136, 2011.
- H.S. Swenson, J.R. Carver, and C. R. Kakarala. Heat transfer to supercritical water in smooth-bore tubes. *ASME Journal of Heat Transfer*, 87(4):477–483, 1965.
- K. Yamagata, K. Nishikawa, S. Hasegawa, T. Fujii, and S. Yoshida. Forced convective heat transfer to supercritical water flowing in tubes. *International Journal of Heat and Mass Transfer*, 15:2575–2593, 1972.

CHAPTER 6

CONCLUSIONS

Heat transfer to fluids at supercritical pressure is different from heat transfer at lower pressures due to strong variations of the thermophysical properties with the temperature (close to the pseudocritical temperature). This is due to the fact that during a heating process it changes from a fluid with liquid-like properties to a fluid with gas-like properties. Fluids at supercritical pressure have many industrial applications. However, it is difficult to accurately predict heat transfer to such fluids. A better understanding of how the variable thermophysical properties of a fluid at supercritical pressure affect heat transfer may help to develop more accurate heat transfer models.

Direct Numerical Simulations of a simultaneously heated and cooled annular flow of carbon dioxide have yielded the following insights with respect to turbulence attenuation due to thermophysical properties variations in a fully developed thermal boundary layer:

1. Mean velocity profiles, turbulent shear stresses and turbulent intensities are significantly affected by the mean variation in dynamic viscosity and density. The attenuation (near a heated surface) or enhancement (near a cooled surface) of the turbulent shear stress and the mean strain rate are accompanied by a diminished production of the turbulent kinetic energy (near a heated surface) or an enhanced production (near a cooled surface).
2. The self regenerating cycle of near wall turbulence was found to be affected through the attenuation or enhancement of streaks. Near wall streaks have a lower density and dynamic viscosity near a heated surface, or a higher density and dynamic viscosity near a cooled surface than the surrounding fluid. Buoyancy acts as to counteract the formation of streaks near a heated surface, but as to enhance them near a cooled surface in gravity opposed flows. Furthermore, positive and negative thermal expansion regions exist within the streaks, which have a detrimental effect on streak coherence.

3. The near-wall turbulence regeneration cycle is also affected through the attenuation or enhancement of the streamwise momentum vorticity (the curl of the momentum $\rho\mathbf{u}$). Budgets show that the torque between the kinetic energy gradient and the density gradient act as a sink to the generation of streamwise momentum vorticity near a heated surface, but as a source term near a cooled surface. Physically, this means that positive and negative wall normal motions may have different momenta due to a difference in the density between those motions.
4. A scaling analysis shows that a large Prandtl number enhances the variable density effects of the streak and streamwise vorticity attenuation.

The Direct Numerical Simulations also yielded insights into how heat transfer is affected by the variable thermophysical properties of a fluid at supercritical pressure:

5. The variation of the specific heat capacity significantly affects the mean temperature profile with respect to the mean enthalpy profile. Furthermore, in flow regions with a high specific heat capacity, temperature fluctuations are diminished, but are enhanced in flow regions with a low specific heat capacity. Furthermore, the variation of the specific heat capacity causes the probability density function of the temperature fluctuations to be radically different from that of the enthalpy fluctuations.
6. While a correlation between fluctuating thermal diffusivity and fluctuating enthalpy gradient (called *turbulent conduction*) may be locally large with respect to molecular conduction or even the turbulent heat flux, its contribution to the Nusselt number is negligible.
7. The turbulent heat flux, $\overline{\rho u'' \widetilde{h''}}$ is not only affected by the mean density; the correlation $\widetilde{u'' \widetilde{h''}}$ is affected by both the attenuation of the wall normal motions, as well as the enhancement of the enthalpy fluctuations near a heated surface. The enhancement of the enthalpy fluctuations can be attributed to a large average molecular Prandtl number.
8. Heat transfer deterioration can occur without mean streamwise acceleration or buoyancy effects.
9. The largest contributions to the Nusselt number come from hot fluid moving away from a heated surface (hot ejection) and cold fluid moving towards it (cold sweep). Due to the variations in thermophysical properties, the hot fluid can have a different density or molecular Prandtl number than the cold fluid has. These contributions to the Nusselt number are therefore affected differently.

These insights have been used to develop a new analogy between the Nusselt number and the friction factor. This analogy is based on the observation that hot ejections and cold sweeps have different Prandtl numbers and therefore affect the Nusselt number differently. A decrease in turbulent heat transfer may be mitigated by the Prandtl numbers of the hot ejections or the cold sweeps. Validations of the new analogy with experiments from literature suggest that the analogy is valid at low heat flux to mass flux rates. As such, the new analogy may help to develop a better model for heat transfer to fluids at supercritical pressure in the future.

ACKNOWLEDGEMENTS

When I started my PhD candidacy at Delft, University of Technology in 2012, I imagined that I would research a subject by myself for four years, while regularly reporting to my thesis advisors.¹ While there is no doubt that the ideas that were developed during the past four years are my own, there should be equally no doubt that these ideas could not have been developed without the proper guidance of my thesis advisors. First of all, I would like to thank Dr Ir Martin Rohde, who made the project, of which my PhD research was but a part, not only possible, but who also early on tipped me off about the PhD candidacy itself. Martin, I appreciate the candidness with which you judged my writings. Although we met only a couple of times per year, I also appreciate the lively discussions with my ‘tweede promotor’ Professor Dr Ir Tim van der Hagen. I think it is fair to say that I should also thank my ‘eerste promotor’, Professor Dr Ir Bendiks Jan Boersma and my ‘co-promotor’ Dr Rene Pecnik. Bendiks and Rene, your willingness and thoroughness in helping me is greatly appreciated. Bendiks, I especially appreciate the speed at which you corrected my writings. I also remember a stimulating discussion on the usefulness of academia in general; your insight convinced me that I am most at home in the academic world. Rene, I love our fiery discussions and I hope that I’m not the cause of too many headaches (I used the present here to emphasise my eagerness to start another discussion soon and in that sense, I should perhaps stress the fact that the graduate school course ‘effective negotiation’ has completely and utterly failed in conveying its message to me).²

During my PhD candidacy, I worked in two different groups at the university; Energy Technology (ET³) and Nuclear Energy and Radiation Applications (NERA).⁴ To my colleagues of SCG-1⁵ in Energy Technology, Ashish, Hassan, Uttiya, Enrico and Gustavo;

¹In a previous iteration, I had written ‘occasionally’ instead of ‘regularly’... I must admit that it looked rather silly.

²I was taught that knowledge about oneself is power. I hereby admit that more than once, my conduct regarding the graduate school program could have been described as rather contumacious.

³No, we do not phone home.

⁴Formerly known only as PNR; short for Physics of Nuclear Reactors.

⁵Super-Critical Group 1; a nickname for our CFD-team and a reference to a sci-fi television series from the late nineties I used to watch. Apparently, the reference was not as conspicuous as I thought it would be, as none of my colleagues initially understood what the ‘1’ stood for.

I hereby convey my heartfelt appreciation for all the discussions, food, drinks and laughter that we shared. I wish you well. The same goes for my acquaintances and colleagues at NERA, with whom I also spent a great deal of time; elvtarszok Zoltan, Károly and Jozsef, my fellow Dutchmen Gert-Jan, Jan-Leen, Danny, Frank and Bart, Stuart from across the channel, our ‘zuidbuur’ Christophe, who significantly contributed to the creation of the research project that I mentioned earlier, il papa Luca, as well as Dimitrios ‘do-you-know-who-I-am?’ Pavlidis, who taught me how to say ‘octopus’ in Greek.⁶

From the IRS⁷ group, I’d like to thank explicitly Marloes; you are quite the organizer and your enthusiasm makes our working environment a friendlier and livelier place. Also thanks for helping me with various last minute ‘defence-details’⁸. Guido and Wei Wei, I enjoyed our time discussing and drinking. The same goes for Karsten and Mahinder from the ETh⁹ group.

I am immensely and eternally grateful to my father and my mother, for stimulating me in my many endeavours. Without their love, support and just a modicum of sternness, this thesis and many other achievements would have been impossible. It still saddens me that my mother has passed away recently. She would have loved to hear me defend this thesis. I remember her fondly and although I miss her, knowing that she can finally rest, makes her loss just a little easier to accept.

Finally, but certainly not least, I would like to thank my brothers, Aernout and Sytze, and my friends Alex and Suzanna as well, for pulling me away from my work sometimes; after all, *“all work and no play makes Jack a dull boy.”*

⁶Χτᾶποδι; bang properly before consumption.

⁷To be clear, this stands for Intensified Reaction & Separation Systems. I did not befriend a mob of tax collectors during my PhD candidacy.

⁸I dare say that swearing regularly (without harming fellow human souls) is a healthy way of releasing built up stress.

⁹Engineering Thermodynamics, *in Delft*

LIST OF PUBLICATIONS

Journal publications

J. W. R. Peeters, R. Pecnik, M. Rohde, T. H. J. J. van der Hagen, B. J. Boersma, *Characteristics of turbulent heat transfer in an annulus at supercritical pressure*, submitted to Physical Review Fluids (2016).

J. W. R. Peeters, R. Pecnik, M. Rohde, T. H. J. J. van der Hagen, B. J. Boersma, *Turbulence attenuation in simultaneously heated and cooled annular flows at supercritical pressure*, Journal of Fluid Mechanics 799, pp. 505–540 (2016). *This article was featured on the cover of the Journal of Fluid Mechanics.*

M. Rohde, **J. W. R. Peeters**, A. Pucciarelli, A. Kiss, Y. F. Rao, E. N. Onder, P. Muehlbauer, A. Batta, M. Hartig, V. Chatoorgoon, R. Thiele, D. Chang, S. Tavoularis, D. Novog, D. McClure, M. Gradecka and K. Takase, *A Blind, Numerical Benchmark Study on Supercritical Water Heat Transfer Experiments in a 7-Rod Bundle*, ASME Journal of Nuclear Engineering and Radiation Science (2), 021012 (2016).

A. Patel, **J. W. R. Peeters**, B. J. Boersma, and R. Pecnik, *Semi-local scaling and turbulence modulation in variable property turbulent channel flows*, Physics of Fluids 27, 095101 (2015).

Conference presentations and publications

J. W. R. Peeters, M. Rohde, *Towards a Nusselt number – friction factor analogy for heated turbulent fluids at supercritical pressure*, submitted to the 17th International Topical Meeting on Nuclear Reactor Thermal Hydraulics (NURETH 17), Xi'an, Shaanxi, China, September 3rd–8th (2017).

J. W. R. Peeters, R. Pecnik, M. Rohde, B. J. Boersma *Direct numerical simulations of heat transfer to a turbulent annular upward flow at supercritical pressure*, The 3rd International Meeting of Specialists on Transfer and Fluid Mechanics at Supercritical Pressure, 25th & 26th August, Sheffield, The United Kingdom (2016).

A. Patel, **J. W. R. Peeters**, B. J. Boersma, R. Pecnik, *Effect of viscosity and density gradients on turbulent channel flows*, 15th European Turbulence Conference (ETC15), August 25th–28th, Delft, The Netherlands (2015).

J. W. R. Peeters, R. Pecnik, M. Rohde, T. H. J. J. van der Hagen, B. J. Boersma, *Near wall structures in turbulent flows with strong thermo-physical property variations*, 10th ERCOFTAC WORKSHOP Direct and Large Eddy Simulation 10, 27th–29th May, Limassol, Cyprus (2015).

B. J. Boersma, R. Pecnik, H. Nematì, **J. W. R. Peeters** *Numerical simulation of turbulent heat transfer close to the critical point*, AIP Conference Proceedings 1648, 030006 (2015).

J. W. R. Peeters, R. Pecnik, M. Rohde, T. H. J. J. van der Hagen, B. J. Boersma, *Direct Numerical Simulation of heat transfer to CO₂ in an annulus at supercritical pressure*, 10th International ERCOFTAC Symposium on Engineering Turbulence Modelling and Measurements, 17–19 Spetember 2014, Marbella, Spain (2014).

Book chapters

A. Patel, R. Pecnik, **J. W. R. Peeters**, S. Hickel, M. E. Moghadam *Turbulence modulation by variable density and viscosity*, Center for Turbulence Research, Proceedings of the Summer Program 2016, (to appear in 2017).

CURRICULUM VITAE

Jurriaan Willem Reinier Peeters was born on the 12th of November 1985 in Nieuwegein, the Netherlands. He attended the Stedelijk Gymnasium of Utrecht from 1998 to 2004. At the Stedelijk Gymnasium, he developed a strong interest in nature and technology. He therefore enrolled in the Applied Physics bachelor program at the technical university of Delft in 2004. He finished the program by writing a thesis titled: *"simulating multiphase magneto-hydrodynamics in gas metal arc-welding using OpenFOAM."* Afterwards, he enrolled in the Applied Physics master program, which he finished in 2011 with the thesis: *"developing thermal boundary layers in laminar fluid flows at supercritical pressure."* As a student, he was a teaching assistant for four years, helping with courses such as thermodynamics, physical transport phenomena and more. He was also active in various student organizations.

After his graduation from Delft, University of Technology, he became an intern at the Nuclear Research and consultancy Group (NRG) in Petten (the Netherlands) for three months. Soon after, he became a full time employee. At NRG, he worked on various RANS-LES hybrid turbulence modelling methods as well as heat transfer at low Prandtl numbers using LES-methods.

In 2012, he joined the group Energy Technology of the faculty Mechanical, Maritime and Materials Engineering as a PhD-candidate. This thesis is the result of his time as a PhD student.

APPENDIX

A.1 Derivations

A.1.1 Low Mach number approximation

The Navier Stokes equations may be written in dimensional form as:

$$\frac{\partial \rho^\circ}{\partial t} + \nabla \cdot \rho^\circ \mathbf{u}^\circ = 0, \quad (1)$$

$$\frac{\partial \rho^\circ \mathbf{u}^\circ}{\partial t} + \nabla \cdot \rho^\circ \mathbf{u}^\circ \mathbf{u}^\circ = -\nabla p^\circ + \nabla \cdot 2\mu^\circ \mathbf{S}^\circ + \rho^\circ \mathbf{g}^\circ, \quad (2)$$

and

$$\frac{\partial \rho^\circ h^\circ}{\partial t} + \nabla \cdot \rho^\circ \mathbf{u}^\circ h^\circ = \frac{\partial p^\circ}{\partial t} + \mathbf{u}^\circ \cdot \nabla p^\circ - \nabla \cdot \mathbf{q}^\circ + 2\mu^\circ \mathbf{S}^\circ : \nabla \mathbf{u}^\circ \quad (3)$$

In order to derive the low Mach number approximation of the Navier Stokes equations, the momentum equation must first be non-dimensionalised. The non-dimensionalisation is exactly as in section 2.1, except that $p = p^\circ / (\rho_{pc}(c^\circ)^2)$, where $(\dots)^\circ$ denotes a dimensional quantity, $(\dots)_{pc}$ a property at the pseudo-critical temperature and where c° is the speed of sound in m/s. The result is written as:

$$\frac{\partial \rho \mathbf{u}}{\partial t} + \nabla \cdot \rho \mathbf{u} \mathbf{u} = -Ma^{-2} \nabla p + Re^{-1} \nabla \cdot 2\mu \mathbf{S} + Fr^{-1} \rho \hat{\mathbf{x}}, \quad (4)$$

where $Ma = w_b^\circ / c^\circ$ is the Mach number, $\hat{\mathbf{x}}$ the unit vector in which the gravitational vector points. Next, the variables are asymptotically expanded as follows:

$$f = f^{(0)} + Ma f^{(1)} + Ma^2 f^{(2)} + \dots + \text{higher order terms} \quad (5)$$

The f here denotes ρ , μ , \mathbf{S} , \mathbf{u} , or p . Terms that have the same order $\mathcal{O}(Ma)$ balance each other out. Collecting the terms of the lowest order gives:

$$\begin{aligned} \mathcal{O}(Ma^{-2}) : \quad & Ma^{-2} \nabla p^{(0)} & = 0 \\ \mathcal{O}(Ma^{-1}) : \quad & Ma^{-1} \nabla p^{(1)} & = 0 \\ \mathcal{O}(1) : \quad & \frac{\partial \rho^{(0)} \mathbf{u}^{(0)}}{\partial t} + \nabla \cdot \rho^{(0)} \mathbf{u}^{(0)} \mathbf{u}^{(0)} & = -\nabla p^{(2)} + Re^{-1} \nabla \cdot 2\mu^{(0)} \mathbf{S}^{(0)} \\ & & + Fr^{-1} \rho^{(0)} \hat{\mathbf{x}} \end{aligned} \quad (6)$$

The higher order terms are neglected. The first part of equation (6) show that $p^{(0)}$ and $p^{(1)}$ are constant in space. The low Mach number approximation of the momentum equation is:

$$\frac{\partial \rho^{(0)} \mathbf{u}^{(0)}}{\partial t} + \nabla \cdot \rho^{(0)} \mathbf{u}^{(0)} \mathbf{u}^{(0)} = -\nabla p^{(2)} + Re^{-1} \nabla \cdot 2\mu^{(0)} \mathbf{S}^{(0)} + Fr^{-1} \rho^{(0)} \hat{\mathbf{x}} \quad (7)$$

Using a similar procedure for the conservation of mass equations, one finds:

$$\frac{\partial \rho}{\partial t} + \nabla \cdot \rho \mathbf{u} = 0, \quad (8)$$

The enthalpy transport equation is non-dimensionalised using the same relations as before, as well as $h = h^\circ / (c^\circ)^2$ and $\mathbf{q} = \mathbf{q}^\circ c_p^\circ D_h / (k^\circ (c^\circ)^2)$:

$$\frac{\partial \rho h}{\partial t} + \nabla \cdot \rho \mathbf{u} h = \frac{\partial p}{\partial t} + \mathbf{u} \cdot \nabla p - (Re_b Pr)^{-1} \nabla \cdot \mathbf{q} + (Ma^2 / Re_b) 2\mu \mathbf{S} : \nabla \mathbf{u} \quad (9)$$

Again making use of asymptotic expansions and subsequently collecting terms of the two lowest orders yields:

$$\begin{aligned} \mathcal{O}(1): \quad \partial_t(\rho^{(0)} h^{(0)}) + \nabla \cdot \rho^{(0)} \mathbf{u}^{(0)} h^{(0)} &= \frac{\partial p^{(0)}}{\partial t} + \mathbf{u}^{(0)} \cdot \nabla p^{(0)} - (Re_b Pr)^{-1} \nabla \cdot \mathbf{q}^{(0)} \\ \mathcal{O}(Ma): \quad \partial_t(p^{(1)}) &= 0 \end{aligned} \quad (10)$$

By equation (6), $\mathbf{u}^{(0)} \cdot \nabla p^{(0)} = 0$, which results in:

$$\frac{\partial \rho^{(0)} h^{(0)}}{\partial t} + \nabla \cdot \rho^{(0)} \mathbf{u}^{(0)} h^{(0)} = \frac{\partial p^{(0)}}{\partial t} - (Re_b Pr)^{-1} \nabla \cdot \mathbf{q}^{(0)} \quad (11)$$

Equations (7), (8), (11) form the low Mach number approximation to the full Navier Stokes equations. From (11) and (6) it follows that $p^{(0)}$ is a function of the time only. The total pressure can be decomposed into two parts, $p^{(0)}$ and $p^{(2)}$, which are the thermodynamic and hydrodynamic pressure, respectively. In fluids at supercritical pressure, $p^{(2)}$ is much smaller than $p^{(0)}$.

A.1.2 Pressure in a simultaneously heated and cooled periodic annulus

In equation (11), the pressure term can be evaluated as follows. By integrating (11) with respect to the volume V , one obtains:

$$\frac{\partial p^{(0)}}{\partial t} = \frac{1}{V} \frac{\partial}{\partial t} \iiint_V \rho^{(0)} h^{(0)} dV + \frac{1}{V} \iint_{\mathbf{a}} \rho \mathbf{u}^{(0)} h^{(0)} \cdot d\mathbf{a} + (Re_b Pr)^{-1} \frac{1}{V} \iint_{\mathbf{a}} \mathbf{q}^{(0)} \cdot d\mathbf{a} \quad (12)$$

The divergence theorem was used to rewrite the second and third term on the right hand side. \mathbf{a} represents a surface vector. For the annular geometry that is simultaneously

heated and cooled of this study, the second term is equal to zero, since there is no mass flux through the walls of the annulus. For an infinitely long annulus, in which the thermal boundary layer is fully developed, the heat flow through the inner wall is equally large as that at the outer wall, but of opposite sign. The third term is therefore zero as well. Lastly, for a fully developed thermal field with respect to mean statistics, the first term should be zero as well; the total heat of the system should not change over time. This suggests that $\partial p^{(0)}/\partial t$ should be zero for a fully developed flow field and thermal field inside an annulus that is simultaneously heated and cooled.

A.1.3 Derivation of the momentum-vorticity equation

Here, we will show how the derivation of the evolution equation of the momentum-vorticity can be derived. We will use various vector- and tensor identities that can be found in Gurtin et al. [2010] or Bladel [2007]. In such identities, f will denote a scalar, \mathbf{a} and \mathbf{b} vectors, and \mathbf{T} a second order tensor. Furthermore, we will define $\boldsymbol{\chi} \equiv \nabla \times \rho \mathbf{u}$, $\boldsymbol{\omega} \equiv \nabla \times \mathbf{u}$, $K = (\mathbf{u} \cdot \mathbf{u})/2$, $\mathbf{l} \equiv \boldsymbol{\chi} \times \mathbf{u}$ and $\psi \equiv \nabla \cdot \mathbf{u}$.

Taking the curl of the Navier-Stokes equations for momentum in conservative form yields the following terms:

$$\underbrace{\nabla \times \frac{\partial \rho \mathbf{u}}{\partial t}}_I + \underbrace{\nabla \times \nabla \cdot (\rho \mathbf{u} \mathbf{u})}_{II} = - \underbrace{\nabla \times \nabla p}_{III} + \underbrace{\nabla \times \rho \mathbf{g}}_{IV} + \underbrace{\nabla \times \nabla \cdot 2\mu \mathbf{S}}_V. \quad (13)$$

The third term equals $\mathbf{0}$ as it is the curl of a gradient. The other terms can be rewritten as follows:

$$I : \nabla \times \frac{\partial \rho \mathbf{u}}{\partial t} = \frac{\partial (\nabla \times \rho \mathbf{u})}{\partial t} = \frac{\partial \boldsymbol{\chi}}{\partial t} \quad (14)$$

Using the differential dyadic identity $\nabla \cdot (\mathbf{a} \mathbf{b}) = (\nabla \cdot \mathbf{a}) \mathbf{b} + (\mathbf{a} \cdot \nabla) \mathbf{b}$, we can write:

$$II : \nabla \times \nabla \cdot (\rho \mathbf{u} \mathbf{u}) = \nabla \times \left(\underbrace{((\nabla \cdot \mathbf{u}) \rho \mathbf{u})}_{II_A} \right) + \nabla \times \left(\underbrace{(\mathbf{u} \cdot \nabla \rho \mathbf{u})}_{II_B} \right) \quad (15)$$

from the vector identity $\nabla(\mathbf{a} \cdot \mathbf{b}) = \mathbf{a} \times \nabla \times \mathbf{b} + \mathbf{b} \times \nabla \times \mathbf{a} + \mathbf{b} \cdot \nabla \mathbf{a} + \mathbf{a} \cdot \nabla \mathbf{b}$, II_B can be rewritten as:

$$II_B : \mathbf{u} \cdot \nabla \rho \mathbf{u} = \nabla(\rho \mathbf{u} \cdot \mathbf{u}) - \rho \mathbf{u} \cdot \nabla \mathbf{u} - \mathbf{u} \times (\nabla \times \rho \mathbf{u}) - \rho \mathbf{u} \times (\nabla \times \mathbf{u}) \quad (16)$$

Using the same vector identity as before to rewrite $\mathbf{u} \cdot \nabla \mathbf{u}$, together with the identities for $\boldsymbol{\chi}$ and $\boldsymbol{\omega}$ yields:

$$II_B : \mathbf{u} \cdot \nabla \rho \mathbf{u} = \nabla(\rho \mathbf{u} \cdot \mathbf{u}) - \rho \nabla \left(\frac{\mathbf{u} \cdot \mathbf{u}}{2} \right) + \rho \mathbf{u} \times \boldsymbol{\omega} - \mathbf{u} \times \boldsymbol{\chi} - \rho \mathbf{u} \times \boldsymbol{\omega} \quad (17)$$

Noting that the curl of a gradient equals zero, we may write:

$$\nabla \times (\mathbf{u} \cdot \nabla \rho \mathbf{u}) = -\nabla \times \rho \nabla \left(\frac{\mathbf{u} \cdot \mathbf{u}}{2} \right) - \nabla \times \mathbf{u} \times \boldsymbol{\chi} \quad (18)$$

Thus, with equations (15) and (18) and noting that $\nabla \times \rho \nabla K = -\nabla \times K \nabla \rho$, term *II* becomes:

$$II : \nabla \times \nabla \cdot (\rho \mathbf{u} \mathbf{u}) = -\nabla \times \mathbf{u} \times \boldsymbol{\chi} + \nabla \times (\rho \psi \mathbf{u}) - \nabla \times \rho \nabla K \quad (19)$$

Finally term *V*, can be rewritten using the identity $\nabla \times (\nabla \cdot \mathbf{T}) = \nabla \cdot (\nabla \times \mathbf{T}^T)$:

$$\nabla \times (\nabla \cdot 2\mu \mathbf{S}) = \nabla \cdot (\nabla \times 2\mu \mathbf{S}^T) = \nabla \cdot (\nabla \times 2\mu \mathbf{S}). \quad (20)$$

With the identity $\nabla \times f \mathbf{T} = \nabla f \times \mathbf{T} + f \nabla \times \mathbf{T}$, we can now write:

$$\nabla \cdot (\nabla \times 2\mu \mathbf{S}) = \nabla \cdot (2\nabla \mu \times \mathbf{S}) + \nabla \cdot 2\mu (\nabla \times \mathbf{S}). \quad (21)$$

Noting that $\mathbf{S} = \frac{1}{2}(\nabla \mathbf{u}) + \frac{1}{2}(\nabla \mathbf{u})^T - \frac{1}{3}(\nabla \cdot \mathbf{u})\mathbf{I}$ The last term here can further be simplified using identities $\nabla \times (\nabla \mathbf{a}) = 0$, $\nabla \times (\nabla \mathbf{a})^T = \nabla(\nabla \times \mathbf{a})$ and $\nabla \cdot (\nabla \times f \mathbf{I}) = 0$ and the definitions:

$$\nabla \cdot 2\mu (\nabla \times \mathbf{S}) = \nabla \cdot \mu \nabla \boldsymbol{\omega} \quad (22)$$

Collecting all terms gives:

$$\begin{aligned} \frac{\partial \boldsymbol{\chi}}{\partial t} &= -\nabla \times \mathbf{l} + \nabla \cdot \mu \nabla \boldsymbol{\omega} \\ &+ \nabla \times \rho \mathbf{g} - \nabla \times (\psi \rho \mathbf{u} + K \nabla \rho) \\ &+ \nabla \cdot (2\nabla \mu \times \mathbf{S}), \end{aligned} \quad (23)$$

which is the equation that is used in section 3.4.

A.1.4 Fourier's law in terms of the enthalpy

Under the low Mach number approximation, the transport equation of the enthalpy h may be written as:

$$\partial_{t^o}(\rho^o h^o) + \nabla^o \cdot \rho^o \mathbf{u}^o h^o = \nabla^o \cdot k^o \nabla^o T^o, \quad (24)$$

where $(\dots)^o$ denotes a dimensional quantity. The diffusive term can be rewritten in terms of the enthalpy by considering the following thermodynamic relations:

$$dh^o = \left(\frac{\partial h^o}{\partial T^o} \right)_{p^o} dT^o + \left(\frac{\partial h^o}{\partial p^o} \right)_{T^o} dp^o \quad (25)$$

$$\rho^{o2} \left(\frac{\partial h^o}{\partial p^o} \right)_{T^o} = \rho^o + T^o \left(\frac{\partial \rho^o}{\partial T^o} \right)_{p^o}. \quad (26)$$

The second of these relations is known as one of the two general thermodynamic equations of state that are valid for a system in equilibrium, see Zappoli et al. [2015]. Noting that

the thermal expansion coefficient at constant pressure is defined as $\beta^o = (\partial\rho^o/\partial T^o)/\rho^o$, we may write;

$$dh^o = c_p^o dT^o + (1 + \beta^o T^o) dp^o / \rho^o. \quad (27)$$

The last result can be used to write:

$$\nabla^o h^o = c_p^o \nabla^o T^o + (1 + \beta^o T^o) \nabla^o p^o / \rho^o. \quad (28)$$

If the scaling, $p^o \propto \rho_{pc} c^2$ (where c is the speed of sound), $\rho \propto \rho_{pc}$, as well as $c_p^o dT^o = w_b^2 c_p dT$ are used, in addition to $p = p_{th}(t) + p_{hy}(\mathbf{x}, t)$ (where p_{th} is the thermodynamic pressure and p_{hy} the hydrodynamic pressure), the following is obtained:

$$\nabla h = c_p \nabla T + (1 + \beta^o T^o) \rho^{-1} Ma^{-2} \nabla p_{hy}, \quad (29)$$

where quantities without a $(\dots)^o$ denote non-dimensional quantities. Using the following scaling estimates:

$$\nabla h \propto \frac{\Delta h}{\lambda_{th}}, \quad \nabla T \propto \frac{\Delta T}{\lambda_{th}} \quad \text{and} \quad \nabla p_{hy} \propto \frac{\rho w_b^2}{\mathcal{L}}, \quad (30)$$

where \mathcal{L} is the integral length scale, $\lambda_{th} \equiv \lambda/\sqrt{Pr}$, the thermal equivalent of the Taylor micro scale λ , which yields:

$$\Delta h \propto c_p \Delta T + w_b^2 \left(\frac{1 + \beta^o T^o}{\sqrt{Pr}} \right) \left(\frac{\lambda}{\mathcal{L}} \right) \quad (31)$$

Since in a turbulent flow it holds that $\lambda/\mathcal{L} \ll 1$, the second term can be neglected, which implies that $dh \approx c_p dT$. This transforms Fourier's law into:

$$q = -k \nabla T = -\frac{k}{c_p} \nabla h. \quad (32)$$

A.1.5 Derivation of the Nusselt number relation

We first define the Stanton number as $St \equiv q_w^o / (\rho_{pc}^o w_b^o (h_h^o - h_i^o))$. Decomposing all variables (except the density) of equation (4.1) and subsequently averaging the result yields:

$$-r^{-1} d_r (r \widetilde{\bar{\rho} u'' h''}) + (r Re Pr_h)^{-1} d_r (\widetilde{\bar{\rho} a d_r \tilde{h}}) + (r Re Pr_h)^{-1} d_r (\widetilde{\bar{\rho} a'' d_r h''}) = 0 \quad (33)$$

Multiplying by r and integrating once, we obtain:

$$-\widetilde{\bar{\rho} u'' h''} + (Re Pr_h)^{-1} \widetilde{\bar{\rho} a d_r \tilde{h}} + (Re Pr_h)^{-1} \widetilde{\bar{\rho} a'' d_r h''} + Cr^{-1} = 0 \quad (34)$$

Evaluating this equation at the inner wall $r = 0.5$ and noting that the fluctuating quantities are zero at the wall, in addition that $(Re Pr_h)^{-1} \widetilde{\bar{\rho} a d_r \tilde{h}} = (Re_b Pr_h)^{-1} q_w = St$, gives

$C = -St/2$. Integrating equation (34) from $r = R_{in}$ to $r = R_a$, while noting that the Stanton number is constant, yields:

$$StRe_bPr_h = \Gamma \left\{ \int_{R_{in}}^{R_a} \bar{\rho}\tilde{a} \frac{d\tilde{h}}{dr} dr + \int_{R_{in}}^{R_a} \bar{\rho}a'' \frac{d\tilde{h}''}{dr} dr - Re_bPr_h \int_{R_{in}}^{R_a} \bar{\rho}u''\tilde{h}'' dr \right\}, \quad (35)$$

where $\Gamma \equiv (1/R_{in})/\ln(R_{in}/R_a)$. Multiplying by $(T_h - T_l)/(T_h - T_b)$ yields equation (4.6).

A.2 Tensors and dyadics

Proofs of the identities that were used in the previous section are given in this section. It is assumed that the elements of all tensors are twice continuously differentiable. By Young's theorem, this implies that:

$$\frac{\partial^2 f}{\partial x_i \partial x_j} = \frac{\partial^2 f}{\partial x_j \partial x_i}. \quad (36)$$

For a mathematical proof, see Rudin [1976].

A.2.1 Curl of the divergence of a second order tensor

Let \mathbf{T} be a second order tensor and let the tensor elements T_{ij} be twice continuously differentiable. Then, $\nabla \times (\nabla \cdot \mathbf{T}) = \nabla \cdot (\nabla \times \mathbf{T}^T)$.

The divergence of the second order tensor \mathbf{T} can be written in index notation as:

$$(\nabla \mathbf{T})_j = \frac{\partial T_{jq}}{\partial x_q}. \quad (37)$$

The k^{th} element of the curl of $\nabla \cdot \mathbf{T}$ is then:

$$\begin{aligned} (\nabla \times (\nabla \cdot \mathbf{T}))_k &= \varepsilon_{ijk} \frac{\partial^2 T_{jq}}{\partial x_i \partial x_q} \\ &= \frac{\partial}{\partial x_q} \left(\varepsilon_{ijk} \frac{\partial T_{jq}}{\partial x_i} \right) \\ &= \frac{\partial}{\partial x_j} \left(\varepsilon_{iqk} \frac{\partial T_{qj}}{\partial x_i} \right) \\ &= \frac{\partial}{\partial x_j} \left(\varepsilon_{kjq} \frac{\partial T_{qj}}{\partial x_i} \right) \\ &= (\nabla \cdot (\nabla \times \mathbf{T}^T))_k \end{aligned} \quad (38)$$

A.2.2 Curl of a gradient- vector- dyadic tensor

Let \mathbf{v} be a tensor of order one (a vector) and let the elements v_j be twice continuously differentiable. Then, $\nabla \times \nabla \mathbf{v} = \mathbf{0}$.

The $(ij)^{\text{th}}$ element of $\nabla \times \nabla \mathbf{v}$ can be written as:

$$\begin{aligned}
\nabla \times \nabla \mathbf{v} &= \varepsilon_{ipq} \frac{\partial^2 v_j}{\partial x_p \partial x_q} \\
&= \varepsilon_{ipq} \frac{\partial^2 v_j}{\partial x_q \partial x_p} \\
&= -\varepsilon_{iqp} \frac{\partial^2 v_j}{\partial x_q \partial x_p} \\
&= -\varepsilon_{ipq} \frac{\partial^2 v_j}{\partial x_p \partial x_q}
\end{aligned} \tag{39}$$

and therefore, $\nabla \times \nabla \mathbf{v} = \mathbf{0}$.

A.2.3 Curl of the transpose of a gradient- vector- dyadic tensor

Let \mathbf{v} be a tensor of order one (vector) and let the elements v_j be twice continuously differentiable. Then, $\nabla \times (\nabla \mathbf{v})^T = \nabla(\nabla \times \mathbf{v})$.

$$\begin{aligned}
(\nabla \times (\nabla \mathbf{v})^T)_{ij} &= \varepsilon_{ipq} \frac{\partial^2 u_q}{\partial x_p \partial x_j} \\
&= \frac{\partial}{\partial x_p} \left(\varepsilon_{ipq} \frac{\partial u_q}{\partial x_j} \right) \\
&= \frac{\partial}{\partial x_j} \left(\varepsilon_{ipq} \frac{\partial u_q}{\partial x_p} \right) \\
&= \frac{\partial}{\partial x_j} \left(-\varepsilon_{iqp} \frac{\partial u_q}{\partial x_p} \right) \\
&= \frac{\partial}{\partial x_j} \left(\varepsilon_{pq i} \frac{\partial u_q}{\partial x_p} \right) \\
&= (\nabla(\nabla \times \mathbf{v}))_{ij}
\end{aligned} \tag{40}$$

Thus, $\nabla \times \nabla \mathbf{v} = \nabla(\nabla \times \mathbf{v})$.

A.2.4 Curl of a tensor multiplied by a scalar

Let \mathbf{T} be a second order tensor and let f be a scalar. Then, $\nabla \times f\mathbf{T} = \nabla f \times \mathbf{T} + f\nabla \times \mathbf{T}$.

$$\begin{aligned}
(\nabla \times f\mathbf{T})_{ij} &= \varepsilon_{ipq} \frac{fT_{jq}}{\partial x_p} \\
&= \frac{\partial f}{\partial x_p} \varepsilon_{ipq} T_{jq} + f \varepsilon_{ipq} \frac{\partial T_{jq}}{\partial x_p} \\
&= (\nabla f \times \mathbf{T})_{ij} + (f \nabla \times \mathbf{T})_{ij}
\end{aligned} \tag{41}$$

Thus, $\nabla \times f\mathbf{T} = \nabla f \times \mathbf{T} + f \nabla \times \mathbf{T}$.

A.2.5 Divergence of the curl of the identity tensor multiplied by a scalar

Let \mathbf{I} be the second order identity tensor and let f be a scalar which is continuously twice differentiable. Then, $\nabla \cdot (\nabla \times f\mathbf{I}) = \mathbf{0}$.

The $(ij)^{\text{th}}$ element of $\nabla \times f\mathbf{I}$ can be written as:

$$(\nabla \times f\mathbf{I})_{ij} = \varepsilon_{ipq} \frac{fI_{jq}}{\partial x_p} \tag{42}$$

The i^{th} of $\nabla \cdot (\nabla \times f\mathbf{I})$ is then:

$$(\nabla \cdot (\nabla \times f\mathbf{I}))_i = \varepsilon_{ipq} \frac{\partial^2 f I_{jq}}{\partial x_j \partial x_p} \tag{43}$$

Because the off diagonal elements of T_{jq} are zero, we can change the index q in ε_{ipq} to j :

$$\begin{aligned}
(\nabla \cdot (\nabla \times f\mathbf{I}))_i &= \varepsilon_{ipj} \frac{\partial^2 f I_{jq}}{\partial x_j \partial x_p} \\
&= \varepsilon_{ipj} \frac{\partial^2 f I_{jq}}{\partial x_p \partial x_j} \\
&= -\varepsilon_{ijp} \frac{\partial^2 f I_{jq}}{\partial x_p \partial x_j} \\
&= -\varepsilon_{ipj} \frac{\partial^2 f I_{jq}}{\partial x_j \partial x_p}
\end{aligned} \tag{44}$$

Therefore, $\nabla \cdot (\nabla \times f\mathbf{I}) = \mathbf{0}$.

A.2.6 Dot product of a vector \mathbf{v} and the divergence of a second order tensor \mathbf{T}

Let \mathbf{v} be a vector and let \mathbf{T} be a symmetric second order tensor. Then, the following identity is true: $\mathbf{v} \cdot \nabla \cdot \mathbf{T} = \nabla \cdot (\mathbf{T}^\top \cdot \mathbf{v}) - \mathbf{T} : \nabla \mathbf{v}$.

$$\begin{aligned}
 \nabla \cdot (\mathbf{T} \cdot \mathbf{v}) &= \frac{\partial}{\partial x_i} (T_{ij} v_j) \\
 &= v_j \frac{\partial T_{ij}}{\partial x_i} + T_{ij} \frac{\partial v_j}{\partial x_i} \\
 &= v_i \frac{\partial T_{ji}}{\partial x_j} + T_{ji} \frac{\partial v_i}{\partial x_j} \\
 &= \mathbf{v} \cdot (\nabla \cdot \mathbf{T}^\top) + \mathbf{T}^\top : \nabla \mathbf{v}
 \end{aligned} \tag{45}$$

Therefore, $\mathbf{v} \cdot \nabla \cdot \mathbf{T} = \nabla \cdot (\mathbf{T}^\top \cdot \mathbf{v}) - \mathbf{T} : \nabla \mathbf{v}$.

A.2.7 Outer product between a vector and a second order tensor in cylindrical coordinates

A dyadic tensor \mathbf{A} is a second order tensor that is the dyadic product of two vectors. In cylindrical coordinates, \mathbf{A} may be written as:

$$\mathbf{A} = \mathbf{a}'_r \mathbf{u}_r + \mathbf{a}'_\theta \mathbf{u}_\theta + \mathbf{a}'_z \mathbf{u}_z, \tag{46}$$

where \mathbf{u}_r , \mathbf{u}_θ and \mathbf{u}_z are the unit vectors of the cylindrical coordinate system and where $\mathbf{a}'_r \mathbf{u}_r \equiv \mathbf{a}'_r \otimes \mathbf{u}_r$. The vectors \mathbf{a}'_r , \mathbf{a}'_θ , \mathbf{a}'_z are written as:

$$\begin{aligned}
 \mathbf{a}'_r &= a_{rr} \mathbf{u}_r + a_{\theta r} \mathbf{u}_\theta + a_{zr} \mathbf{u}_z \\
 \mathbf{a}'_\theta &= a_{r\theta} \mathbf{u}_r + a_{\theta\theta} \mathbf{u}_\theta + a_{z\theta} \mathbf{u}_z \\
 \mathbf{a}'_z &= a_{rz} \mathbf{u}_r + a_{\theta z} \mathbf{u}_\theta + a_{zz} \mathbf{u}_z
 \end{aligned} \tag{47}$$

A dyadic tensor $\mathbf{A} \equiv \mathbf{v} \times \mathbf{T}$ then has the following elements;

$$\begin{aligned}
 (\mathbf{v} \times \mathbf{a}'_r) \mathbf{u}'_r &= \underbrace{(a_{zr} v_\theta - a_{\theta r} v_z)}_{A_{rr}} \mathbf{u}'_r \mathbf{u}'_r \\
 &+ \underbrace{(a_{rr} v_z - a_{zr} v_r)}_{A_{\theta r}} \mathbf{u}'_\theta \mathbf{u}'_r \\
 &+ \underbrace{(a_{\theta r} v_r - a_{rr} v_\theta)}_{A_{zr}} \mathbf{u}'_z \mathbf{u}'_r
 \end{aligned}$$

$$\begin{aligned}
(\mathbf{v} \times \mathbf{a}'_{\theta}) \mathbf{u}'_{\theta} &= \underbrace{(a_{z\theta}v_{\theta} - a_{\theta\theta}v_z)}_{A_{r\theta}} \mathbf{u}'_r \mathbf{u}'_{\theta} \\
&+ \underbrace{(a_{r\theta}v_z - a_{z\theta}v_r)}_{A_{\theta\theta}} \mathbf{u}'_{\theta} \mathbf{u}'_{\theta} \\
&+ \underbrace{(a_{\theta\theta}v_r - a_{r\theta}v_{\theta})}_{A_{z\theta}} \mathbf{u}'_z \mathbf{u}'_{\theta}
\end{aligned} \tag{48}$$

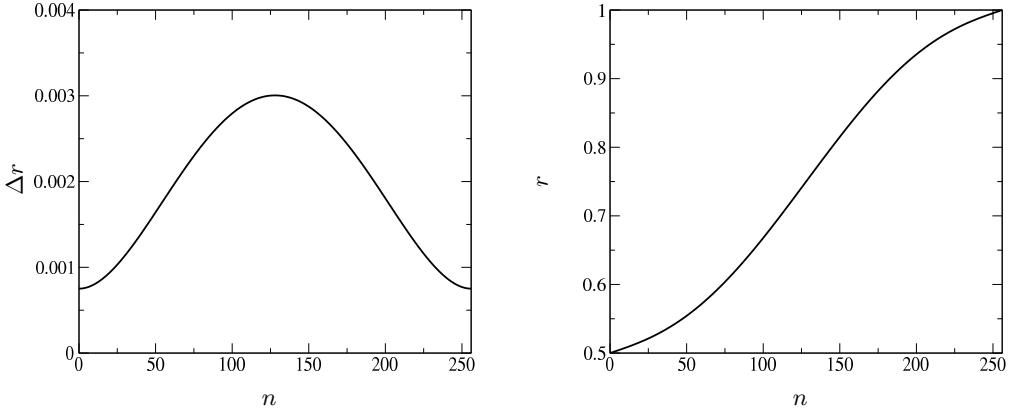
$$\begin{aligned}
(\mathbf{v} \times \mathbf{a}'_z) \mathbf{u}'_z &= \underbrace{(a_{zz}v_{\theta} - a_{z\theta}v_{\theta})}_{A_{rz}} \mathbf{u}'_r \mathbf{u}'_z \\
&+ \underbrace{(a_{rz}v_z - a_{zz}v_r)}_{A_{\theta z}} \mathbf{u}'_{\theta} \mathbf{u}'_z \\
&+ \underbrace{(a_{\theta z}v_r - a_{rz}v_{\theta})}_{A_{zz}} \mathbf{u}'_z \mathbf{u}'_z
\end{aligned}$$

The divergence of \mathbf{A} is easily determined as:

$$\nabla \cdot \mathbf{A} = \left(\nabla \cdot \mathbf{a}'_r - \frac{a_{\theta\theta}}{r} \right) \mathbf{u}_r + \left(\nabla \cdot \mathbf{a}'_{\theta} + \frac{a_{\theta r}}{r} \right) \mathbf{u}'_{\theta} + (\nabla \cdot \mathbf{a}'_z) \mathbf{u}'_z, \tag{49}$$

where,

$$\begin{aligned}
\nabla \cdot \mathbf{a}'_r &= \frac{1}{r} \left(\frac{\partial r A_{rr}}{\partial r} \right) + \frac{1}{r} \frac{\partial A_{\theta r}}{\partial \theta} + \frac{\partial A_{zr}}{\partial z}, \\
\nabla \cdot \mathbf{a}'_{\theta} &= \frac{1}{r} \left(\frac{\partial r A_{r\theta}}{\partial r} \right) + \frac{1}{r} \frac{\partial A_{\theta\theta}}{\partial \theta} + \frac{\partial A_{z\theta}}{\partial z}, \\
\nabla \cdot \mathbf{a}'_z &= \frac{1}{r} \left(\frac{\partial r A_{rz}}{\partial r} \right) + \frac{1}{r} \frac{\partial A_{\theta z}}{\partial \theta} + \frac{\partial A_{zz}}{\partial z}.
\end{aligned} \tag{50}$$



(a) Wall normal mesh width versus gridpoint number ($N = 256$).

(b) Radial distance versus gridpoint number ($N = 256$).

Figure A.3.1: Wall normal mesh width and radial distance versus grid point number according to equation (51) for $N = 256$.

A.3 Additional case details

A.3.1 Mesh generation

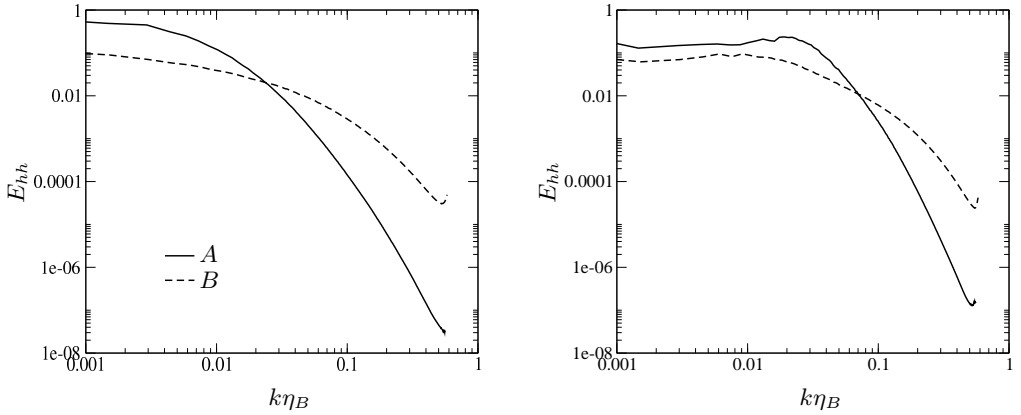
The wall normal mesh size is calculated according to:

$$\Delta r(n) = \frac{1}{0.65} \left(\frac{1/8}{N} + 6 \frac{n^4}{N^5} - 12 \frac{n^3}{N^4} + 6 \frac{n^2}{N^3} \right), \quad (51)$$

where Δr is the wall normal size, n the grid number and N the total number of grid points in the wall normal direction. This leads to a modest stretching of the cells, as can be seen in figure 1(a) and 1(b).

A.3.2 Enthalpy power spectra

Power spectra of the enthalpy fluctuations are shown in figure 2(a) and 2(b) for the stream-wise and circumferential directions respectively at two different points (A and B) in the forced convection $s\text{CO}_2$ case. Point A refers to the wall normal location where the enthalpy fluctuations are the largest (near the hot wall), while point B corresponds to the wall normal location where the mean molecular Prandtl number has its maximum. In point A at least 6 decades are resolved, while in point B, at least 3 decades are resolved. There is a small build-up of energy at the highest wave numbers, which is assumed to be too small to affect the results in this paper. As the momentum scales are larger than



(a) Stream-wise power spectra of enthalpy fluctuations.

(b) Circumferential power spectra of enthalpy fluctuations.

Figure A.3.2: Wall normal mesh width and radial distance versus gridpoint number (upper row). Stream-wise and Circumferential power spectra. Point A corresponds to the location where h_{rms} is largest, point B refers to the location where \overline{Pr} is largest.

the thermal scales for Prandtl numbers larger than unity, the mesh can be considered to be sufficient to resolve all momentum scales.

Bibliography

J. Bladel. *Electromagnetic Fields*. Wiley-IEEE Press, 2007.

M.E. Gurtin, E. Fried, and L. Anand. *The Mechanics and Thermodynamics of Continua*. Cambridge University Press, 2010.

W. Rudin. *Principles of Mathematical Analysis*. McGraw-Hill, New York, 3rd edition, 1976.

B. Zappoli, D. Beysens, and Y. Garrabos. *Heat transfers and related effects in supercritical fluids*. Springer, 2015.